INFORMATION TO USERS

This manuscript has been reproduced from the microfilm master. UMI films the text directly from the original or copy submitted. Thus, some thesis and dissertation copies are in typewriter face, while others may be from any type of computer printer.

The quality of this reproduction is dependent upon the quality of the copy submitted. Broken or indistinct print, colored or poor quality illustrations and photographs, print bleedthrough, substandard margins, and improper alignment can adversely affect reproduction.

In the unlikely event that the author did not send UMI a complete manuscript and there are missing pages, these will be noted. Also, if unauthorized copyright material had to be removed, a note will indicate the deletion.

Oversize materials (e.g., maps, drawings, charts) are reproduced by sectioning the original, beginning at the upper left-hand corner and continuing from left to right in equal sections with small overlaps.

Photographs included in the original manuscript have been reproduced xerographically in this copy. Higher quality 6" x 9" black and white photographic prints are available for any photographs or illustrations appearing in this copy for an additional charge. Contact UMI directly to order.

UNIVERSITY OF ALBERTA

Simulation of Coupled Aqueous and Non-aqueous Phase
Flow and Transport In a Fracture

BY

Melody Dawn Larsen Heise

A thesis submitted to the Faculty of Graduate Studies and Research in partial fulfillment of the requirements for the degree of Master of Science.

DEPARTMENT OF EARTH AND ATMOSPHERIC SCIENCES

Edmonton, Alberta
Fall 1999

0-612-47038-5

Canada

UNIVERSITY OF ALBERTA

LIBRARY RELEASE FORM

NAME OF AUTHOR: Melody Dawn Larsen Heise

TITLE OF THESIS: Simulation of Coupled Aqueous and Non-aqueous Phase Flow and Transport In a Fracture

DEGREE: Master of Science

YEAR THIS DEGREE GRANTED: 1999

Permission is hereby granted to the University of Alberta Library to reproduce single copies of this thesis and to lend or sell such copies for private, scholarly or scientific research purposes only.

The author reserves all other publication and other rights in association with the copyright in the thesis, and except as hereinbefore provided neither the thesis nor any substantial portion thereof may be printed or otherwise reproduced in any material form whatever without the author's prior written permission.
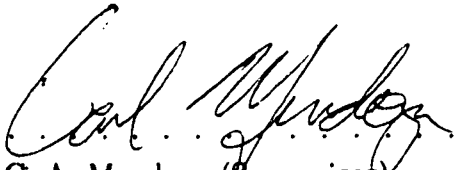
(Signed) . . . .
Melody Dawn Larsen Heise
6 Laurier Cresent
St. Albert, Alberta
Canada, T8N 1M7
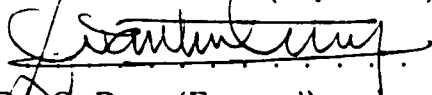
Date: . Aug 31 /99 .
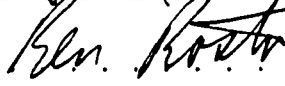
UNIVERSITY OF ALBERTA
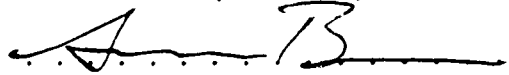
FACULTY OF GRADUATE STUDIES AND RESEARCH

The undersigned certify that they have read, and recommend to the Faculty of Graduate Studies and Research for acceptance, a thesis entitled **Simulation of Coupled Aqueous and Non-aqueous Phase Flow and Transport In a Fracture** submitted by Melody Dawn Larsen Heise in partial fulfillment of the requirements for the degree of Master of Science.

Dr. C. A. Mendoza (Supervisor)

Dr. Q. Doan (External)

Dr. B. Rostron (Examiner)

Dr. A. Bush (Examiner)

Dr. A. Bush (Chair)

Date: Aug. 30, 1999

For my family,
who have been constant, ongoing supporters,
and
for Geoff,
the love of my life

Abstract

Many studies have examined flow of water and a non-aqueous phase liquid (NAPL) in a discrete fracture, but few have attempted to examine the effect that dissolution and aqueous-phase transport have on NAPL flow. Various researchers have shown that mass can be removed from the fracture via diffusion into the porous fracture walls. They have also shown that fracture walls can act as a significant storage medium until water with a lower concentration flushes the dissolved material out.

A finite-difference computer program was written to simulate NAPL flow with dissolution and aqueous-phase transport in a vertical, discrete, rough-walled fracture embedded in a porous, but non-permeable matrix. The rate of NAPL flow through a fracture, the distribution of NAPL in the fracture, the dissolved mass concentration distribution in the fracture and the matrix, and the amount of mass that diffuses into the porous matrix surrounding the fracture were examined as a means of defining the total system behaviour, including the effects that coupling flow and transport together have. The sensitivity of these model outputs to differing input parameters was also examined.

The coupling, or the effect that both dissolution and aqueous phase transport have on flow, was found to be weak at low to moderate NAPL solubilities. Matrix diffusion was very sensitive to the diffusion coefficient, NAPL solubility, and matrix porosity. The sensitivity of NAPL flow to other factors such as fracture aperture field statistics, NAPL properties, and boundary conditions was also examined and found to have varying degrees and types of sensitivity. In particular, mean aperture and variance have a great effect on NAPL travel time and distribution.

Acknowledgements

A Master's degree is so much more than you presently have in your hands. It is not only a time of academic learning, but a time of personal growth and development. The last three years have been a time of incredible transition for me. I have moved away from home, gotten married, bought a house, secured a full-time job, and, of course, graduated from university (although, not necessarily in that order!!). There are many people that have helped me through this time.

Firstly, I wish to say "Thank you" to Dr. Carl Mendoza for his assistance in the preparation of this thesis. My Master's degree was a long, hard struggle up the learning curve. Thanks for the hand up. Thanks also to my supervisory committee, Dr. Ben Rostron, Dr. Andrew Bush, and Dr. Quang Doan. Your time and energy spent on my thesis is greatly appreciated. I also wish to thank the department of Earth and Atmospheric Sciences for their financial support through teaching assistantships, as well as the Natural Sciences and Research Council for granting me a scholarship. Also, Judith Enarson was a great source of help and support from the first day I walked into the EAS office. We are truly fortunate to have her on our side.

I want to acknowledge some of the friends I have made here at the University: Sheri, Brent, Darlene, Tannis, Jennifer, Kristine, Heather, and Adam. I'm sure that I drove Brent crazy with my million-and-one questions about programming, but he always found the time to help me out. Thank you. I also want to congratulate Darlene on finishing her thesis. It was great to have someone to talk to during my time here. A special thanks to Tannis for being such a great friend. She was never too busy to help me out. The best of luck to those students that have still yet to

finish. My one word of advice: finish your thesis BEFORE you start working!! And keep the faith, even when things look dim. You will make it.

My family (both sides) have also been wonderful sources of support over the last three years (and the rest of my life, too!). Mom and Dad Heise were always interested in my progress, and celebrated with me during times of triumph. Mom and Dad Larsen have always supported my academics and were there to listen during my dark hours as well. I cannot put in to words how indebted I am to all of you. Thank you.

Last, but certainly not least, my husband, Geoff. You are my best and truest friend, my confidant, and my miracle. We have so many special times ahead. I will see your face in the faces of our children, and I take comfort in knowing that you will be a wonderful father. I know that with this will come many burdens. I promise to stand with you through all of life's trials, and to always believe in you and in us.

You have my respect, my gratitude, my love, and my friendship ... forever.

Contents

List of Tables

List of Figures

Notation

Domain Definition

b	fracture aperture width	$[L]$	m
$\overline{Y}$	ln-mean aperture value	$[-]$	ln (m)
$\bar{b}$	geometric-mean aperture value	$[L]$	m
σ_Y^2	ln-aperture variance	$[-]$	-
f_{sp}	fracture spacing	$[L]$	m
λ_{sp}	spatial aperture correlation	$[L]$	m
$\Delta x, \Delta z, \Delta y$	grid discretization in three coordinate directions	$[L]$	m
N_b	number of blocks	$[-]$	-
ϕ	porosity	$[-]$	-
R	retardation factor	$[-]$	-
ρ_b	porous medium bulk density	$[M]/[L^3]$	g/cm^3
K_d	partitioning coefficient	$[L^3]/[M]$	mL/g
f_{oc}	soil organic content	$[-]$	-
K_{oc}	organic carbon partitioning coefficient	$[L^3]/[M]$	mL/g

Notation

Flow

k	intrinsic permeability	$[L^2]$	m^2
k_r	relative permeability	$-$	-
ρ	density	$[M]/[L^3]$	kg/m^3
μ	dynamic viscosity	$[M]/[LT]$	Pa · s
σ	interfacial tension	$[M]/[T^2]$	N/m
θ	contact angle	$[-]$	-
λ	pore size distribution index	$[-]$	-
m	van Genuchten and Parker fitting parameter	$[-]$	-
α	fitting parameter for Leverett J scaling	$[-]$	-
P	pressure	$[M]/[LT^2]$	Pa
P_c	capillary pressure $(P_n - P_w)$	$[M]/[LT^2]$	Pa
P_c^*	fracture entry pressure	$[M]/[LT^2]$	Pa
P_d	displacement pressure	$[M]/[LT^2]$	Pa
P_c'	dimensionless capillary pressure	$[-]$	-
S	volumetric saturation	$[-]$	-
S_r	residual volumetric saturation	$[-]$	-
S_e	effective volumetric saturation	$[-]$	-
q	Darcy velocity (flux)	$[L]/[T]$	m/s
v	average linear groundwater velocity	$[L]/[T]$	m/s
h	equivalent head	$[L]$	m
H	height of column of DNAPL	$[L]$	m

Notation

Transport

MW	molecular weight	$[M]/[mol]$	g/mol
C	concentration	$[M]/[L^3]$	kg/m^3
s	NAPL solubility	$[M]/[L^3]$	kg/m^3
F	diffusive mass flux	$[M]/[L^2 T]$	kg/(m^{2}s)
$\mathbf{D}_{ij}$	hydrodynamic dispersion tensor	$[L^2]/[T]$	m^2/s
D	free diffusion coefficient	$[L^2]/[T]$	m^2/s
D^*	effective diffusion coefficient	$[L^2]/[T]$	m^2/s
α_L	longitudinal dispersivity	$[L]$	m
α_T	transverse dispersivity	$[L]$	m
δ_{ij}	Kronecker delta	$[-]$	-
τ	tortuosity	$[L/L]$	-
k_f	mass transfer coefficient	$[L^2]/[T]$	m^2/s
q'	mass source/sink term	$[M]/[L^3 T]$	kg/(m^{3}s)
Q_w	water mass source/sink coupling term	$[M]/[L^3 T]$	kg/(m^{3}s)
Q_n	NAPL mass source/sink coupling term	$[M]/[L^3 T]$	kg/(m^{3}s)
J	net mass flux per unit volume	$[M]/[LT]$	kg/(ms)
J'	total mass flux for fracture	$[ML^2]/[T]$	kg · m^2/s

Notation

Miscellaneous

E_n	Euclidean norm	[−]	-
l_1	normalized l_1 norm	[−]	-
g	gravitational acceleration constant	$[L]/[T^2]$	m/s^2
β	time weighting factor for transport	[−]	-
t	time	$[T]$	s
Δt	time step size	$[T]$	s

Superscripts

nr	Newton-Raphson
cp	coupled
con	concentration

Subscripts

w	wetting phase (water)
n	non-aqueous phase (oil)
a	air phase
i, j	two cartesian coordinate directions (i.e. x and z)
f	fracture
m	matrix
tol	tolerance

Chapter 1

Introduction and Objectives

The widespread use of non-aqueous phase liquids (NAPLs) such as trichloroethy-lene and other chlorinated solvents in recent history has led to a large number of intentional or inadvertent releases of NAPL into the subsurface. These chemicals can migrate into irrigation or drinking water supplies and be difficult and costly to remediate (Mackay and Cherry, 1989; Imhoff and Miller, 1996). Efforts to contain subsurface contamination are often hampered by the existence of subsurface materials containing fractures because fractures may act as high permeability conduits for flow and contaminant transport. Knowledge of the processes that control flow and transport through fractures is limited; furthermore, the parameters needed to describe flow and transport through fractures are not easily characterized. This study enhances our understanding of two-phase flow and transport processes in fractures by exploring the degree to which coupling of dissolved aqueous phase transport with immiscible phase flow should be a significant consideration. Also examined is how dissolution and matrix diffusion rates might affect the distribution of NAPL in a rough-walled fracture, and if the matrix serves as an important storage mechanism for contamination.

Traditional fracture flow and transport studies often assume that a fracture can be represented by two smooth parallel plates. However, as virtually all natural fractures are non-smooth and non-parallel, the validity of this representation must be evaluated. Many researchers have done so (Witherspoon *et al.*, 1980; Brown, 1987; Ge,

1997). Their major findings are, generally, that the cubic law is an acceptable representation of a rough-walled fracture on a local scale; however, this characterization can be sensitive to stress exerted on the fracture as well as microscale fracture roughness. The cubic law is, at best, a reasonable (if simplified) conceptual representation of a rough-walled fracture.

The computer program **FaTMatD** was written to simulate NAPL flow with dissolution and aqueous-phase transport in a vertical, discrete, rough-walled fracture embedded in a porous, but non-permeable matrix. A log-normally distributed, exponentially correlated aperture field was assumed, with permeability on the local scale estimated by the cubic law. Model inputs were either taken from the literature or assumed, as appropriate. The rate of NAPL flow through the fracture, the distribution of NAPL in the fracture, the dissolved mass concentration distribution in the fracture and the matrix, and the amount of mass that diffuses into the porous matrix surrounding the fracture were examined as a means of defining the total perceived system behaviour, including the effects that coupling flow and transport have. The sensitivity of these model outputs to differing input parameters was also examined.

Traditional studies (Mackay and Cherry, 1989; Mercer and Cohen, 1990) assume that dissolved phase NAPL cannot dissolve and/or diffuse into a porous matrix. Other studies, such as the study conducted by Mayer and Miller (1986), consider NAPL flow with dissolution and transport sequentially, where NAPL dissolution has no effect on the bulk movement of NAPL. Parker *et al.* (1994; 1997) quantified dissolution and matrix diffusion in the absence of bulk NAPL or aqueous-phase flow. The novel aspect of the study conducted here is the simulated coupling between the flow of NAPL and transport of the dissolved phase in a fracture and the surrounding porous matrix. It combines aspects of the above mentioned studies to provide a more conceptually correct solution for NAPL flow with dissolution in a single, rough-walled fracture.

Chapter 2

Background and Theoretical Development

Schwille (1988), Kueper and McWhorter (1991), Parker et al. (1994), Banack (1996), and others have offered conceptual models similar to that shown in Figure 2.1. Here, a dense non-aqueous phase liquid (DNAPL), such as creosote or a chlorinated solvent, has been released into the subsurface where it percolated down through the unsaturated zone. Upon reaching the watertable, the DNAPL continued to migrate downward because it is denser than water. The free-phase DNAPL's downward migration might be arrested by capillary barriers such as a low permeability aquitard or bedrock; however, if this barrier contains fractures, flow may continue downwards. This study addresses migration processes through such fractures.

The way that DNAPL moves through fractures depends on several factors. Some of the chemical constituents that make up the DNAPL may dissolve and subsequently be transported in the aqueous phase. The dissolved phase is also subject to diffusion into the porous medium that surrounds the fracture. Matrix diffusion acts to attenuate the migration of dissolved-phase constituents (Ross and Lu, 1999).

The fractures shown in Figure 2.1 interconnect with one another, thus forming a network. The network may act to expand the range of a spill or leak by facilitating movement of both the free-phase NAPL and its dissolved constituents. This in turn may increase the extent of subsurface contamination, even though the concentrations

3
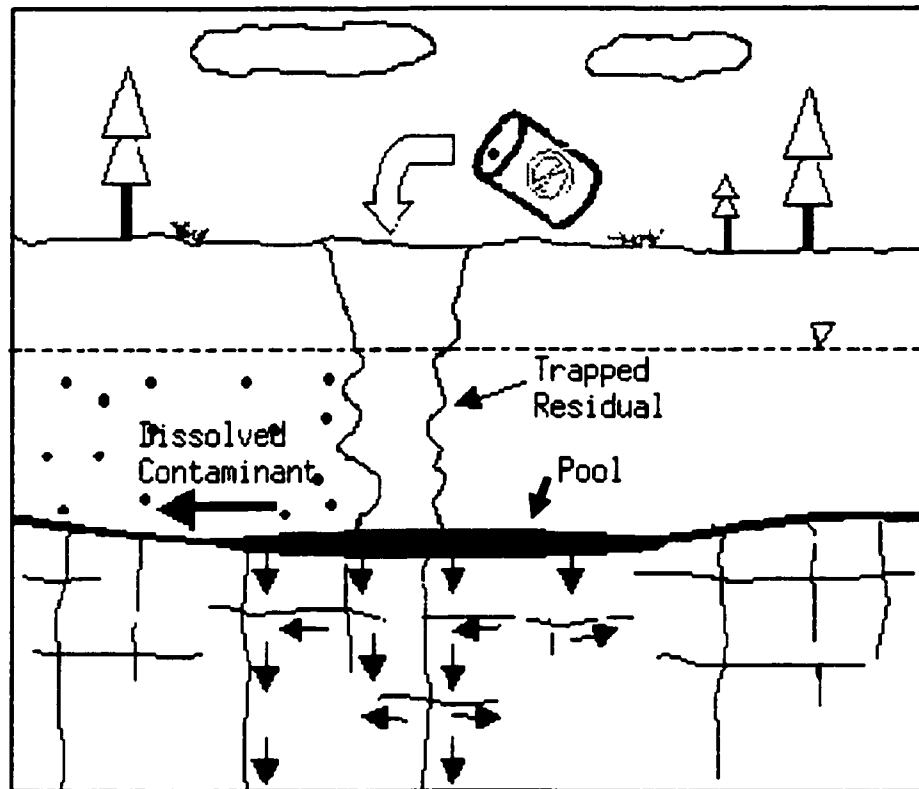
Figure 2.1: Conceptual model of a contamination scenario.

of dissolved phase contaminant may decrease substantially. These contaminants, even at reduced concentrations, can migrate into and contaminate aquifers used for drinking water or irrigation.

There are many ways that fractures, either singly or in fracture networks, may be conceptualized. The three major conceptual models are the equivalent porous media model, the dual porosity model, and the discrete fracture model. The equivalent porous media model attempts to approximate fracture and surrounding matrix properties, such as porosity and permeability, with average porous media properties. The dual porosity model acknowledges that the fracture and the matrix have very different properties with respect to porosity and permeability. As a result, the fracture is characterized by a high permeability and low porosity, while the medium surrounding the fracture is characterized by a low permeability and high porosity. The discrete fracture approach treats the fracture by itself, often without the consideration of interaction with the surrounding porous media. The following three sections describe these three conceptual models in greater detail (Anderson and Woessner, 1992).

2.0.1 Equivalent Porous Media Approach

The equivalent porous media approach replaces the fracture/matrix porosity and permeability with a continuous porous medium which attempts to approximate the fractured system with effective hydraulic properties. Tsang and Tsang (1989) used this approach to simulate water flow and tracer transport in a single fracture. This surrogate system tries to achieve the same overall flow pattern as the original fracture system, contingent upon the assumption that the fractured material can be treated as a continuum and that a representative elementary volume (REV) can be defined and assigned effective hydraulic parameters. An REV is defined as the smallest volume that can be assigned constant, unique properties such as porosity and permeability (Baveye and Sposito, 1984).

The equivalent porous media approach is commonly used to represent fracture networks at a regional scale (Moreno et al., 1988), as the difficulty in determining the

appropriate REV size for smaller scale problems precludes it from being an effective conceptual model at the local scale. Additionally, this conceptual model is used to emulate very densely fractured systems. As this thesis study involves neither regional nor densely fractured systems, this approach has not been taken.

2.0.2 Dual Porosity Approach

The concept of dual porosity representation is directly applicable when explicitly considering fractures in a porous matrix. The porous matrix that surrounds a discrete fracture may have a very low permeability (i.e., low ability to transmit fluid), but very good storage characteristics due to high porosity; porosities of up to 70% are not uncommon (Parker *et al.*, 1994) for commonly fractured materials. Conversely, fractures typically have a very high capacity to transmit fluid, or a high permeability, but make up only a very small volume of void space (porosity) of the medium. So, it is often not acceptable to define a single representative elementary volume that can be characterized with a single permeability and porosity for fractured media, as these permeabilities and porosities are functions of space and time. Nor is it feasible to completely separate the fractures and the matrix from one another. So, it must suffice to define a small block of porous medium as having two conductivities and two porosities, collectively known as dual porosity.

The dual porosity model is usually applied to fracture networks in low permeability porous media (Rossen and Shen, 1989; Peng *et al.*, 1990; Fung, 1991). This model has also been used to represent matrix diffusion in areas where the fractures in the network exist below the modelling scale (Sudicky and McLaren, 1992). The study here involves examination of only a single fracture embedded within a porous matrix; therefore, the dual porosity conceptual model was not utilized.

2.0.3 Discrete Fracture Approach

The discrete fracture conceptual model treats each fracture in a porous matrix as a discrete entity, where the fracture may or may not be considered as part of a bigger

network of fractures. This approach often assumes that free-phase movement (of water, NAPL, or air) occurs only in the fracture, and not in the surrounding porous matrix. As such, the discrete fracture approach is typically applied to fractures embedded in matrices with low permeability; however, it is possible to include free-phase movement in the matrix. This makes this approach very widely adaptable, yet costly in terms of computational time and efficiency.

The classical discrete fracture approach considers a fracture as being characterized by a set of parallel plates with uniform aperture along its length. This leads to the development of the "cubic law", which states that the volumetric flow rate per unit width of fracture is directly proportional to the cube of the aperture if flow is laminar (Wang, 1991). It can also be determined from the cubic law that the effective permeability of a fracture or fracture segment is given by (Pruess and Tsang, 1990):

$$k = \frac{b^2}{12} \tag{2.1}$$

where b is the aperture width. The cubic law has been shown to be locally valid for small fracture lengths (Witherspoon et al., 1980; Brown, 1987; Ge, 1997). In order to simulate a rough-walled, or variable aperture, fracture, many workers have assumed that the apertures within a fracture conform to log-normal distributions with an exponential correlation structure (Kueper and McWhorter, 1991; Mendoza and Sudicky, 1992). These fracture aperture distributions are biased towards having a large number of apertures considerably smaller than the mean aperture and a relatively small proportion of large apertures (Pruess and Tsang, 1990). At the microscale, each of these aperture segments are assumed to conform to the parallel plate ideology.

Other discrete fracture models include conceptualizing the matrix surrounding the fracture as cones of equal size in a closely packed configuration (Wang, 1991) or considering the fracture as having a composite topography (Brown, 1995). Composite topography views the fracture as having one flat side and the other rough-walled, with the aperture width forming the distance in between them. Fractal geometry is another method of fracture characterization used (Fetter, 1993), sometimes in combination

8

with other methods. This is a field of mathematics postulating that irregular objects such as fracture apertures tend to have patterns which repeat themselves at different scales.

As implied above, the discrete fracture approach is suitable for describing fractures on the small scale, especially when the primary interest is describing what occurs in the fracture itself. Complications of this approach include the efficacy of applying the solution to an actual fracture and its flow system in the field. In almost all cases, it is extremely difficult or impossible to determine reliable estimates of the small scale fracture aperture statistics required from field studies; in addition, the necessary computational requirements for this method can be very large.

2.1 Aqueous and Non-aqueous Phase Flow

In many studies (e.g., Parker *et al.* ,1994; Esposito and Thomson, 1999), the flow of water and NAPL is considered to occur separately and distinctly from each other in time and space. Parker *et al.* (1994) and Banack (1996) assume the fracture is occupied with free-phase NAPL at residual saturation, with water subsequently flushing the fracture. Because the NAPL is at residual saturation, it is assumed to be immobile in the fracture and therefore does not flow into or out of the fracture as a free-phase. The processes of water imbibition and drainage within fractures, with the corresponding cocurrent influx and outflux of free-phase NAPL, are considered in this study.

2.1.1 Wettability, Capillary Pressure, Entry Pressure, and Saturation

The conditions under which NAPL enters into or exits from a fracture arise from a number of fluid and fracture characteristics. Consider again the conceptual model given in Figure 2.1. Upon NAPL initially reaching the fractured material interface, some will pool above the fracture entry points. When the NAPL has accumulated

sufficient potential energy, it will enter the fracture. The dynamics that cause NAPL to flow in a rough-walled fracture are very complex; the theory behind NAPL flow will be discussed more thoroughly in this section. Note that the physics of flow through a discrete, rough-walled fracture has many similarities to flow in porous media. As such, both fields of study can be drawn upon.

Wettability

As a precursor to the discussion of NAPL and water flow, it is necessary to define the average spatial distribution that NAPL and water will have in the subsurface. This introduces the concept of wettability. In a two fluid system, one fluid can be characterized as the primary wetting fluid, and the other as the primary non-wetting fluid (Mercer and Cohen, 1990). The wetting fluid tends to coat the surface of grains and occupy the small pore spaces in a porous medium, whereas the non-wetting fluid will tend to be restricted to the large pore spaces or openings (cf., Figure 2.2). The degree of wettability depends on the interfacial tension, or free surface energy, between water, NAPL, and porous medium. The interfacial tension is the difference between the cohesive and adhesive forces in the fluids, which in turn depends on the thermal energy of the molecules (Bear, 1972). The constitutive relationships between the interfacial tensions for NAPL/solid grains (σ_{ns}), water/solid grains (σ_{ws}), and NAPL/water (σ_{nw}) are given by the Young-Laplace equation:

$$(\sigma_{nw}) \cos \theta = \sigma_{ns} - \sigma_{ws} \tag{2.2}$$

where θ is the contact angle between the fluids. The special case where water is considered to be perfectly wetting, and hence NAPL perfectly non-wetting, occurs when the difference in interfacial tension between the NAPL/solid grains and water/solid grains exactly equals the interfacial tension of the NAPL/water interface. This means that the contact angle, or the angle that is formed between the wetting and non-wetting fluids, is $0°$. In many cases, the simplifying assumption is made that water is perfectly wetting (Parker, 1989; Pruess and Tsang, 1990; Mendoza, 1992;
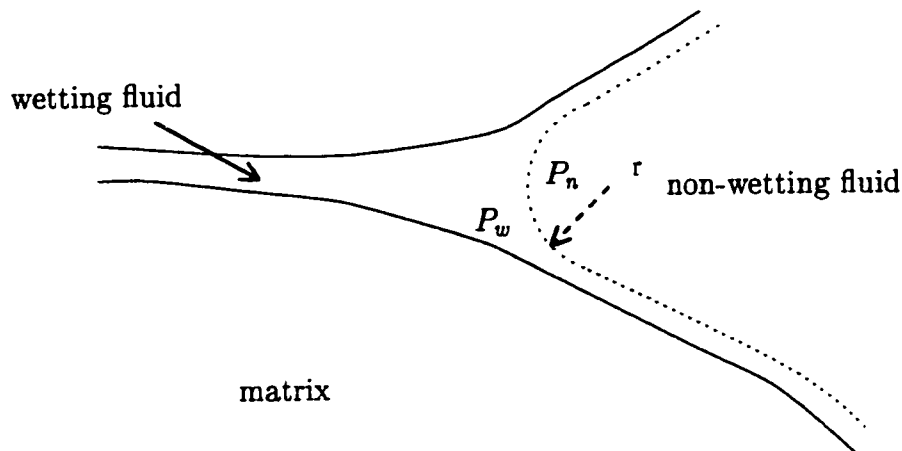
Figure 2.2: Capillary interface in porous media for the case where the wetting fluid perfectly wets the matrix (modified from Abdul, 1988).

Banack, 1996); however, the theory may be easily generalized for small angles.

Saturation

The fraction of the total void space in a porous medium that a fluid phase occupies is called the saturation of that phase (Mercer and Cohen, 1990). As such, the sum of the saturations of all fluid phases must equal unity. For a two-phase system (i.e., water-NAPL), this translates to:

$$S_w + S_n = 1 \qquad (2.3)$$

where S_w and S_n are the wetting and non-wetting phase saturations, respectively. This equation forms a fundamental constraint that must be satisfied when solving problems involving multiphase flow.

Capillary Pressure and Entry Pressure

When two fluids, such as water and non-aqueous phase liquid, coexist in the subsurface, there exists a pressure difference across the fluid-fluid interface (Parker, 1989). This pressure difference is termed the capillary pressure (P_c) and is defined as the difference between the non-wetting phase pressure (P_n) and the wetting phase pressure

(P_w):

$$P_c = P_n - P_w \qquad (2.4)$$

At equilibrium, the capillary pressure at the base of the NAPL pool is given by:

$$P_c = (\rho_n - \rho_w)gH \qquad (2.5)$$

where ρ_n is non-wetting (NAPL) phase density, ρ_w is wetting (water) phase density, g is gravitational acceleration, H is the height of the NAPL pool, and P_w and P_n are the pressures exerted by the wetting and non-wetting phases, respectively. This assumes that the top of the pool exists at zero capillary pressure and that hydrostatic conditions prevail.

NAPL will enter a water-filled fracture only if the capillary pressure at the leading edge is greater than the fracture entry (or displacement) pressure (Kueper and McWhorter, 1996). This means that the NAPL pressure must exceed the pressure needed to penetrate the fracture. If a rough-walled fracture can be considered to locally behave like a pair of parallel plates (rather than as tubes), the entry pressure of the fracture is given by (Pruess and Tsang, 1990; Reitsma and Kueper, 1994):

$$P_c^* = \frac{2\sigma_{nw}\cos\theta}{b} \qquad (2.6)$$

where b is the aperture width of interest. If water is assumed to be perfectly wetting, the contact angle is $0°$ and (2.6) reduces to:

$$P_c^* = \frac{2\sigma}{b} \qquad (2.7)$$

NAPL enters the fracture when:

$$P_c > P_c^* \qquad (2.8)$$

Conversely, for NAPL already occupying a fracture, exit of NAPL from the fracture occurs when:

$$P_c < P_c^* \qquad (2.9)$$

where the pressure required to exit the fracture may be different than the fracture entry pressure due to a locally different aperture value at the exit point.

So, fractures with smaller apertures have larger entry pressures and hence require larger capillary pressures and, in turn, higher pool heights to force entry. Equations 2.8 and 2.9 collectively mean that the larger apertures are the first to receive and to discharge NAPL. These processes are somewhat temperature dependent; however, as temperature only shows a very small variation in the subsurface, it is valid in most cases to consider it to be constant.

The theory of capillary/entry pressure relationships has applications for traditional percolation theory. This approach assumes that fluid is distributed throughout the domain of interest in a steady-state distribution (Mendoza, 1992), implying that all accessible areas of a fracture where the capillary pressure exceeds the entry pressure are invaded by NAPL. This assumes that sufficient time is available for equilibration, and that capillary forces dominate over viscous forces. Quantification of whether or not the latter criterion is met has been expressed as the dimensionless capillary number (modified from McWhorter and Kueper, 1996):

$$N_c = \frac{\mu v}{\sigma} \qquad (2.10)$$

where v is the average linear velocity and μ is the fluid viscosity. When N_c is small (on the order of 10^{-4} or less), capillary forces dominate. What traditional percolation theory often does not account for, however, is that all areas of the fracture may not be available for flow. Further, some areas of the fracture may be disconnected from others due to contact points where the fracture closes off; also, some areas may not receive flow due to preferential channelling by the NAPL through the fracture. This has implications for dissolution and matrix diffusion as areas of the fracture that have more NAPL will be subject to these processes to a greater extent than "cleaner" areas. Although it is possible to modify traditional percolation theory using accessibility and trapping criteria, it still cannot be used in transient scenarios. Furthermore, traditional percolation theory does not consider viscous effects of active flow. With these restrictions, percolation theory precluded itself from being used in this study.

Capillary Pressure and Saturation

Small capillary numbers, where capillary forces dominate over viscous forces, validate the use of capillary pressure versus saturation curves. A capillary pressure versus saturation curve is considered to be primarily a function of pore/grain size and orientation, and hence is "unique" to a particular porous medium. The corollary to pore/grain size in porous media for fractures is the aperture width, where NAPL migration into the aperture segment is presumably "step-like" in nature. This means that the NAPL saturation in the segment increases rapidly after NAPL reaches the required entry pressure. These curves can be experimentally derived as a best-fit curve on a plot of capillary pressure versus saturation. Alternatively, several workers have put forth empirical equations to represent capillary pressure-saturation curves. Perhaps two of the most notable capillary pressure versus saturation relationships were presented by Brooks and Corey (1964) and van Genuchten (1980). The Brooks-Corey relationship is given by (Brooks and Corey, 1964):

$$S_e = \left(\frac{P_c}{P_d}\right)^{-\lambda} \tag{2.11}$$

where P_d represents the entry (or displacement) pressure, λ is the pore size distribution index, and S_e is the effective saturation of the given phase given by:

$$S_e = \frac{S_i - S_{r_i}}{1 - S_{r_i}} \qquad i = w, n \tag{2.12}$$

with S_i representing the phase saturation and S_{r_i} the phase saturation at residual. The relationship given by van Genuchten (1980) is:

$$S_e = \left[1 + \left(\frac{P_c}{P_d}\right)^{\frac{1}{1-m}}\right]^{-m} \tag{2.13}$$

where m is a fitting parameter based on model calibration.

Curves of capillary pressure versus saturation are useful in modelling two-phase flow because saturation is usually more easily measured than capillary pressure (Fetter, 1993), although both functions are quite difficult to measure in fractures at the microscale. An example curve of capillary pressure versus saturation typical of a
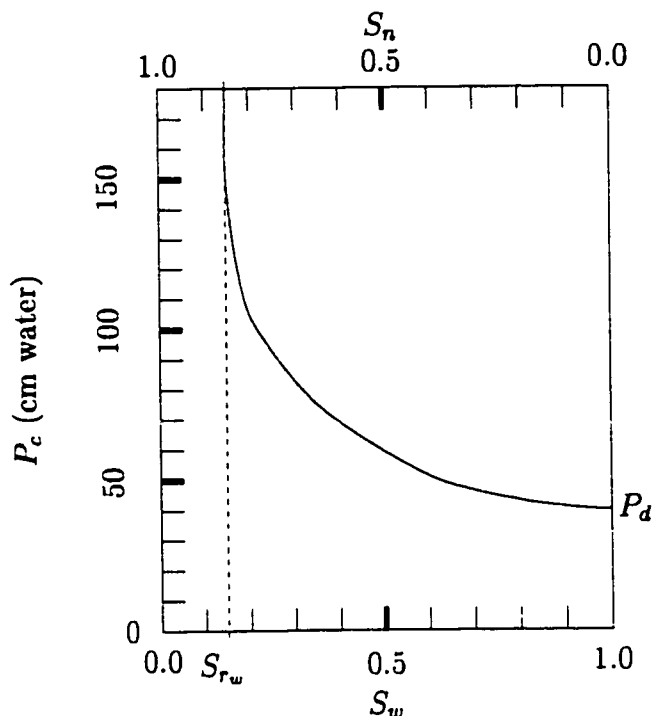
Figure 2.3: Sample capillary pressure versus saturation curve typical of a fine-grained sand.

fine-grained sand is shown is Figure 2.3. In addition, the concept of maintaining a small capillary number also means that, in most cases, the "viscous coupling effect" (Rose, 1993), or viscous drag that occurs across the macroscopic interface between different fluid phases, can be justifiably neglected.

Capillary Pressure Scaling

For similar media, it is often convenient to define a single dimensionless capillary pressure versus saturation curve and then "scale" the curve to account for differences in intrinsic permeability. Leverett (1941) derived the following relationship between capillary pressure and dimensionless capillary pressure:

$$P'_c = \frac{P_c}{\sigma} \left(\frac{k}{\phi}\right)^\alpha \qquad (2.14)$$

where P'_c is the dimensionless capillary pressure. Leverett originally found $\alpha = 0.5$; it is often treated in the literature as a fitting parameter (Kueper and McWhorter, 1991).

$$S_n$$
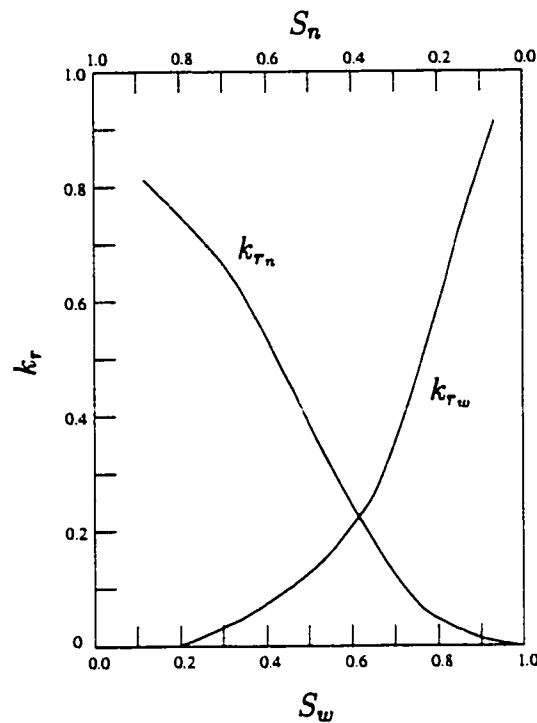
Figure 2.4: Typical relative permeability versus saturation curves for the wetting phase (k_{r_w}) and the non-wetting phase (k_{r_n}) (after Peaceman, 1977).

2.1.2 Relative Permeability and Saturation

For a single phase flowing by itself in a medium, the ability that the medium has to transmit fluid is given by its intrinsic permeability (Fetter, 1993). In two-phase flow, however, the presence of the second fluid phase may significantly impede the progress of the first phase, and vice versa. This effect requires the introduction of a dimensionless relative permeability term into Darcy's Law to account for the interference between phases. This term is usually taken to be a function of the fluid saturation. The relative permeability is expressed as a number between 0, which applies when none of the phase of interest is present $(S_i = 0, i = w, n)$, to 1, which applies when the medium is totally saturated with that phase $(S_i = 1.0, i = w, n)$ (Parker, 1989). As such, the permeability of the medium for a given fluid phase is given by the product of its intrinsic permeability and its relative permeability. Each phase will have its own intrinsic and relative permeability. Typical relative permeability versus saturation curves for two-phase flow are shown in Figure 2.4.

The relationship between relative permeability and saturation has been widely studied (Mercer and Cohen, 1990; Reeves and Celia, 1996). Brooks and Corey (1964) have presented the following two equations to describe relative permeability for both the wetting and non-wetting phases:

$$k_{r_w} = S_e^{(2+3\lambda)/\lambda} \tag{2.15}$$

$$k_{r_n} = (1 - S_e)^2 \left(1 - S_e^{(2+\lambda)/\lambda}\right) \tag{2.16}$$

where λ is determined from 2.11.

van Genuchten (1980) also derived a different representation using Mualem's (1976) k_r model for relative permeability versus saturation:

$$k_{r_w} = \sqrt{S_e} \left[1 - \left(1 - S_e^{1/m}\right)^m\right]^2 \tag{2.17}$$

$$k_{r_n} = \sqrt{(1 - S_e)} \left(1 - S_e^{1/m}\right)^{2m} \tag{2.18}$$

where m is the van Genuchten fitting parameter in 2.13.

2.1.3 Flow Equations

The mathematical equations used to represent the flow process are fundamental to any rigorous study into multiphase flow. Parker (1989) gives the following equations to represent multiphase flow in porous media:

$$q_{i_w} = -k_{r_w} \frac{k_{ij}}{\mu_w} \left[\frac{\partial P_w}{\partial x_j} + \rho_w g \frac{\partial z}{\partial x_j}\right] \tag{2.19}$$

$$q_{i_n} = -k_{r_n} \frac{k_{ij}}{\mu_n} \left[\frac{\partial P_n}{\partial x_j} + \rho_n g \frac{\partial z}{\partial x_j}\right] \tag{2.20}$$

where q is the volumetric flux density, or Darcy velocity, of phase w or n in the ith coordinate direction; k_r is the relative permeability of each respective phase; k_{ij} is the intrinsic permeability, with direction indices i and j repeated indicating summation in tensor notation; z is the elevation head; x_j is the jth Cartesian coordinate; ρ is the phase density (which may vary in space and time); and g is gravitational acceleration.

Note that the above equations are dependent upon the implicit assumption that flow is laminar so that it may be characterized by Darcy's Law, which states that flow velocity is directly proportional to hydraulic conductivity K and hydraulic gradient dh/dl (encompassing pressure, elevation, fluid density and viscosity, and gravitational acceleration). This also means that the Reynold's number, which gives the ratio of inertial forces to viscous forces, must be sufficiently low (Brown, 1987). In most cases, groundwater flows slowly enough that this requirement is easily met; however, forced advection in fractured media may be an important exception.

2.1.4 Continuity Equations

Also important in the study of flow is the idea of mass continuity, which requires that the amount of mass in a system be preserved. For multiphase flow, the continuity equations for each phase based on their simultaneous flow can be described in the following equations (Parker, 1989):

$$\phi \frac{\partial S_w}{\partial t} - \frac{\partial}{\partial x_i} \left[\frac{k_{ij} k_{r_w}}{\mu_w} \left(\frac{\partial P_w}{\partial x_j} - \rho_w g \frac{\partial z}{\partial x_j} \right) \right] + Q_w = 0 \qquad (2.21)$$

$$\phi \frac{\partial S_n}{\partial t} - \frac{\partial}{\partial x_i} \left[\frac{k_{ij} k_{r_n}}{\mu_n} \left(\frac{\partial P_n}{\partial x_j} - \rho_n g \frac{\partial z}{\partial x_j} \right) \right] + Q_n = 0 \qquad (2.22)$$

where ϕ is the medium porosity; μ_w and μ_n are the wetting and non-wetting phase viscosities, respectively; and Q_w and Q_n are source/sink terms for the wetting and non-wetting phases, respectively. In numerical modelling, a mass balance is often performed as a check on the stability of the solution (Celia et al., 1990; Celia and Binning, 1992); however, Celia et al. (1990) also point out that even solutions which are perfectly mass conservative may still suffer from instability. These continuity equations provide the basis for the two-phase flow implementation.

2.2 Dissolution

To this point, fundamental equations describing flow and continuity of water and NAPL have been presented without the inclusion of chemical interaction between

the two phases. Although NAPL is commonly considered to be immiscible with water, it does undergo limited dissolution into the aqueous phase to a maximum of its solubility limit. This creates a cause for concern as residual NAPL, or NAPL that is immobilized by capillary forces, may dissolve for very lengthy time periods at levels that create dissolved phase aqueous concentrations that are orders of magnitude higher than drinking water standards (Mercer and Cohen, 1990; Kueper and McWhorter, 1991). In addition, non-uniform dissolution may result in fingering, or NAPL ganglia which are disconnected from each other (Parker et al., 1996); these immobile "blobs" reduce the permeability of the medium or fracture to aqueous flow (Imhoff and Miller, 1996). This, in turn, may hinder remediation of contaminated media as most remediation strategies involve mobilizing the contaminants.

Dissolution will continue until either equilibrium is reached or the system is altered. A discussion of equilibrium versus kinetic or rate-controlled dissolution will be presented later in this section.

2.2.1 Dissolution as a Diffusive Process

Miller et al. (1990) and Powers et al. (1992), based on much earlier work, postulate that dissolution is a diffusive process that can be expressed as a quasi-steady approximation of Fick's first law:

$$J = -k_f(C - s) \tag{2.23}$$

where J is the net mass flux per unit volume of the species $[M]/[LT]$, C is the dissolved aqueous concentration for that constituent, s is the equilibrium concentration (solubility limit) for that constituent, and k_f is the mass transfer coefficient. The mass transfer rate is limited by diffusion across a boundary layer (Powers et al., 1992). As such, the mass transfer coefficient is directly proportional to the NAPL diffusion coefficient and inversely proportional to the thickness of the boundary layer. It is assumed that the concentration gradient is linear (i.e., that steady-state has been reached). For application to fractures, Equation 2.23 must be modified to account

for the interfacial area of the NAPL/water contact for fracture geometry (Banack, 1996). The modified form is:

$$J' = -b\omega k_f(C - s) \tag{2.24}$$

where J' is the total mass flux for the fracture $[ML^2]/[T]$, b is the aperture and ω is the width of an aperture segment.

Other models, such as the two-stage model and the dual-resistance model (Weber et al., 1991), are alternatives to the linear diffusion model. Discussion of these is beyond the scope of this thesis, but may be considered at a later time.

2.2.2 Equilibrium versus Rate-controlled Dissolution

Many studies (e.g., Parker et al., (1994)) consider dissolution as being an equilibrium process. This means that at all times, NAPL has dissolved to its solubility limit. This viewpoint does not consider the time that NAPL takes to dissolve into the aqueous phase. In reality, due to the presence of low NAPL saturations, the presence of heterogeneities in the porous media, or the effects of aqueous phase bypassing, residual NAPL saturation, or immobile NAPL blobs, result. These can be formed by "snap-off" mechanisms where pore throats are much smaller than pore bodies (Mercer and Cohen, 1990). The residual NAPL blobs contribute to long-term subsurface contamination in porous media and fractures as they may continue to dissolve and contaminate adjacent water for very lengthy time periods. In this case, aqueous phase concentrations that are significantly out of equilibrium may be observed (Mayer and Miller, 1996). In addition, residual NAPL may be remobilized as a result of increased hydraulic gradients (Kueper and McWhorter, 1991), and significantly expand the range of dissolved phase contamination.

Note that whether equilibrium or kinetic dissolution is appropriate may depend quite strongly on scale. It is very difficult to quantify the kinetic dissolution factor for a large problem, and it may not be feasible to define an equilibrium model for a problem when great levels of detail are required. The question of equilibrium versus

rate-controlled dissolution continues to be an area of active research (Frind *et al.*, 1999).

2.3   Aqueous Phase Transport

After some of the NAPL has dissolved into the aqueous phase, it can then be transported in porous media and fractures with bulk advection of water or due to concentration gradients. The dissolved phase is subject to the process of matrix diffusion, where some of the solute diffuses into the adjacent porous blocks. Calculations by Parker *et al.* (1994) postulate that the process of matrix diffusion is a significant mechanism for removing NAPL from the fracture.

2.3.1   Transport Equation

Aqueous phase transport may also be described by equations that mathematically represent the relevant physical and chemical processes that occur. The two-dimension, non-reactive transport equation as given by Freeze and Cherry (1979) for uniform porosity is:

$$-v_i\frac{\partial C}{\partial x_i} + \frac{\partial}{\partial x_i}\mathbf{D}_{ij}\frac{\partial C}{\partial x_j} = R\frac{\partial C}{\partial t} \qquad i,j = x,y \qquad (2.25)$$

where $\mathbf{D}_{ij}$ is the hydrodynamic dispersion coefficient, C is the aqueous phase concentration, x and y are Cartesian coordinate directions, v_i is the velocity in the ith direction, and R is the retardation factor. The first term represents advective (or bulk) movement of solute with groundwater flow, the second term represents dispersive movement of the tracer, and the right-hand term represents storage. The dispersion coefficient is a tensor that describes spreading due to the tortuous path the contaminant must take around soil grains through the pore space. To represent two-dimensional advection and dispersion in a fracture, Equation 2.25 may be rewritten as (Sudicky and Frind, 1982):

$$-bv_i\frac{\partial C}{\partial x_i} + \frac{\partial}{\partial x_i}b\mathbf{D}_{ij}\frac{\partial C}{\partial x_j} = bR\frac{\partial C}{\partial t} \qquad i,j = x,y \qquad (2.26)$$

to take into account fracture aperture (b). Note that the hydrodynamic dispersion term, D_{ij}, is a function of fracture dispersivities α_L (along flowpath) and α_T (transverse to flowpath), respectively; D_{ij} is also a function of the average groundwater velocity in the ith or jth coordinate direction v_i and v_j, their Euclidean norm $v = \sqrt{v_x^2 + v_y^2}$, and the effective diffusion coefficient D^* (Fetter, 1993). The preceding statements may be described mathematically by the following relationship:

$$D_{ij} = (\alpha_L - \alpha_T)\frac{v_i v_j}{|v|} + \alpha_T |v| + D^* \qquad (2.27)$$

where α_L and α_T are the longitudinal and transverse dispersivities, respectively.

Matrix Diffusion

After the water and NAPL have been introduced into the fracture and dissolution has begun, the dissolved phase may migrate into the surrounding porous blocks. This process, known as matrix diffusion, removes dissolved phase NAPL from the fracture by diffusion into the matrix. Note that this is predicated on the need for the matrix to have appreciable porosity. If this is not the case, NAPL will continue to dissolve until it is completely flushed away by invading water (after NAPL invasion has halted).

Diffusion in one dimension is commonly described by Fick's first and second laws (Fetter, 1993):

$$F_i = -\phi D^* \left(\frac{\partial C}{\partial x}\right) \qquad (2.28)$$

$$\frac{\partial C}{\partial t} = D^* \left(\frac{\partial^2 C}{\partial x^2}\right) \qquad (2.29)$$

where F_i is the mass flux of solute per unit area per unit time in the ith coordinate direction.

Sorption

Sorption is a process which may remove contaminants from the mobile aqueous solution. It involves chemical interaction between the dissolved contaminant and the

solid matrix, and is described by a partitioning coefficient K_d. Both matrix diffusion and sorption create an additional obstacle for subsurface remediation, as fresh water flushing by the NAPL-adsorbed sites is subject to NAPL contamination by the reverse concentration gradient created from the porous matrix, where NAPL concentrations are high, to the fresh water in the fracture. Clean water in the fracture may also be subject to contamination from reverse partitioning from the matrix. Sorption is not considered in this study; therefore, concentrations in the fracture may be overestimated.

Chapter 3

Model Development and Verification

A numerical model was developed to simulate coupled two-phase flow and dissolved-phase transport in a rough-walled fracture and the surrounding porous matrix. This model, **FaTMatD** (**F**low **a**nd **T**ransport with **Mat**rix **D**iffusion) is based on Swanflow2D (Faust and Rumbaugh, 1990), which simulates the flow of oil and water in porous media.

3.1   Overview of Swanflow2D

Swanflow2D is a block-centered finite-difference model which simulates simultaneous flow of water and a completely immiscible fluid in two-dimensional heterogeneous porous media. The model is capable of performing the simulations either in the saturated zone or in the unsaturated zone. A passive air phase, which moves only in response to displacement by other phases, is assumed in the unsaturated zone. Due to the non-linearities inherent in a two-phase flow simulation, a full Newton-Raphson iteration scheme is used to solve for the dependent variables of water saturation and non-aqueous phase liquid pressure. Heterogeneity and anisotropy are permitted. Two-phase flow implementation specifics of the Swanflow2D model are discussed in detail in Faust (1985) and Faust and Rumbaugh (1990), and hence are not repeated

here.

The original model was verified as working correctly for a number of test cases, which included a comparison between Swanflow2D, another numerical model, and the analytical solution presented by Buckley and Leverett (1942) for a linear waterflood of a petroleum reservoir. A petroleum reservoir with an initial NAPL saturation of 0.84 was subsequently flooded with water. These verification simulations were repeated following modifications to the code for this study to confirm that the two-phase flow component was not inadvertently altered.

3.1.1 Summary of Dependent Variables

The coupled two-dimensional equations describing simultaneous water and NAPL flow posed in terms of the dependent variables of water saturation and NAPL pressure are given by:

$$\theta \frac{\partial S_w}{\partial t} - \frac{\partial}{\partial x_i} \left[\frac{k_{ij} k_{r_w}}{\mu_w} \left(\frac{\partial P_n - P_c}{\partial x_j} - \rho_w g \frac{\partial z}{\partial x_j} \right) \right] + Q_w = 0 \qquad (3.1)$$

$$\theta \frac{\partial (1 - S_w)}{\partial t} - \frac{\partial}{\partial x_i} \left[\frac{k_{ij} k_{r_n}}{\mu_n} \left(\frac{\partial P_n}{\partial x_j} - \rho_n g \frac{\partial z}{\partial x_j} \right) \right] + Q_n = 0 \qquad (3.2)$$

Initial conditions must be specified by the user for both of the dependent variables. Type I boundary conditions may be specified by the user, where selected grid blocks are constrained to the water saturation and NAPL pressure values initially assigned by the user. All other boundary blocks default to Type II (zero flux normal to the boundary).

Equations 3.1 and 3.2 are coupled though the water saturation and capillary pressure equations, given in Section 2.1 as:

$$S_w + S_n = 1 \qquad (3.3)$$

$$P_c = P_n - P_w \qquad (3.4)$$

Swanflow2D solves 3.1 and 3.2 simultaneously for the dependent variables of water saturation and NAPL pressure, and then uses these and 3.3 and 3.4 to calculate the other output parameters (water pressure, NAPL saturation).

3.2 Grid

Simulations were carried out on three-dimensional grids composed of grid blocks with constant width and height but variable depth (to represent the aperture). Figure 3.1 shows the fracture grid block conceptualization, as well as the nodal points at which parameters are defined and dependent variables determined. The plane which cuts the fracture in half acts as a symmetry boundary for matrix diffusion.

The fracture was conceptualized as being embedded in a low permeability, porous rock matrix. This representation assumes that the matrix permeability is sufficiently low so as to not allow advective free-phase fluid flow to a significant degree. Consequently, diffusion into and within the matrix are the only transport processes modelled in the matrix. Figure 3.2 schematically demonstrates the matrix grid block discretization used in model simulations. The spacing was chosen to approximate a semi-infinite domain for diffusion. The number of grid blocks required orthogonal to the fracture is largely a function of the strength of the diffusive process as well as the physical size of the domain. The dimensions of the grid blocks were chosen so as to approximate as closely as possible continuous planes of nodal points (see Figure 3.2).

3.3 Solver

One of the primary drawbacks of using Swanflow2D in its original form included Swanflow2D's use of a Gauss-Doolittle direct solver. Behie and Vinsome (1982) indicate that, because iterative solvers are less memory-intensive and may require fewer computations, an iterative solver would likely increase computational speed and efficiency compared to a direct solver. The iterative block solver FIVEPTB, developed at the University of Alberta by Mendoza, was implemented and verified as working correctly through a reverification of the linear waterflood simulation (Section 3.1).

26
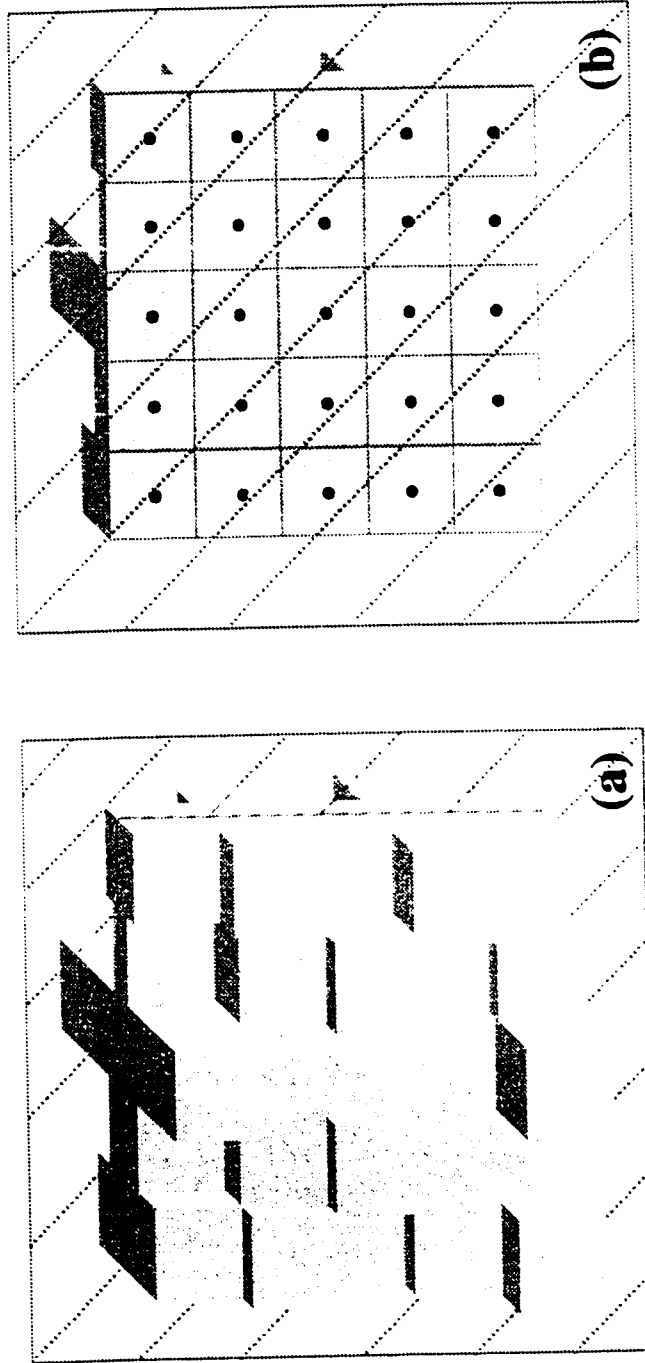
Figure 3.1: Three-dimensional conceptual diagram of fracture aperture blocks used in the numerical model. (a) The fracture blocks. (b) The bisected fracture with a symmetry boundary along the centre. The black dots in the centres of the grid blocks represent nodal points, or the points at the centroids of the blocks that are assigned input and output properties.
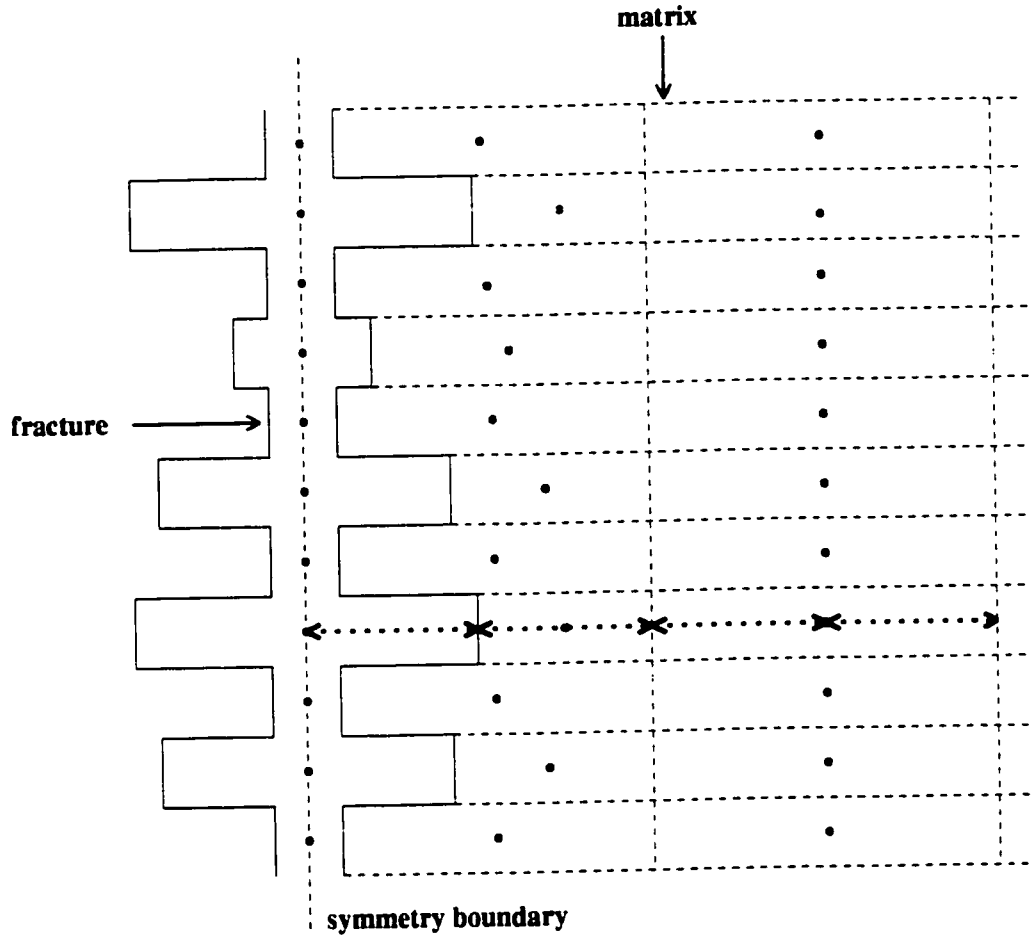
Figure 3.2: Cross section of fracture and matrix showing grid block spacing into the matrix. The first matrix block has variable spacing such that all blocks terminate along the same plane. The second matrix block has a depth of the largest half aperture. Each subsequent matrix block after the second increases geometrically by a factor of four times the depth of the block preceding it. Note that the horizontal scale is exaggerated relative to the vertical scale.

3.3.1 Iterative Solver

Behie and Vinsome (1982) give the following outline for the development of an iterative solver. The iterative block solver FIVEPTB solves simultaneously for more than one equation or unknown at each nodal point. In this case, the unknowns are water saturation and NAPL pressure. The matrix equation for one unknown, in general terms, is given by:

$$Ax = r^o \qquad (3.5)$$

where A is the original matrix, x is the solution vector, and r^o is the original residual. The matrix A is subsequently approximated by the sum of a lower triangular matrix L, a diagonal matrix D, and an upper triangular matrix U, so that $A = LDU$. This is known as incomplete LU factorization, and is generally carried out because it can be very costly to factor the original matrix directly. A forward substitution is performed, followed by a backward substitution, to obtain a first approximation to the change in x. The process is then repeated until convergence is achieved. Convergence will be discussed more fully in Section 3.9.

In addition, ORTHOMIN acceleration is used as it is the most suitable technique for strongly non-symmetric matrices arising from a fully implicit oil-water flow simulation. This technique involves performing a number of orthogonalizations which act to reduce the number of iterations required considerably. Further details of this acceleration technique are given in Behie and Vinsome (1982).

3.3.2 Results of Direct Versus Iterative Solver Comparison

For the base flow run used (see Chapter 4), the iterative solver increased computational efficiency, and hence decreased central processing unit (CPU) time, by roughly nine times. Thus, the implementation of the iterative solver was very important in the timely completion of the study, and, because iterative solvers are less prone to accumulated roundoff errors (Behie and Vinsome, 1982), this implementation may also have led to more accurate solutions.

3.4 Aperture Characterization

Fields of exponentially-correlated, log-normally distributed apertures were generated with the computer program FGen (Robin *et al.*, 1993). The resulting output was then read into the model such that each grid block on the fracture plane was assigned an aperture. Each aperture field had a specified log mean aperture ($\overline{Y}$) and log-aperture variance (σ_Y^2), as well as a degree of spatial correlation (λ_{sp}). The degree of correlation expresses the likelihood of the aperture of one grid block being statistically similar to the apertures of its surrounding neighbors. This type of aperture distribution has been shown to reasonably emulate the aperture distribution observed in real fractures (Moreno *et al.*, 1988; Reitsma and Kueper, 1994; Abdel-Salam and Chrysikopoulos, 1996). Figure 3.3 shows one fracture aperture distribution used in the model studies. The parameters are given in the figure caption.

3.5 Capillary Pressure and Saturation Relations

To reiterate what was stated in the previous section, each fracture grid block was assigned an aperture. Hence, each grid block has an associated intrinsic permeability characterized by the "cubic law" (see Section 2.0.3). Grid blocks with different apertures will exhibit different capillary pressure and relative permeability behaviour for given water saturations. As a result, each unique aperture requires the definition of unique capillary pressure versus saturation and relative permeability versus saturation curves. For the large number of grid blocks with differing aperture values simulated, it is prohibitively expensive in terms of memory and computational efficiency to input all of these different curves as model inputs. As a result, the capillary pressure scaling procedure developed by Leverett (1941) was implemented.

The basic theory behind Leverett-J capillary pressure scaling was outlined in Section 2.1.1. For the purposes of modelling, a reasonable assumption was made that small-scale heterogeneities were similar from one block to another. A dimensionless capillary pressure curve was generated using Brooks-Corey relationships (Equations
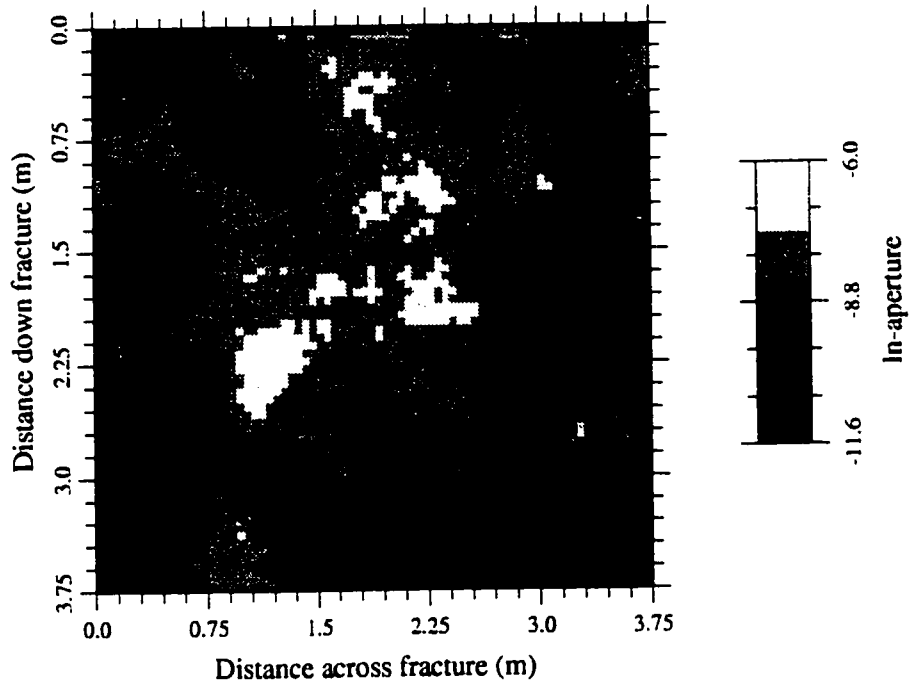
Figure 3.3: Fracture aperture distribution for $\overline{Y} = -8.8$ (corresponding to a geometric-mean aperture of approximately 150 $\times 10^{-6}$ m) and $\sigma_Y^2 = 0.65$. The dark coloured areas show smaller apertures. The grid is composed of 75 aperture blocks each with a width and height of 0.05 m. This aperture field is used for the base case (see Chapter 4).
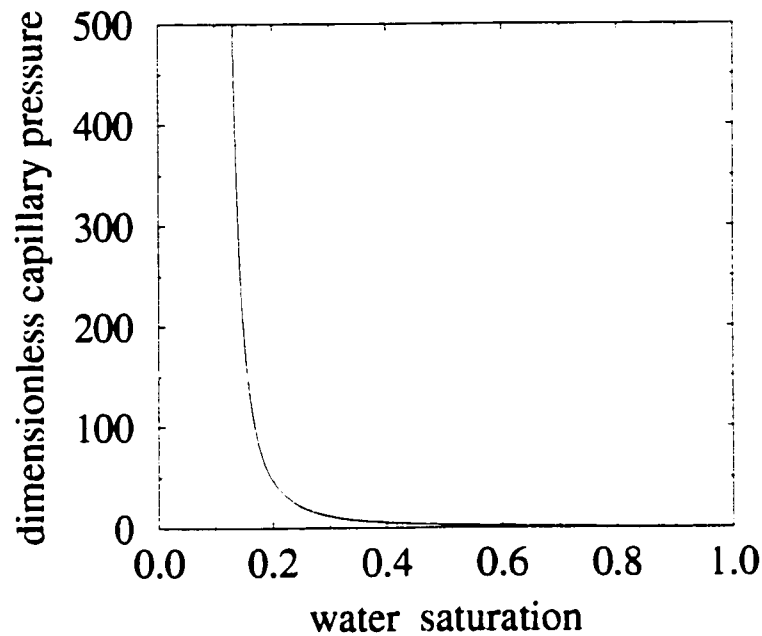
Figure 3.4: Dimensionless capillary pressure versus saturation curve used in base flow runs. The curve was generated with $\lambda = 1$, $S_{r_w} = 0.1$, and $\phi_f = 1$.

2.11 and 2.12) and was subsequently scaled to become a unique, dimensional capillary pressure curve for each unique aperture. As only one curve was used, with a simple one-line calculation to convert from dimensionless to dimensional capillary pressure, a considerable savings in computational time and memory were expected. A similar procedure was used to scale dimensionless relative permeabilities to dimensioned relative permeabilities. The primary dimensionless capillary pressure curve used is shown in Figure 3.4.

The relative permeability versus saturation curves used are shown in Figure 3.5. The parameters for both graphs are given in the figure captions. The parameters chosen for simulations are consistent with previous work by Kueper and McWhorter (1991) and Slough et al. (1999) as being representative of real aperture capillary pressure behaviour.
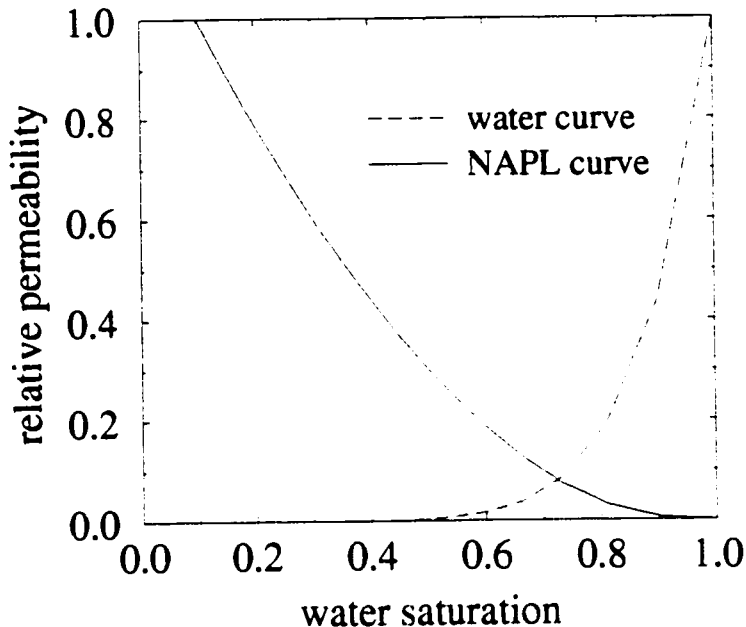
Figure 3.5: Relative permeability versus saturation curve used in base flow runs. The curve was generated with $\lambda = 1$, $S_{r_w} = 0.1$, and $\phi_f = 1$. Refer to Figure 3.4 for the capillary pressure versus saturation curve.

3.6   Flow Simulation

All of the simulations were conducted in essentially the same fashion. A water flow run with a specified average gradient up or down the fracture was initially set up and run until the solution for water pressure reached steady state, or did not change from one time step to the next. Then NAPL, with a specified saturation consistent with the NAPL pressure, was placed at the top of the fracture and the simulation was restarted. This latter procedure more accurately represents the true physical system, where water is assumed to be flowing for some time before NAPL is introduced.

Due to the non-linearities inherent in the flow formulation, the original authors implemented into Swanflow2D a fully-implicit treatment of the non-linear terms, with the relative permeability terms having upstream weighting. The nonlinear equations are then linearized using a residual formulation with Newton-Raphson iteration (Faust and Rumbaugh, 1990). In the Newton-Raphson iteration scheme, a Taylor Series expansion is performed about an assumed solution for the finite difference

equations, leading to a linearized matrix equation. This assumed solution is the solution at the previous iteration or time level. Huyakorn and Pinder (1983) observed that this method tends to converge quite rapidly. Convergence is determined by performing a mass balance for each fluid and comparing them to the given tolerances (Faust and Rumbaugh, 1990). The reader is referred to Faust (1985) and Faust and Rumbaugh (1990) for details regarding the implementation of the flow equations into the original code.

3.7 Transport Implementation

As NAPL flows in the fracture, mass is transferred from the free-phase to the aqueous (dissolved) phase via dissolution. This mass is then available to be transported in the fracture by advection and hydrodynamic dispersion, and is also available to diffuse into the porous matrix via molecular diffusion. These processes were incorporated into the model.

3.7.1 Governing Matrix Equation

The partial differential equations for transport were given in Equation 2.25. The overall matrix equation implemented into the numerical model is given by:

$$\left(\beta \left[A\right] - \frac{1}{\Delta t} R\left[T\right]\right) \{c^{t+\Delta t}\} = \left((1-\beta)\left[A\right] + \frac{1}{\Delta t} R\left[T\right]\right) \{c^t\} \qquad (3.6)$$

where β is the time weighting factor, A is the coefficient matrix, Δt is the time step size, R is the retardation factor, T is the contaminant storage matrix, and $\{c^{t+\Delta t}\}$ and $\{c^t\}$ are the concentrations at time $t + \Delta t$ and time t, respectively.

β - Time Weighting

The time weighting factor defined above expresses the degree to which the solution is evaluated based on known (old) values or on unknown (new) values. It may range from 0 for a fully explicit solution to 1 for a fully implicit solution. When β is equal

to 0, the solution becomes a forward difference approximation as $\{c^{t+\Delta t}\}$ is evaluated based on known or old values of c (i.e., $\{c^t\}$). Conversely, the fully implicit time weighting scheme ($\beta=1$) is known as the backward difference approximation. That is, values of $\{c^{t+\Delta t}\}$ are obtained as a simultaneous solution of linear equations at the $t + \Delta t$ time level (Wang and Anderson, 1982). One advantage of the fully implicit scheme is that it is unconditionally stable for linear problems, while the explicit scheme, particularly with relatively large time steps, is often unstable and prone to oscillations. One disadvantage of using implicit time weighting is that solutions are often smeared. Common alternatives to using either of these time weighting schemes are to use the Galerkin ($\beta = 0.66$) or Crank-Nicholson ($\beta = 0.5$) time weighting factors (Huyakorn and Pinder, 1983).

A - Coefficient Matrix

The coefficient matrix is calculated as the nodal sum of several components. The first component describes the contribution of the transport of mass via advection. It is the product of the surface area of connection between the blocks and the average linear groundwater velocity. A central difference approximation in space, where the advective term is averaged across the block between its neighbors, was used on all internal blocks. However, at boundaries, either a forward difference or backward difference approximation (as appropriate) was used to avoid extrapolating outside the domain. In these cases, the advective term was calculated from the grid block in question to its internal neighbor.

The second and third components of the coefficient matrix are calculated in a similar fashion to one another. They are the nodal contributions from mechanical dispersion and molecular diffusion, respectively. They are calculated as the product of the surface area of connection between blocks divided by the distance between nodes, the dispersion (or diffusion) coefficient, and the block porosity. In the fracture, these are calculated for all blocks; in the matrix, however, the contribution for molecular diffusion is the only transport mechanism considered. Harmonic weighting of the

apertures was used in all cases when calculating the surface area between blocks for processes acting parallel to the fracture plane.

T - Contaminant Storage Matrix

The contaminant storage matrix expresses how much mass is stored internally in a block in one time step, and is very important in ensuring that all mass is accounted for. It is calculated as the product of the retardation factor, the block volume, the block porosity, and the water saturation.

3.7.2 Solution Procedure

Initially, the Darcy velocities for the aqueous phase are calculated from the flow solution. Subsequently, coefficient matrix A is formed, which is followed by the creation of the full left- and right-hand sides of Equation 3.6 with the exception of the unknown concentrations. The matrix equation is then solved using a seven-point iterative solver SEVNPT developed by Mendoza. The solver description is similar to that given for the flow solver; however, only one set of equations is solved at each grid block in three directions (two parallel, and one orthogonal, to the fracture plane).

3.8 Coupling of Flow and Transport

Recall that the major objective of this study was to investigate system behaviour when flow, dissolution, and transport happen simultaneously. Therefore, a method to numerically couple flow and transport was required.

The basic algorithm is illustrated in Figure 3.6. The solution begins a step forward in time with the calculation of the flow solution as described in Section 3.6. Blocks which contain a minimum NAPL saturation value of 0.1% could subsequently participate in dissolution. The implementation of a threshold required saturation was required for the numerical stability of the model; with insufficient NAPL in a block for dissolution, the NAPL front jumps back and forth between iterations. As

```
┌─────────────────────────────┐
│    BEGIN LOOP OVER TIME     │
└─────────────────────────────┘
              ↓
┌─────────────────────────────────┐
│ SOLVE FOR FLOW OF WATER AND NAPL │
└─────────────────────────────────┘
              ↓
┌─────────────────────────────────┐
│   CONSTRAIN ALL BLOCKS HAVING   │
│      NAPL IN THEM TO C=s        │
└─────────────────────────────────┘
              ↓
┌──────────────────────────────────────────┐
│ SOLVE FULL TRANSPORT WITH MATRIX DIFFUSION │
└──────────────────────────────────────────┘
              ↓
┌──────────────────────────────────────────┐
│  BACK-CALCULATE MASS FLUX FROM NAPL TO    │
│ WATER – THIS GIVES THE RATE OF DISSOLUTION │
└──────────────────────────────────────────┘
              ↓
        ┌────────────────────────────┐
        │ PUT MASS FLUX TERM INTO FLOW │
        │  EQUATION AS A SINK TERM    │
        └────────────────────────────┘
              ↓
┌─────────────────────────────┐
│     END LOOP OVER TIME      │
└─────────────────────────────┘
```
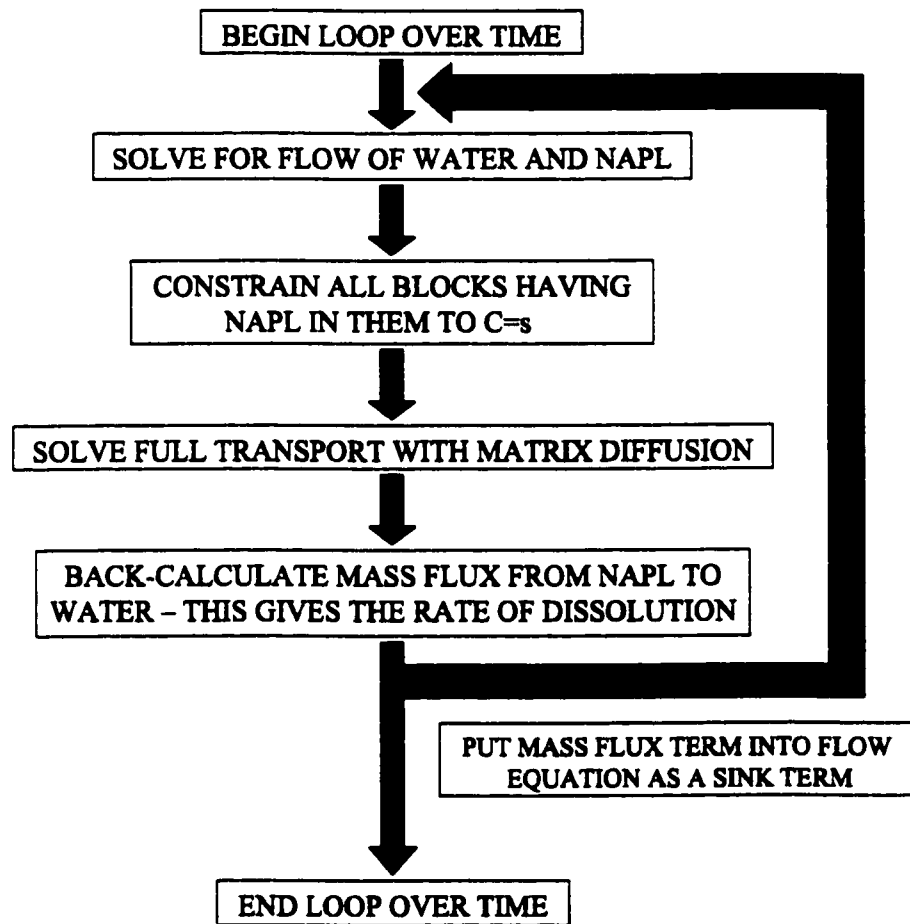
Figure 3.6: Model flow in FaTMatD.

a result, the solution does not converge. The dissolution-eligible blocks are subsequently given a concentration value equal to their user-inputted aqueous solubility. The transport solution is then obtained as discussed in Section 3.7.

After the transport solution has been completed, the dispersive mass flux or dissolution rate in the constrained blocks is determined. This is accomplished by multiplying the original coefficient matrix by the new concentration vector and then subtracting the right hand side (see Equation 3.6). The original flow solution is then resolved with the dissolution rate acting as the sink term Q_n in the two-phase flow equations (see Equations 2.22 and 3.2). The process is repeated until both the flow and transport solutions converge to within their respective convergence tolerances or convergence norms.

3.9 Implementation of Convergence Norms

3.9.1 Flow Solution

Due to the added consideration of dissolution, the mass balance convergence criteria implemented for flow was made more rigorous by insisting that the dependent variables of water saturation and NAPL pressure must also have reached steady values from one iteration to the next. To this end, the widely accepted concept of the norm, or metric, was adapted (Protter and Morrey, 1991; Medina and Carrera, 1996).

In the flow iteration, for the dependent variable of water saturation (see Section 2.1.4), a "Euclidean norm" is used:

$$E_n^{nr} = \sqrt{\sum_{i=1}^{i=N_b} \left(S_{w_i}^{nr} - S_{w_i}^{nr-1} \right)^2} \tag{3.7}$$

where E_n^{nr} is the Euclidean norm for the Newton-Raphson iteration, N_b is the total number of blocks in the fracture, $S_{w_i}^{nr}$ is the water saturation solution at block i after the present Newton-Raphson iteration, and $S_{w_i}^{nr-1}$ is the water saturation solution after the previous Newton-Raphson iteration. The calculated Euclidean norm is then compared to an input Euclidean tolerance (E_{tol}). The flow solution continues

to iterate until $E_n \leq E_{tol}$.

The Euclidean norm is suitable for comparisons where the range of dependent variables is expected to vary between 0 and some small, predetermined value (in this case, 1). It then becomes relatively easy to choose an appropriate value for E_{tol}. In cases where the values of the dependent variable are not known ahead of time, it is much more difficult to assign a value to E_{tol}. To circumvent this difficulty, the l_1 norm, which is very well known in mathematical analysis (Protter and Morrey, 1991), was adopted by normalizing the norm to the average test value. For the dependent variable of NAPL pressure, the formulation of this norm is:

$$l_1^{nr} = \sum_{i=1}^{i=N_b} \frac{\left| P_{N_i}^{nr} - P_{N_i}^{nr-1} \right|}{\frac{1}{2}\left(P_{N_i}^{nr} + P_{N_i}^{nr-1}\right)} \tag{3.8}$$

where l_1^{nr} is the normalized l_1 norm for the Newton-Raphson iteration, $P_{N_i}^{nr}$ is the NAPL pressure of block i after the present Newton-Raphson iteration, and $P_{N_i}^{nr-1}$ is the NAPL pressure of block i after the previous Newton-Raphson iteration. This formulation allows greater ease in determining an appropriate NAPL pressure norm. The Newton-Raphson iteration was considered to be converged when at least one of the calculated norms was less than the norm criteria values given in the input file.

3.9.2 Coupled Solution

With minor differences, the norms described above were also used to define convergence of the coupled flow and transport solution. The equations are adapted as follows:

$$E_n^{cp} = \sqrt{\sum_{i=1}^{i=N_b} \left(S_{w_i}^t - S_{w_i}^{t-1}\right)^2} \tag{3.9}$$

$$l_1^{cp} = \sum_{i=1}^{i=N_b} \frac{\left| P_{N_i}^t - P_{N_i}^{t-1} \right|}{\frac{1}{2}\left(P_{N_i}^t + P_{N_i}^{t-1}\right)} \tag{3.10}$$

$$E_n^{con} = \sqrt{\sum_{i=1}^{i=N_b} \left(c^t - c^{t-1}\right)^2} \tag{3.11}$$

where the variables are as described above, with the superscript cp indicating that the norm applies to the coupled solution and the superscript con indicating that the norm

applies to the concentration solution. The dependent variables were compared at the $t - 1$ and t time level, respectively. Two of the three norms (saturation, pressure, and concentration) must have converged to below their input tolerances before the coupled solution is considered converged, although convergence of all three norms generally occurred.

3.10 Model Verification

Due to the complexity of the finished numerical model, a suitable model for a comprehensive, overall verification was not available. Therefore, as is commonly done with numerical models (Zheng, 1990; Guiguer et al., 1994), simplified simulations were tested against various analytical solutions. The following sections outline the verification exercises undertaken in the model development.

3.10.1 Flow Verification

The verification exercise for two-phase flow performed by Faust and Rumbaugh (1990) was described in Section 3.1. Each time the code was significantly altered, this verification exercise was rerun to ensure that the model was still running correctly. This verification exercise was the only one originally run by the authors of Swanflow2D.

3.10.2 Transport Verification

The transport solution was tested against a number of analytical solutions. The following sections summarize these verifications.

Molecular Diffusion

A test case run was set up such that a specified concentration of 1000 mg/l was placed at the top of the fracture and at the top of the porous matrix. A transport solution was then run in the absence of advective water flow. The results of the test case
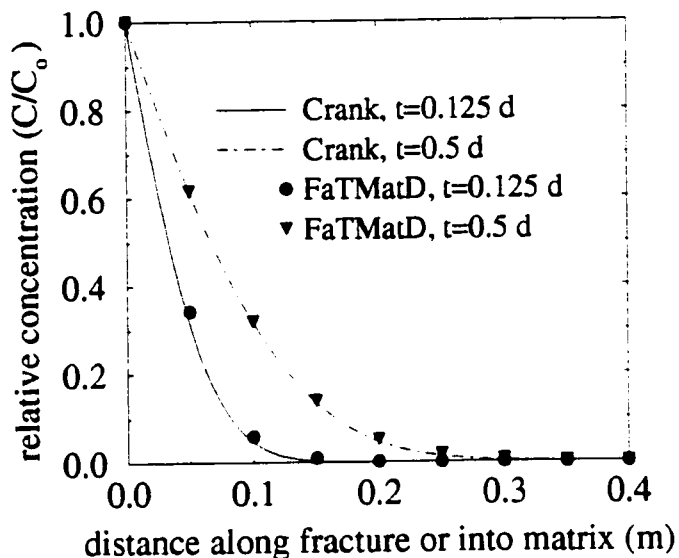
Figure 3.7: Crank's diffusion solution versus FaTMatD for one-dimensional diffusion only, plotted as a function of concentration relative to source concentration.

were verified against the diffusion solution reported by Crank (1956). The analytical solution is given as follows:

$$\frac{C}{C_o} = \text{erfc}\left(\frac{x}{\sqrt{(4D^*t)}}\right) \tag{3.12}$$

where C is the concentration solution, C_o is the source concentration at $x = 0, t \geq 0$, x is the position in space, D^* is the molecular (free) diffusion coefficient, t is the time, and erfc is the complementary error function. The results for one verification run are given in Figure 3.7. The diffusion coefficient used was 0.01 m^2/d.

Advective-Dispersive Transport

In order to test the advection and dispersion implementation, a simulation was set up such that the top row of the fracture was constrained with a specified concentration of 1000 mg/l. Diffusion into the matrix was not simulated for this verification exercise. The simulation parameters are given in Table 3.1.

parameter name	value	units
grid discretization $x \times z$	0.1 × 0.1	m
flow velocity v	0.1	m/d
diffusion coefficient D^*	0.01	m²/d
dispersion coefficient D_l	0.01	m²/d

Table 3.1: Parameters for Ogata-Banks and Craflush verification exercises.

The advection and hydrodynamic dispersion capabilities were tested against the advection/dispersion solution developed by Ogata and Banks (1961). The analytical solution is given as follows:

$$\frac{C}{C_o} = \frac{1}{2}\left[\text{erfc}\left(\frac{x - vt}{\sqrt{4Dt}}\right) + \exp\left(\frac{vx}{D}\right)\text{erfc}\left(\frac{x + vt}{\sqrt{4Dt}}\right)\right] \qquad (3.13)$$

where C is the concentration solution, C_o is the specified concentration, x is the position in space, v is the groundwater velocity, D is the hydrodynamic dispersion coefficient, t is the time, and erfc is the complementary error function. The results for one verification run are given in Figure 3.8.

In addition, the model was verified against the pseudo-analytical model Craflush (Sudicky, 1988). Results similar to those seen in Figure 3.8 were obtained. The results are not presented here.

Full Advective-Dispersive Transport with Matrix Diffusion

A total comparison of all transport components was completed against Craflush (Sudicky, 1988). Simulation parameters are again given in Table 3.1, with constrained concentrations on the top of the fracture. The parameters are given in Table 3.1. In addition to full advective-dispersive transport in the fracture, diffusion into the porous matrix was also simulated. The results of one such simulation are shown in Figure 3.9.
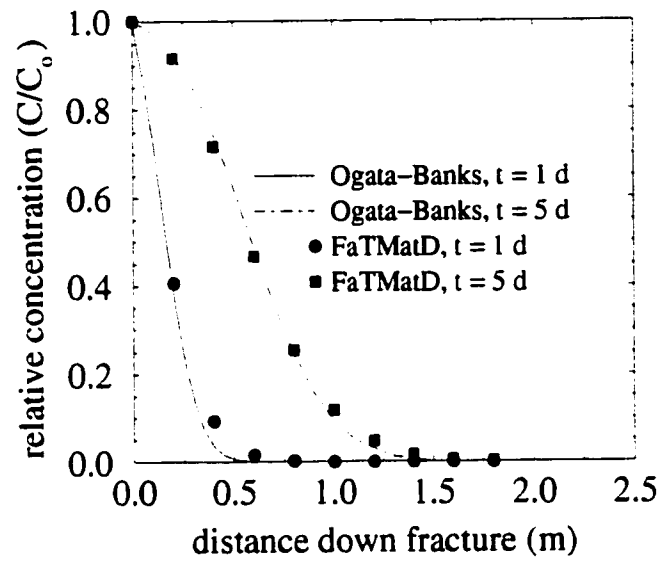
Figure 3.8: The Ogata-Banks solution versus FaTMatD for advective-dispersive transport in the fracture only, plotted as a function of concentration relative to source concentration.
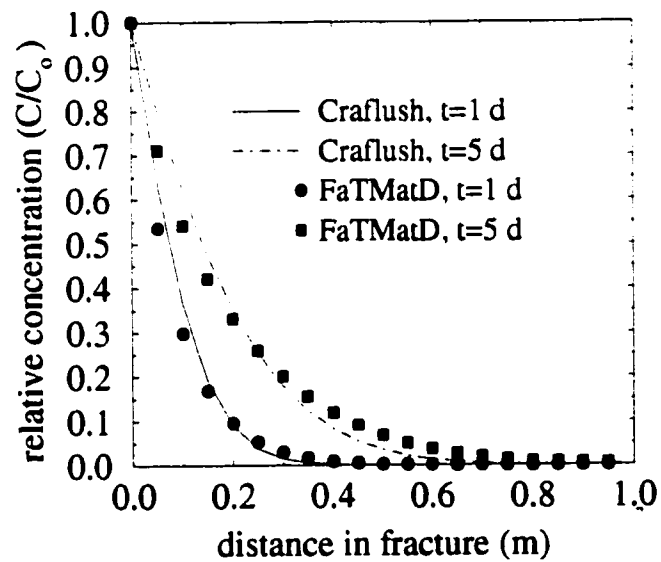
Figure 3.9: Craflush versus FaTMatD for full advective-dispersive transport with matrix diffusion, plotted as a function of concentration relative to source concentration.

3.11 Summary

The final numerical model solves for coupled two-phase flow with dissolution and advective-dispersive transport in the fracture, with matrix diffusion into the surrounding porous matrix. Care was taken to perform the smallest number of necessary operations and limit the amount of memory used. The finished product enabled further research to be conducted. The results of some of the simulations run will be presented in the next chapter.

Chapter 4

Results and Sensitivity Analysis

The computer model developed was used to simulate flow, dissolution, and aqueous phase transport with matrix diffusion in a rough-walled fracture. A variety of different conditions were tested in order to determine the sensitivity of the system to different input parameters. Most simulations were conducted with some form of dissolution; however, a flow simulation in the absence of dissolution was also simulated as a basis for comparison.

Other researchers have conducted studies in this area. For example, Kueper and McWhorter (1992) examined the behaviour of DNAPLs in a rough-walled fracture in the absence of dissolution, and Parker et al. (1994) examined the behaviour of dissolution and matrix diffusion from parallel plate fractures in the absence of NAPL/water flow. Sudicky and Frind (1982) simulated matrix diffusion in rough-walled fractures in the absence of free-phase contaminant. Ross and Lu (1999) demonstrated through the use of a computer model that matrix diffusion can be important in allowing the remobilization of free-phase NAPL pooled above small apertures after a potentially long period of residence time, where the decrease in mass flux from the fracture into the matrix over time allows the capillary pressure to increase and eventually exceed the entry pressure of the next aperture segment. Recently published is a study by Esposito and Thomson (1999), who developed a numerical model that also couples DNAPL flow with transport and matrix diffusion in a discrete fracture, although dissolution is only simulated after a number of transport solutions. It was not clear

44

from this research the criteria that they used in order to determine when coupling flow and transport together becomes important in the course of a simulation. This study did not focus on this issue.

4.1 Base Flow Scenario

A base case simulation was developed to act as a basis for comparison in the ensuing sensitivity analysis. This simulation was designed to be sufficiently simple while providing a clear picture of system behaviour. The base flow simulation is described in the following sections.

4.1.1 Grid Discretization

A 3.75 m by 3.75 m grid composed of 75 grid blocks in each of the x and z coordinate directions and 7 blocks in the orthogonal (y) coordinate direction was specified. The blocks had a discretization of 0.05 m in each of the x and z directions, with discretizations in the y direction given by the aperture. The discretization procedure for subsequent "layers" into the matrix (i.e., in the y direction) was described in Section 3.2. Figure 3.2 shows the conceptual grid discretization used in the y direction.

4.1.2 Aperture Characterization

The base flow simulation was simulated with an aperture field with $\overline{Y} = -8.8$ and $\sigma_Y^2 = 0.65$. This corresponds to a geometric-mean aperture of approximately 150×10^{-6} m, with apertures ranging from 15×10^{-6} m to 2300×10^{-6} m. The aperture field is shown in Figure 3.3.

4.1.3 Capillary Pressure Scaling

As explained in Section 3.5, a dimensionless capillary pressure curve was generated using Brooks-Corey relationships. The curve parameters are reiterated in Table 4.1. The graph of the dimensionless capillary pressure versus saturation curve used is

Parameter Name	Symbol	Value	Units
pore size distribution index	α	1.0	-
residual wetting phase saturation	S_{r_w}	0.1	-
fracture porosity	ϕ_f	1.0	-
interfacial tension	σ	0.04	N/m

Table 4.1: Parameters for Brooks-Corey capillary pressure definition and Leverett-J capillary pressure scaling.

shown in Figure 3.4. The curve created from the parameters listed in Table 4.1 has been determined by other researchers (Kueper and McWhorter, 1991; Slough et al., 1999) as being a reasonable conceptual representation of a real fracture; therefore, the implementation of other capillary pressure curves was not undertaken.

4.1.4 Boundary Value Problem

The boundary value problem used is demonstrated in Figure 4.1. A 0.6 m column of NAPL is placed on the centre third of the top of a discrete, rough-walled fracture; that is, NAPL extends from $x = 1.25$ m to $x = 2.5$ m. The height of the column of NAPL placed on the fracture in this case corresponds to a NAPL pressure of 9500 Pa. Initial constrained NAPL saturations in each of the grid blocks under the column were obtained by comparing the NAPL pressure at the base of the column with the entry pressure at the top of the fracture. The saturations for the 26 grid blocks under the column are given in Figure 4.2. A hydrostatic water column is defined for the fracture prior to the introduction of NAPL. Subsequent simulations test the sensitivity to differing initial flow conditions and NAPL column heights. The sides of the fracture are considered to be symmetry boundaries with respect to both NAPL and water flow as well as aqueous phase transport.
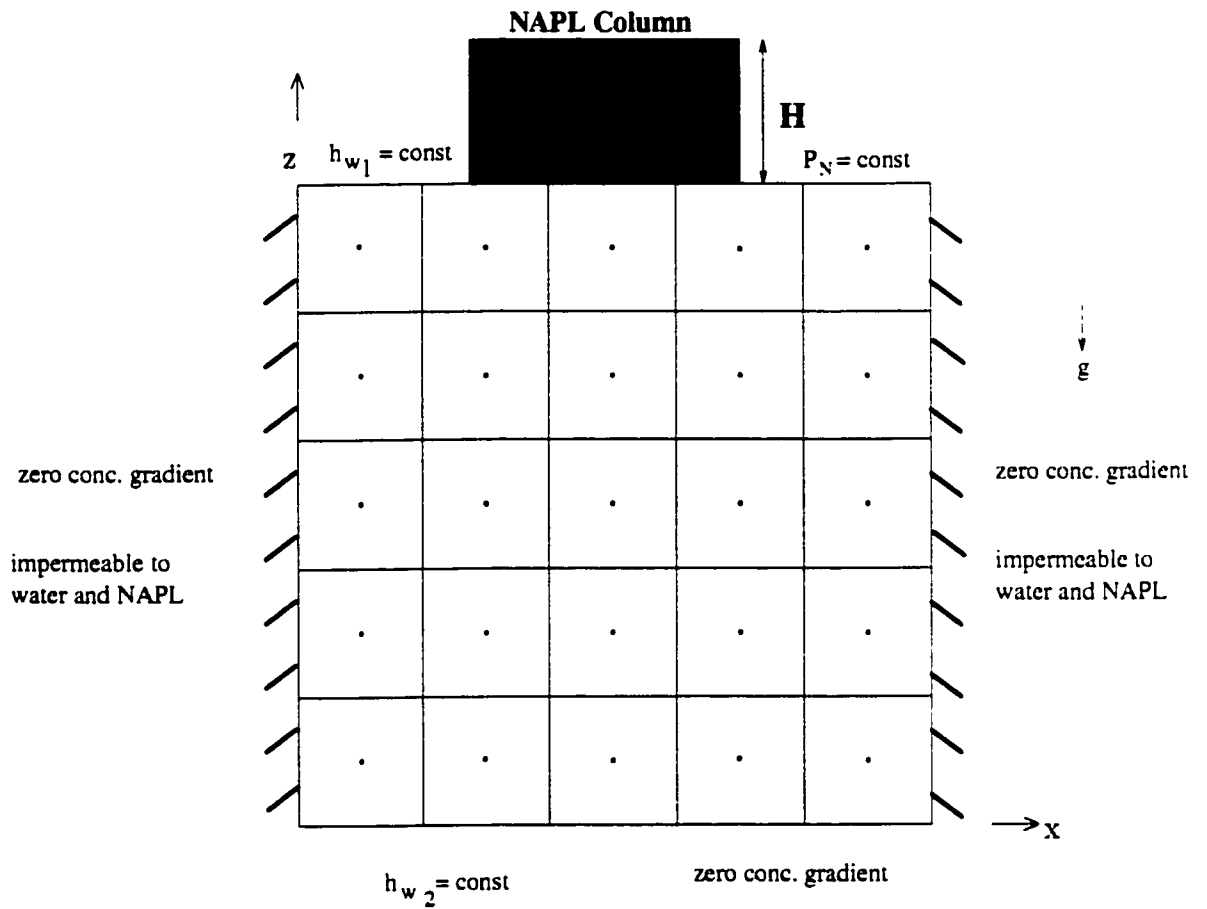
Figure 4.1: Conceptual diagram of boundary value problem used in model simulations. The grid discretization has been simplified for illustrative purposes.
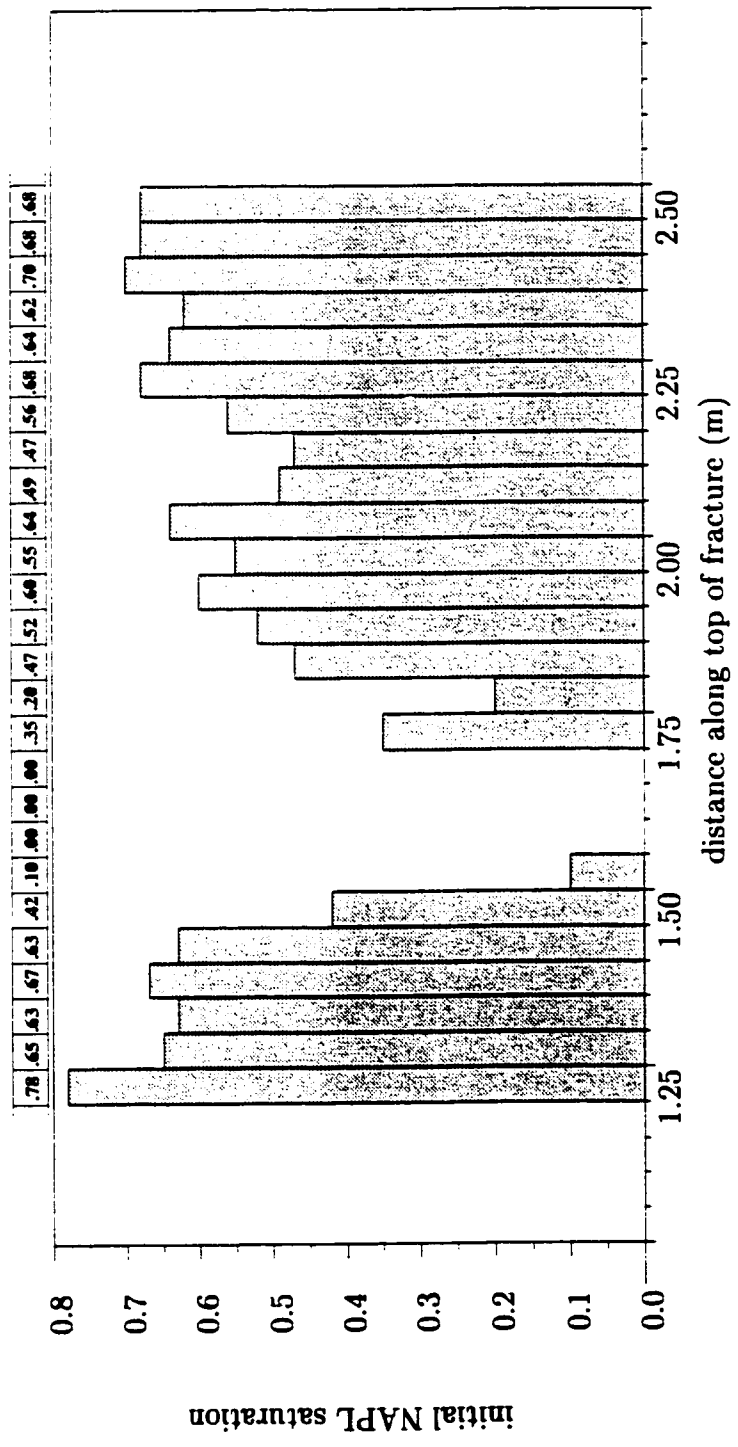
Figure 4.2: Initial NAPL saturations for the base flow simulation. Numbers along the top of the graph are the actual saturation values.

4.1.5 Base Flow Simulation Parameters

Parameters for the base flow simulation were chosen to be representative of plausible conditions in a real fracture embedded in low permeability material. The fracture characterization described above is similar to the characterization used by other researchers (Kueper and McWhorter, 1991; Parker *et al.*, 1994; Banack, 1996; Slough *et al.*, 1999). The parameters chosen to represent the non-aqueous phase liquid (NAPL) are similar to tetrachloroethylene (PCE), a dense chlorinated solvent typically used in drycleaning and other operations. The specific parameters are given in Table 4.2.

4.1.6 General Considerations With Respect to Flow

All simulations were run until the maximum saturation of NAPL at the bottom of the fracture reached 2%. This criteria was arbitrarily chosen in order to compare simulation times for different runs and is the same as the criteria chosen by Kueper and McWhorter (1991). Figure 4.3 shows the general NAPL distribution at several times, ending with the point at which NAPL reaches the bottom of the fracture. As the fracture apertures range over several orders of magnitude, a variable distribution of free-phase NAPL was expected and observed.

Figure 4.4 shows an overlay of NAPL saturation contours on the aperture field at the final time step. This diagram shows that, in general, the NAPL preferentially follows the path with the largest apertures (the lighter areas in Figure 4.4). This phenomenon is consistent with results of a study conducted by Kueper and McWhorter (1991), who offer that "...DNAPL will preferentially migrate through a fracture along the larger aperture pathways." In addition, NAPL is attenuated near areas with small apertures, as high NAPL pressures are required to exceed the entry pressures for these blocks (cf., Equation 2.6). The distribution of NAPL is also strongly influenced by the aperture distribution at the base of the NAPL column, as the centre of the fracture begins with much lower saturations relative to the

Parameter Name	Symbol	Value	Units
number of columns	nx	75	-
number of rows	nz	75	-
number of slices	ny	7	-
ln-mean aperture value	$\overline{Y}$	-8.8	-
geometric-mean aperture value	b	150	μm
ln-aperture variance	σ_Y^2	0.65	-
fracture spacing	f_{sp}	0.985	m
spatial aperture correlation	λ_{sp}	0.5	m
grid discretization	$\Delta x = \Delta z$	0.05	m
fracture porosity	ϕ_f	1.0	-
matrix porosity	ϕ_m	0.2	-
norm for S_w convergence (Newton-Raphson it.)	E_n^{nr}	1.0×10^{-4}	-
norm for P_n convergence (Newton-Raphson it.)	l_1^{nr}	1.0×10^{-4}	-
norm for S_w convergence (coupled iteration)	E_n^{cp}	1.0×10^{-5}	-
norm for P_n convergence (coupled iteration)	l_1^{cp}	1.0×10^{-5}	-
norm for concentration convergence (coupled iteration)	E_n^{con}	1.0×10^{-5}	-
density of water	ρ_w	1000	kg/m^3
density of NAPL	ρ_n	1620	kg/m^3
viscosity of water	μ_w	0.001	Pa · s
viscosity of NAPL	μ_n	0.0018	Pa · s
interfacial tension	σ	0.04	N/m
column height of NAPL	H	0.6	m
wetting phase hydraulic head at top of fracture	h_t	30	m
initial wetting phase gradient down fracture	dh/dz	0	m/m
longitudinal dispersivity	α_L	0.1	m
transverse dispersivity	α_T	0.1	m
retardation factor for the fracture	R_f	1	-
retardation factor for the matrix	R_m	1	-
NAPL solubility limit	s	0.15	kg/m^3
effective diffusion coefficient	D^*	1.0×10^{-8}	m^2/s
time weighting factor for transport	β	1	-

Table 4.2: Parameters for base flow simulation.
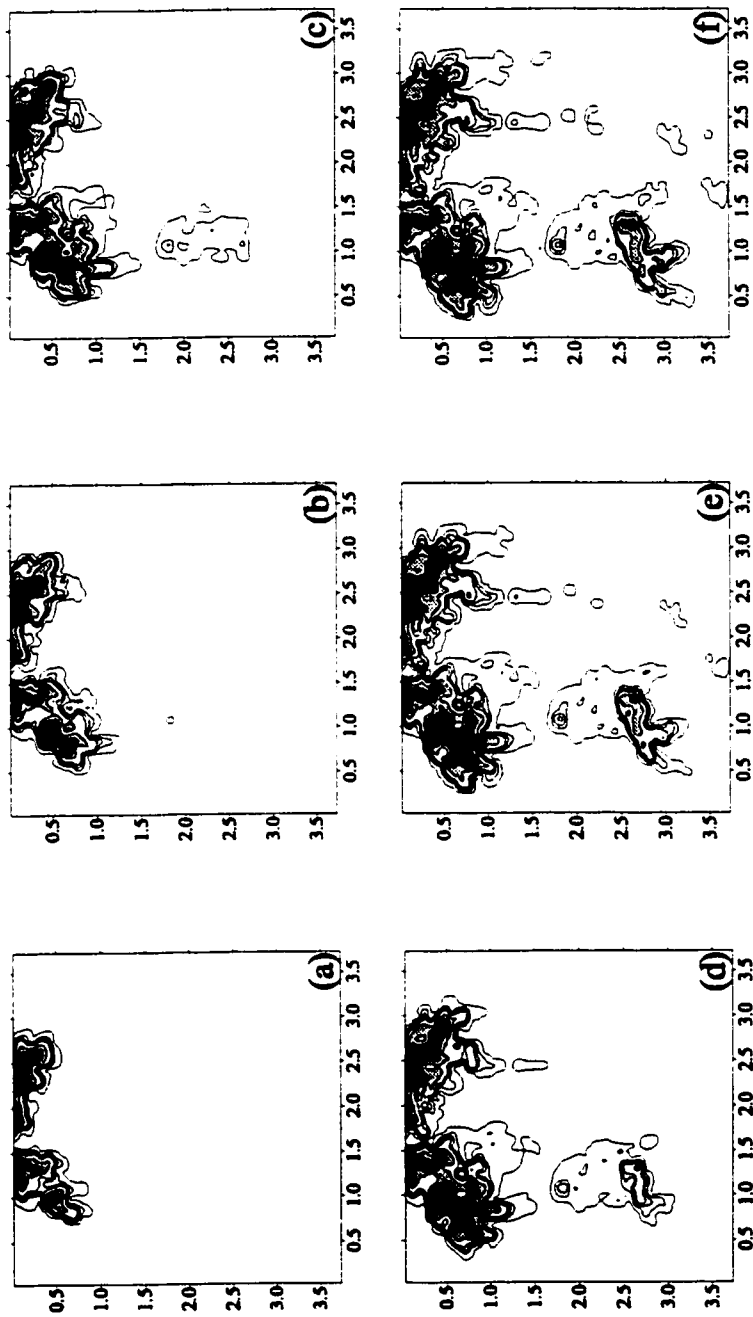
Figure 4.3: NAPL saturations for the base flow simulation with dissolution corresponding to (a) 120 seconds, (b) 240 seconds, (c) 360 seconds, (d) 480 seconds, (e) 600 seconds, and (f) 642 seconds (final time). Contours represent NAPL saturations at 0.5%, 5.5%, 10.5%, 15.5%, 30.5%, 45.5%, 60.5%, and 75.5%. Note that all areas containing NAPL are connected to one another; however, saturations may be below the minimum contour interval, and hence may not appear.
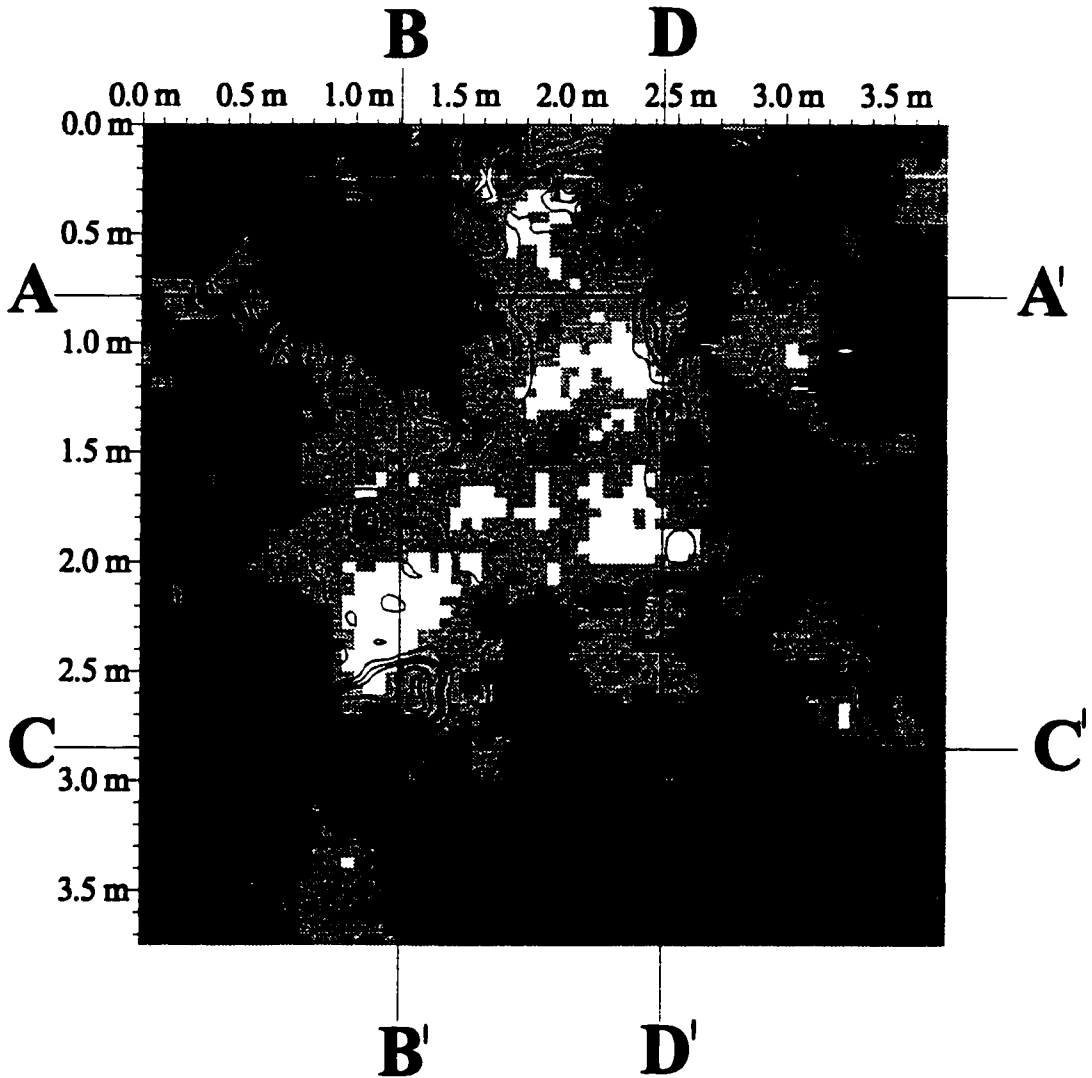
Figure 4.4: The final NAPL distribution for the base flow simulation, overlain on the fracture aperture field. An explanation of contour values is given in Figure 4.3. Profiles A-A', B-B', C-C', and D-D', with Intersections 1-4, are annotated on the figure. Table 4.3 provides locations and aperture sizes for Intersections 1-4.

Intersection #	column #	row #	x coord. (m)	z coord. (m)	b (μm)
1	25	16	1.225	0.775	182
2	49	16	2.425	0.775	216
3	25	57	1.225	2.825	47
4	49	57	2.425	2.825	572

Table 4.3: Intersections as shown on Figure 4.4, with their location and aperture information.

saturations closer to the sides (Figure 4.2).

To examine how the NAPL distribution changes with time, two horizontal and two vertical profiles were arbitrarily taken (Figure 4.4). Figures 4.5 and 4.6 show z and x profiles corresponding to the distributions shown in Figure 4.3.

To elucidate the behaviour of NAPL flow in terms of aperture distribution, graphs comparing NAPL saturation to aperture sizes were prepared. Figure 4.7 shows aperture overlays for profiles A-A' and B-B'. From these graphs, it is clear that saturations correspond, in a general sense, to aperture sizes, such that larger apertures generally have higher saturations. It also appears that NAPL accumulates above areas with smaller apertures, as a higher entry pressure is required for the NAPL to enter into these areas. In the B-B' profile in Figure 4.7, NAPL has passed through the higher aperture blocks (at approximately 2.1 m) and then has built up above the adjacent, smaller, aperture blocks. It is important to note that these profiles are one-dimensional representations of a two-dimensional simulation, and as such these observations may be oversimplified. NAPL flow is, however, primarily vertically downwards at this point.

4.1.7 General Considerations With Respect to Transport

Transport results for the base flow simulation were also examined. The measures chosen for this analysis were the mass flux behaviour from the fracture to the porous matrix, the total mass diffused into the matrix, and an examination of spatial concentration profiles, both in the fracture and into the matrix, and temporal curves for
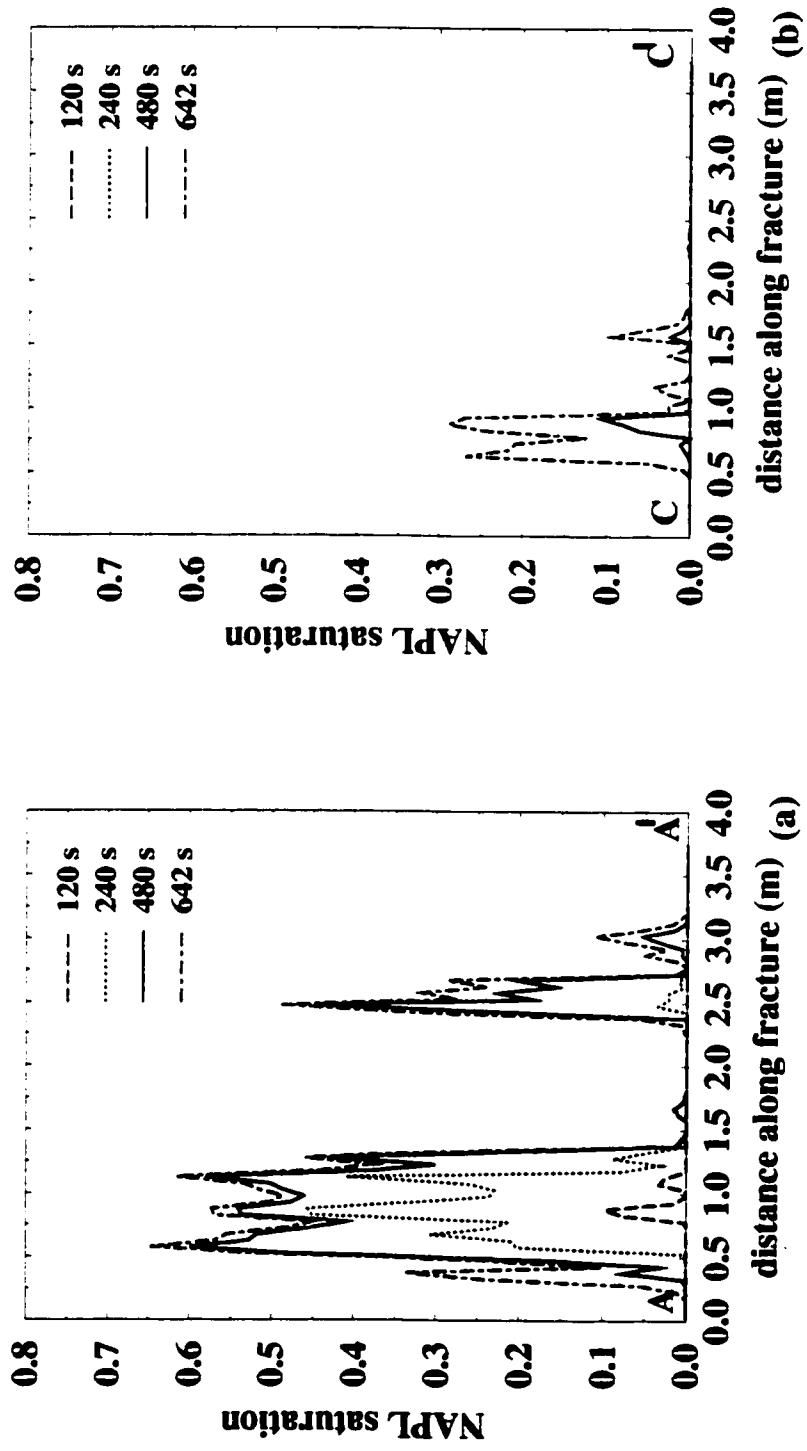
Figure 4.5: Horizontal profiles along A-A' and C-C' through time. The times are given in the figure legends.
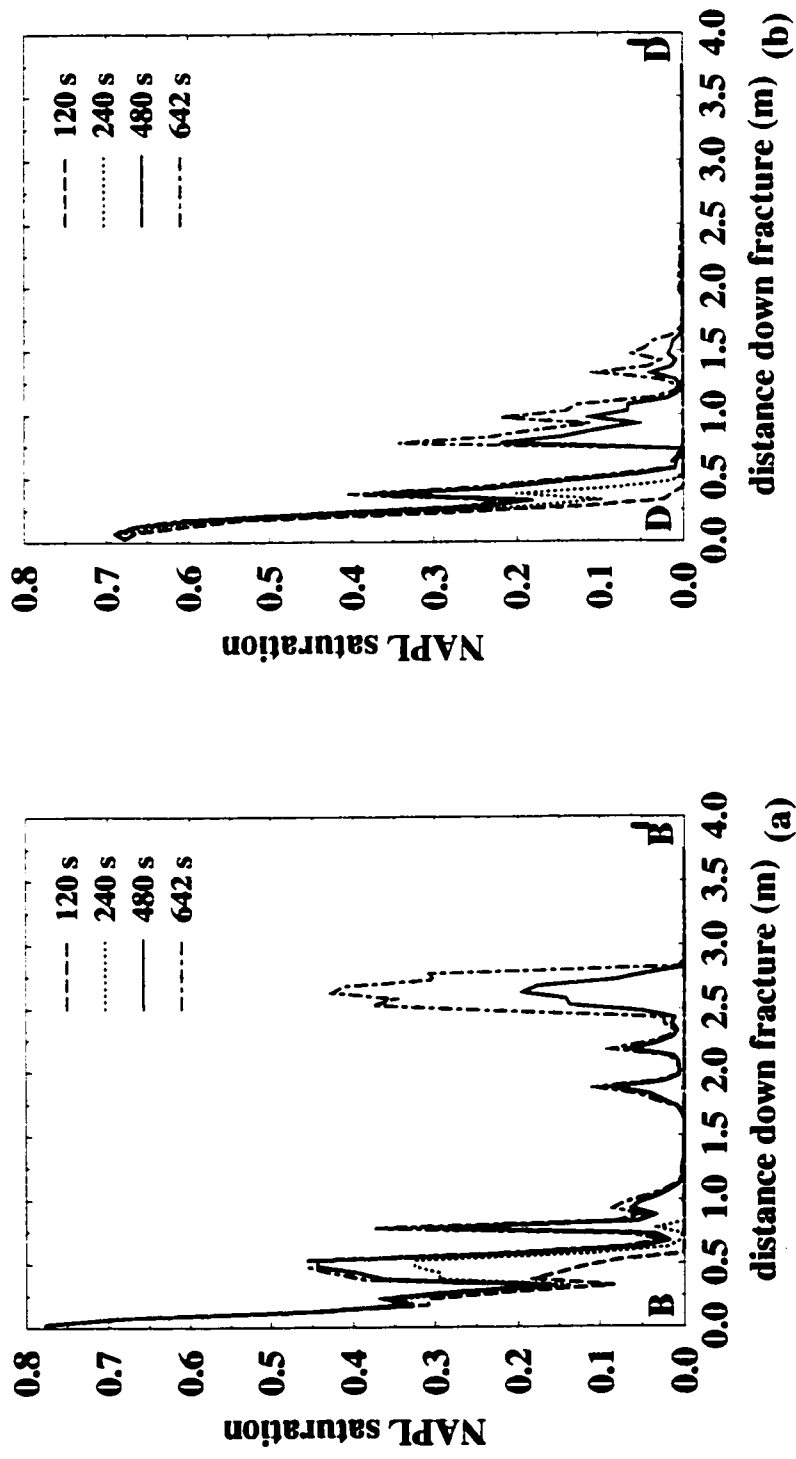
Figure 4.6: Vertical profiles along B-B' and D-D' through time. The times are given in the figure legends.
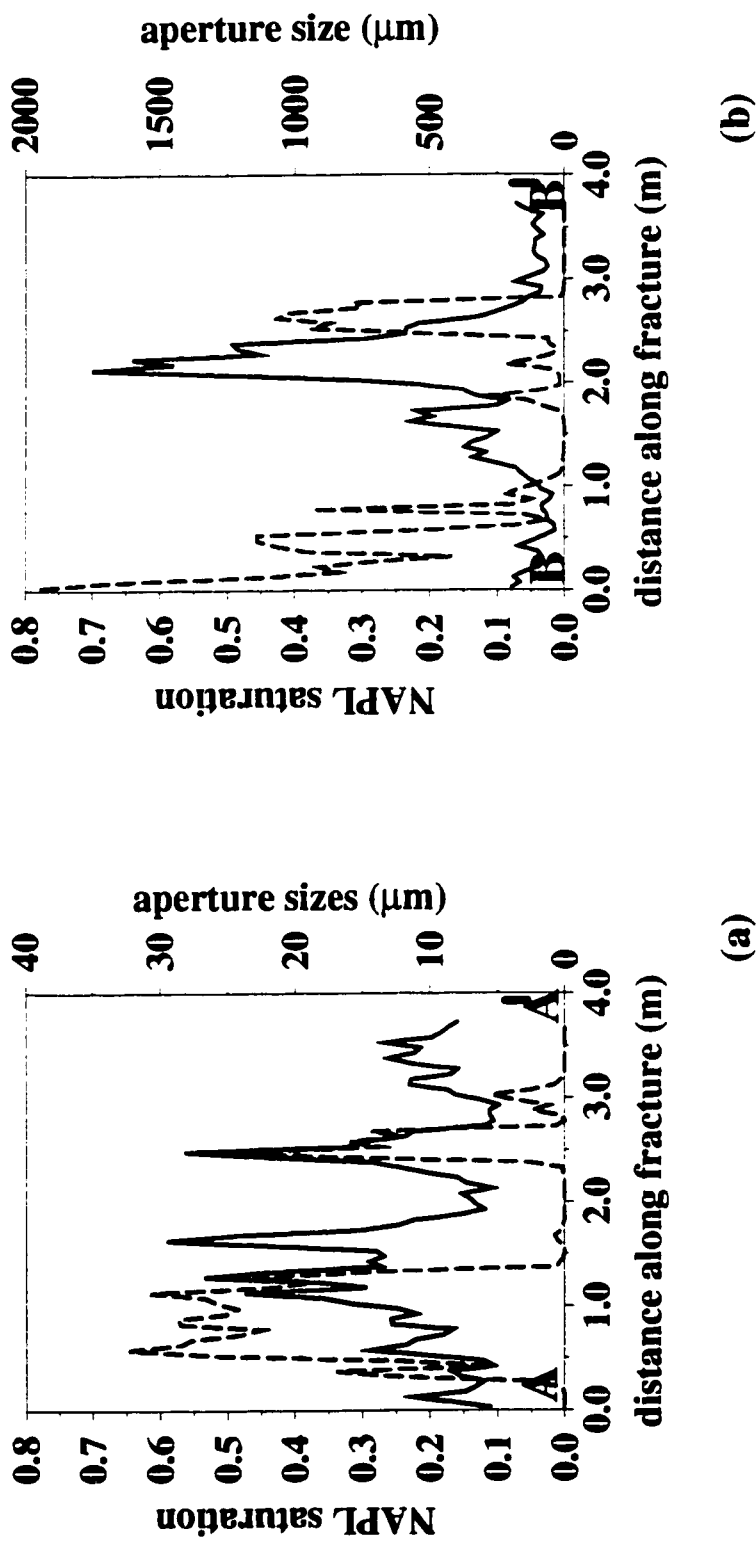
Figure 4.7: NAPL saturation profiles (dashed lines) along A-A′ and B-B′, together with aperture distributions (solid lines) for the final saturation distribution. Note that profile A-A′ has smaller apertures than profile B-B′.

arbitrarily selected fracture blocks.

Mass Flux Behaviour

The definition of mass flux, in general, includes the concentration in the block as well as the diffusion coefficient (Equation 2.28). The concentration in the matrix immediately adjacent to the fracture also has a profound effect on the strength of the mass flux from the fracture into the matrix. The maximum mass flux was seen at the leading edge of NAPL migration, where the concentration gradient was greatest. The strength of the mass flux from the fracture to the matrix at a given block over time decreased as more mass was introduced into the matrix at that block. The mass flux at a given block was typically on the order of 10^{-10} kg/m^{2}s for the base case, with the flux near the source decreasing from roughly 4×10^{-10} kg/m^{2}s initially to 2×10^{-10} kg/m^{2}s at the end of the simulation.

Total Mass Diffused

The total mass diffused into the matrix was deemed an important measure of the transport characteristics and of the coupling between flow and transport. This model output also has implications for remedial alternatives at real fractured sites, as the amount of mass that diffuses into the matrix would conceivably diffuse out if the fracture were flushed with clean water. Figure 4.8 shows the amount of mass diffused into the matrix as a function of time, normalized to the total amount of mass in the fracture.

From this figure, it can be seen that a significant amount of mass can be stored in the porous matrix, relative to the total mass in the fracture. At the final time of 642 seconds, more than 15% of the total mass of NAPL in the fracture at that point in time has diffused. This is even more impacting considering that the source of NAPL in the fracture is continuous; this means that a proportionally greater mass of NAPL is diffusing as more mass is introduced into the fracture.
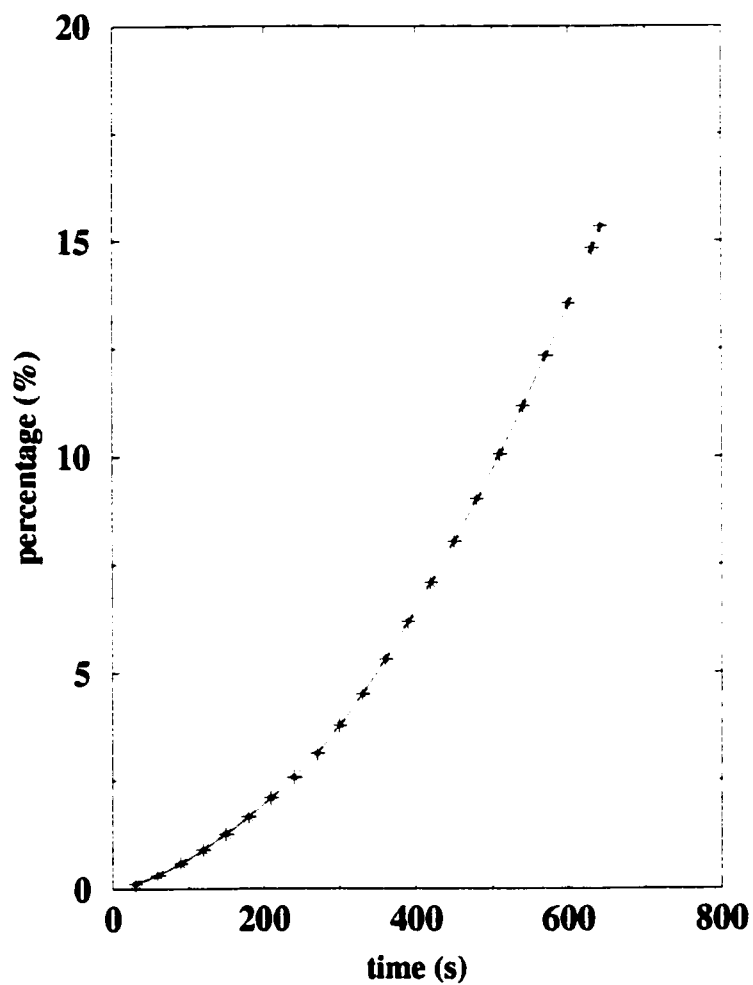
Figure 4.8: Total mass diffused into the porous matrix for the base case, expressed as a percentage of the total amount of mass in the fracture.

Concentration Profiles

In addition to examining the free-phase NAPL migration in the fracture, dissolved phase transport in the fracture and in the porous matrix is of interest. In order to examine this, spatial and temporal concentration profiles were taken in the fracture and the surrounding porous matrix.

Spatial profiles

As outlined in Chapter 3, concentrations in the fracture were constrained to their solubility limit wherever free-phase NAPL exceeded a threshold saturation. Because of this constraint, concentrations in the fracture tend to closely mimic the migration pattern of the NAPL. Very little dissolved phase migration is visible in the fracture due to diffusion. Therefore, comparative spatial profiles in the fracture were not taken.

The profiles from the fracture into the porous matrix are of greater interest, as they show the distribution of mass in the matrix. Figure 4.9 shows profiles from Intersection 1 (Figure 4.4) into the matrix for various times. The concentrations are plotted relative to the solubility limit. From Figure 4.9, it can be seen that the strength of the diffusive process decreases with time, as the concentrations in the matrix blocks increase at a slower rate as time progresses. This is consistent with the observation given in Section 4.1.7, where the mass flux decreases with time at any position in the domain. Parker et al. (1997) also observed this phenomenon, where the rate at which concentrations increase in the matrix declines with time as the matrix storage capacity diminishes.

Figure 4.10 shows image maps of the concentrations in the fracture and in the first two matrix slices adjacent to the fracture for the final distribution. This figure demonstrates that concentration distributions in the matrix are dependent on both the distribution as well as the residence time of NAPL in the fracture. Areas closer to the source, where NAPL has resided longer, have higher concentrations in the matrix, whereas areas closer to the bottom of the fracture have lower concentrations.

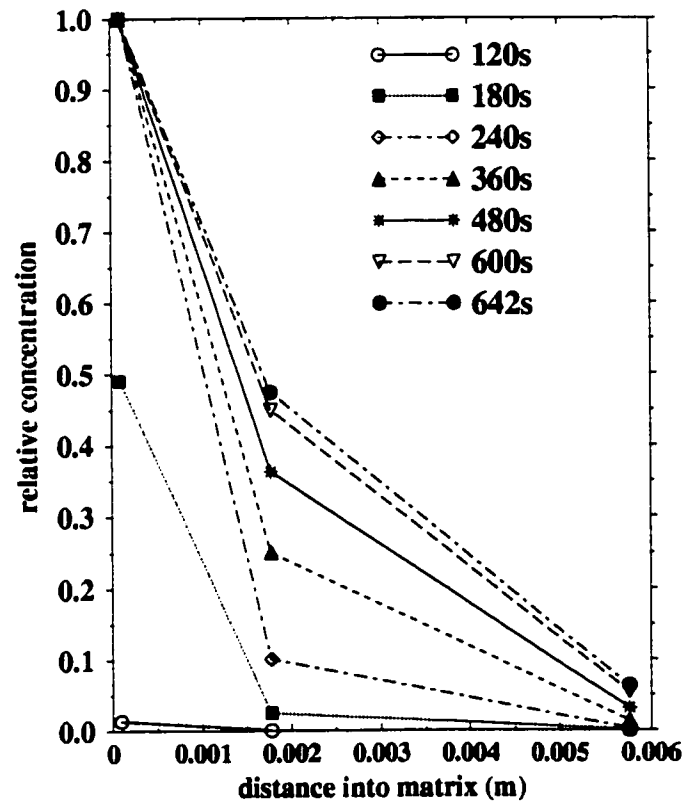Figure 4.9: Profiles from Intersection 1 in the fracture into the first two matrix slices at various times.

Figure 4.10: Concentration distributions in (a) the fracture, (b) the first matrix slice, and (c) the second matrix slice for the base case at the final saturation distribution. Darker areas show higher relative concentrations, to a maximum value of 1. The horizontal and vertical scales are as shown in Figure 4.4.

Temporal profiles

Temporal profiles were taken at Intersections 1-4 in the fracture to examine dissolved phase behaviour. Figure 4.11 shows the results for profiles at Intersections 1-4. Each profile shows a characteristically different shape, all ending with the relative concentrations increasing rapidly to 1.0 as NAPL reaches the required threshold saturation to constrain the grid block concentration.

NAPL reaches Intersection 1 before any of the other Intersections, and hence there is little time for much of the dissolved phase to flow. Recall that the initial water column flow field is hydrostatic, and all water flow is induced by the free NAPL flow displacing the water. At Intersection 2, there is more time between the beginning of the simulation (i.e., the commencement of dissolution) and when free-phase NAPL reaches it. Hence, one would expect to see a more gradual increase in concentration at Intersection 2 than at Intersection 1.

Intersections 3 and 4 are much further down the fracture than Intersections 1 and 2; therefore, one might expect somewhat different behaviour. The profile for Intersection 3 on Figure 4.11 shows a more gradual increase to a relative concentration of 1 than do the other profiles. It was unclear, however, whether the difference in the behaviour of concentration increase is due to its position in the fracture or to some other factor. Therefore, temporal concentration profiles for the blocks immediately above Intersection 3 were taken to test this hypothesis. The resultant profiles for two blocks immediately above Intersection 3 are shown in Figure 4.12.

Figure 4.12 shows that aperture size can be directly correlated to the rate of increase in concentration. This correlation is, in turn, related to free-phase NAPL flow, where the grid block with the smaller aperture takes much longer to reach the required threshold NAPL saturation. In fact, it takes about 200 seconds longer for NAPL to fill the grid block at Intersection 3 with 0.01% saturation of NAPL than for the block directly above it. That block, having an aperture of roughly twice that of Intersection 3, only takes about 50 seconds longer than the block above it to reach the same threshold saturation. This phenomenon occurs because smaller aperture
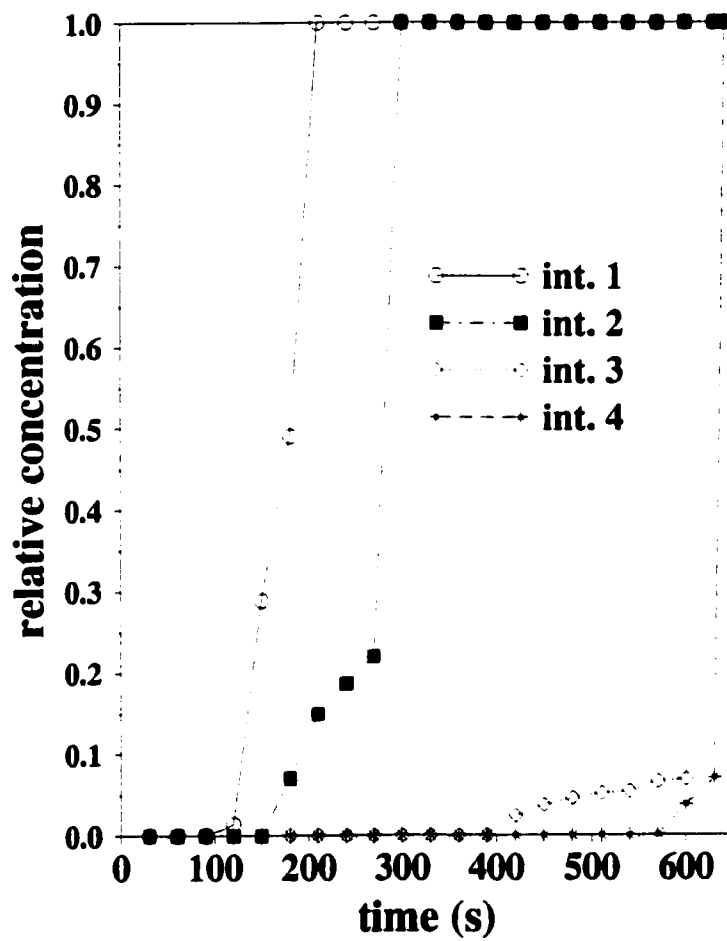
Figure 4.11: Concentration breakthrough curves in the fracture with respect to time for Intersections 1 to 4.
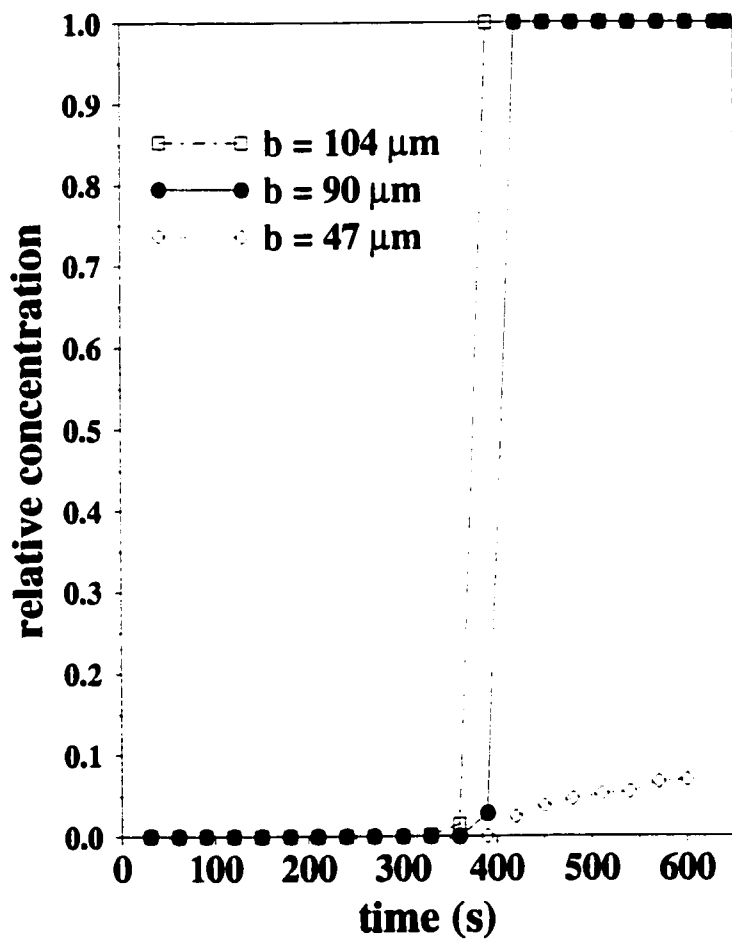
Figure 4.12: Concentration breakthrough curves in the fracture for Intersection 3 (b=47 μm), and the two blocks immediately above it (b=90 μm and b=104 μm, respectively).

blocks have a higher entry pressure, and larger volumes of NAPL are required to accumulate above the block before entry can occur.

4.2 Preliminary Simulations

A number of different simulations were conducted to examine the behaviour of a system subject to varying conditions. The following four sections will outline these simulations.

4.2.1 Comparison to Case Without Dissolution

In order to compare the effect that dissolution has on the simulation, a similar simulation with a NAPL solubility of 0 kg/m^3 was performed. The greatest difference in NAPL saturation between the simulations with and without dissolution was at lower saturations, where the saturations were just above the threshold saturation value.

The total travel time, defined as the time that the NAPL takes to get to a maximum of 2% saturation at the bottom of the fracture, increases only 2 seconds from the simulation without dissolution to the base simulation with dissolution. It is clear that, for the base case, the coupling between flow and transport, or the effect that dissolution has on the flow solution, is minimal. Other cases that increase the strength of the coupling will be examined in subsequent sections.

4.2.2 Homogeneous Fracture

A simulation was conducted where every fracture aperture was assigned $\overline{Y} = -8.8$; that is, the aperture variance was specified as 0. All of the other parameters are as given in Tables 4.1 and 4.2.

The total real simulation time, or the time that NAPL took to reach the bottom of the fracture, was 730 seconds. This is approximately 88 seconds, or 1.5 minutes, longer than the base flow simulation. This makes intuitive sense as the homogeneous fracture simulation does not have correlated flow paths of larger apertures in which

to flow (as the base case simulation does). Subsequently, NAPL in the homogeneous fracture does not have the opportunity to bypass areas with smaller apertures.

4.2.3 Low Permeability Lens

In order to examine the behaviour around low permeability (or small aperture) grid blocks, a simulation was run where most of the aperture blocks were assigned the same (mean) aperture. Within this uniform aperture field, two layers of grid blocks, oriented horizontally across the entire fracture in its approximate centre, were assigned apertures one order of magnitude lower than the mean.

The simulation demonstrated that low permeability/smaller aperture blocks are a significant impediment to free-phase NAPL flow. Upon reaching the low permeability rows, NAPL began to pool, and subsequently spread outward towards the edges of the fracture with time. Breakthrough beyond the low permeability layers only occurred in the area directly below the source, where the maximum amount of NAPL had pooled, and the saturations below the low permeability rows were very small. This supports what is seen in the base case simulation, where the highest NAPL saturations (the red areas in Figure 4.13(a)) are confined to the region near the top of the fracture, as the NAPL first encounters grid blocks with smaller apertures.

4.2.4 Aperture Binning

A simulation was conducted where the apertures were placed into statistically related "bins" or groupings, rather than being treated uniquely. The objective of this substudy was to determine if an alternative to Leverett-J capillary pressure scaling could be developed that would be more efficient with respect to CPU time, while still maintaining an acceptable solution.

Initially, one standard deviation was considered to be one bin. That is, upper and lower bounds for 4 standard deviations larger than the mean aperture and for 4 standard deviations smaller than the mean aperture were determined. All apertures occurring in one bin were then assigned the (harmonic) mean aperture of that bin.
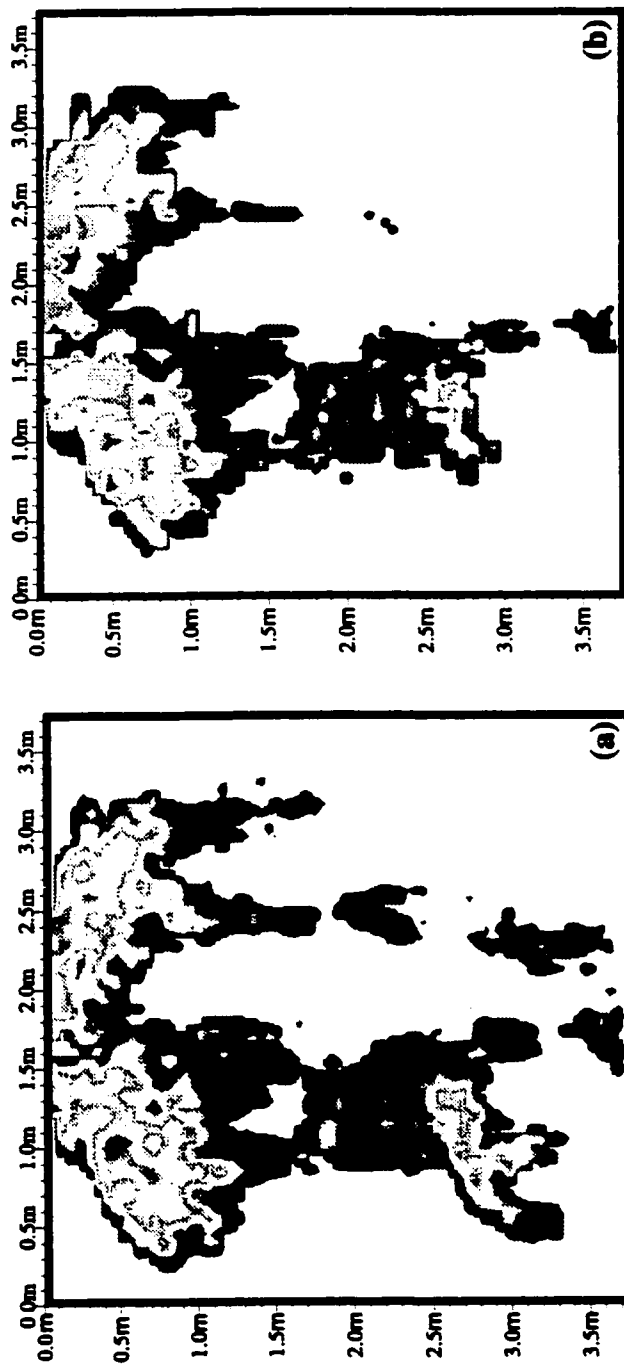
Figure 4.13: Final NAPL distributions for: (a) Leverett J-scaled apertures versus (b) binned apertures. Saturations range from 2% (dark blue) to 78% (red).

This effectively reduced the number of unique apertures from up to 5625 (75 × 75 blocks) to only 8. While it is conceded that placing all apertures into only 8 bins is a very coarse approximation of real aperture values, it was sufficient to fulfill the objective of the substudy. Simulations with a larger number of bins were therefore not performed.

Using aperture binning, a savings in CPU time on the order of 10% was realized, with the real simulation time decreasing by roughly 7%, to 601 seconds from 642 seconds for the base flow simulation. Also, it can be seen from Figure 4.13 that the NAPL distributions are somewhat different. This is particularly evident on in the lower right hand quadrant of the binned simulation, where NAPL has been attenuated much more so than in the base flow simulation. It does not appear that the base flow simulation can be effectively pared down to 8 unique apertures and still maintain the same properties. It also does not appear that there is a significant CPU time savings in doing so.

4.3   Numerical Instability in FaTMatD

Accepted accuracy criteria (Fetter, 1993) were satisfied at all times for both flow and transport for all simulations. However, when the analysis of the simulations began, it became apparent that the coupling (dissolution) between flow and transport required more stringent criteria, translating to a smaller time step size. This was deduced from Figure 4.14, a plot showing total mass diffused versus time for the base flow simulation as well as a simulation done with higher solubility (*increased-s^2*). It can be seen that the instability increases as dissolution increases. Because of this, all of the simulations were re-run with much smaller time steps, typically at 25% to 50% of what had been used previously. Simulations that affected the matrix diffusion component of transport, such as solubility and matrix porosity, generally required smaller time steps than did runs that provided a greater sensitivity to NAPL flow. The time step size was not precalculated, but instead each run was checked with respect to total mass diffused to determine its stability. Adaptive time stepping was
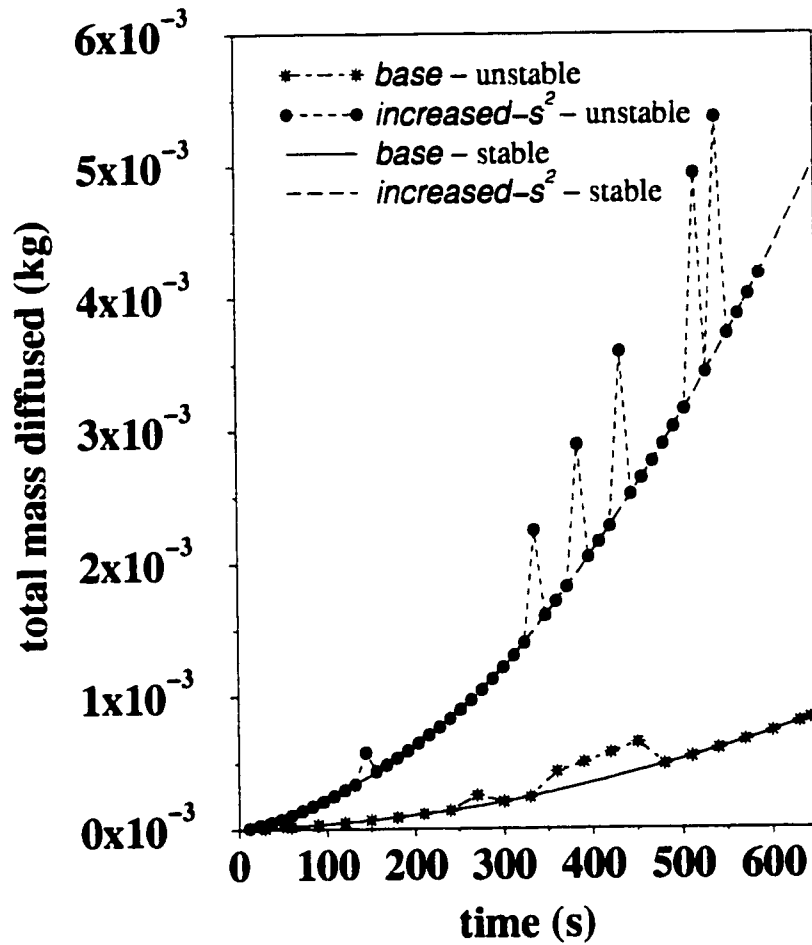
Figure 4.14: Total mass diffused into the matrix versus time demonstrating numerical instability in FaTMatD. The peaks in the unstable cases represent oscillations in the solution.

implemented into the model; however, it was not utilized due to the difficulty in determining appropriate accuracy criteria *a priori*.

Sensitivity Analysis

A sensitivity analysis was performed in order to test system behaviour against changes in input parameters. In most cases, a triangular distribution was assumed, with reasonable low, mean, and high values chosen either from the literature or arbitrarily, as appropriate.

Table 4.4 provides a summary of the simulations performed. In every case, only one parameter was perturbed at a time, with the remainder of the parameters assigned as they were in the base case (Table 4.2). Four different categories of sensitivity have been defined. These are given as follows:

1. properties of the contaminant:

   - NAPL density

   - dynamic viscosity

   - diffusion coefficient

   - solubility

2. properties of the aperture field:

   - mean

   - variance

   - correlation length

3. properties of the porous matrix:

   - fracture spacing

   - matrix porosity

Simulation ID	Changed Parameter and Value	Units	Total Travel Time (s)
base	-	-	642
increased-Y	$Y = -7.8$	-	70
decreased-Y	$Y = -9.8$	-	11000
increased-σ_Y^2	$\sigma_Y^2 = 0.80$	-	636
decreased-σ_Y^2	$\sigma_Y^2 = 0.10$	-	790
decreased-f_{sp}	$f_{sp} = 0.0058$	m	642
increased-λ_{sp}	$\lambda_{sp} = 1.0$	m	490
decreased-λ_{sp}	$\lambda_{sp} = 0.25$	m	820
increased-s^1	$s = 0.30$	kg/m^3	644
increased-s^2	$s = 0.90$	kg/m^3	651
increased-ρ_n	$\rho_n = 1820$	kg/m^3	490
decreased-ρ_n	$\rho_n = 1200$	kg/m^3	1700
increased-D	$D^* = 1.0 \times 10^{-7}$	m^2/s	647
decreased-D	$D^* = 1.0 \times 10^{-10}$	m^2/s	640
increased-ϕ_m^1	$\phi_m = 0.4$	-	643
increased-ϕ_m^2	$\phi_m = 0.8$	-	645
decreased-ϕ_m	$\phi_m = 0.05$	-	641
increased-μ_n	$\mu_n = 0.0024$	Pa · s	870
decreased-μ_n	$\mu_n = 0.0010$	Pa · s	370
increased-H	$H = 0.8$	m	570
decreased-H	$H = 0.4$	m	800
increased-δ	$dh/dl = 0.1$	-	460
decreased-δ	$dh/dl = -0.1$	-	1200

Table 4.4: Summary of parameters tested in sensitivity analysis.

4. properties relating to the boundary value problem definition:

- NAPL column height
- gradient of water flow field

4.4 Effect of Parameter Sensitivity on NAPL Flow

The first arena of interest is the extent to which parameter perturbations affect overall NAPL flow velocity and NAPL distribution in the fracture. A similar analysis to that performed for the base case was carried out, with an examination of travel time, intermediate and final NAPL distributions, and profiles across the fracture.

4.4.1 Total NAPL Travel Time

Figure 4.15 shows a graphical summary of the sensitivity that each parameter had on the total time taken for 2% saturation of NAPL to reach the base of the fracture. The actual travel times are given in Table 4.4.

From Figure 4.15, it can been seen that the simulations have varying degrees of sensitivity for different parameters. NAPL density, NAPL viscosity, mean aperture, aperture variance, correlation length, NAPL column height, and initial water column flow field definition appear to affect the NAPL flow velocity to the greatest degree. Other parameters have a much smaller effect.

Total NAPL travel time - Contaminant properties

NAPL density provided the greatest simulation sensitivity for this category. The reason for this is partially derived from the fact that NAPL column height is kept constant at 0.6 m. For a NAPL with a lower density, this means that a smaller pressure is exerted at the top of the fracture (see Equations 2.4 and 2.5), because the capillary pressure P_c is directly proportional to the NAPL density. A smaller pressure corresponds, in turn, to lower NAPL saturations constrained at the top of
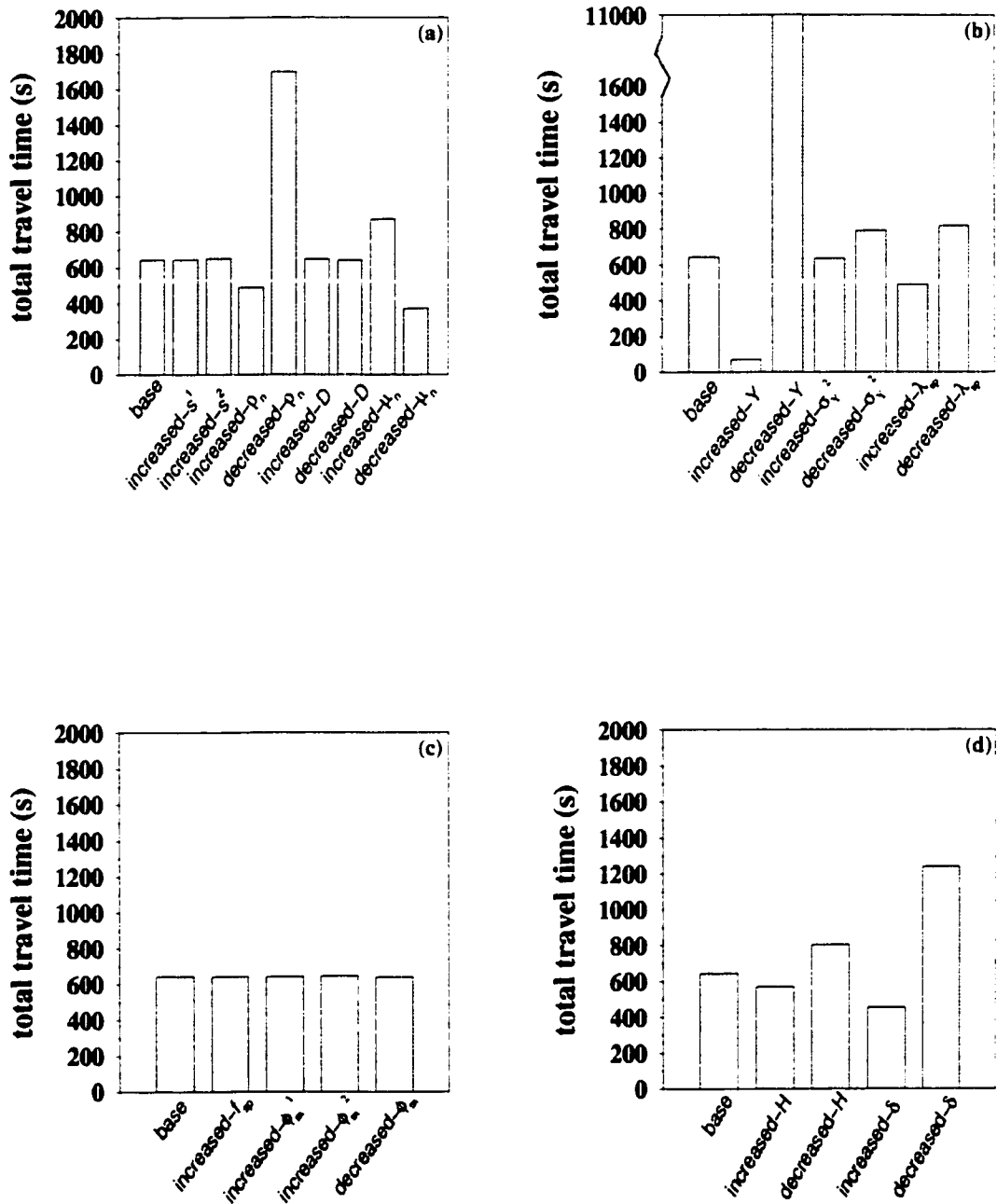
Figure 4.15: Bar charts showing sensitivity to total NAPL travel time for (a) contaminant properties, (b) aperture field properties, (c) matrix properties, and (d) boundary condition properties. The charts are plotted on the same vertical scale. An explanation of the parameter changes is given in Table 4.4.

Simulation ID	$\overline{Y}$	$\bar{b}$ (μm)	σ_Y^2	λ_{sp} (m)	min. b (μm)	max. b (μm)
base	-8.8	150	0.65	0.5	15	2306
increased-Y	-7.8	409	0.65	0.5	41	6268
decreased-Y	-9.8	55	0.65	0.5	5	848
increased-σ_Y^2	-8.8	154	0.80	0.5	12	3258
decreased-σ_Y^2	-8.9	134	0.10	0.5	52	408
increased-λ_{sp}	-8.7	168	0.57	1.0	24	1604
decreased-λ_{sp}	-8.9	134	0.64	0.25	9	2515

Table 4.5: Parameters for simulations varying in aperture field properties.

the fracture. In addition, for the same aperture fields, a decrease NAPL density requires an increase in accumulated NAPL mass at any point in the fracture to allow migration; the converse is also true. For these reasons, the NAPL travel time increases or decreases inversely to the change in NAPL density.

NAPL viscosity also affects the total travel time for the simulation. From Equation 2.20, it can be easily seen that Darcy velocity and NAPL viscosity are inversely related to one another. Therefore, as viscosity increases, so must total NAPL travel time, as the Darcy velocity, and hence average linear groundwater velocity, must decrease accordingly.

Total NAPL travel time - Aperture field properties

Table 4.5 shows mean, minimum, and maximum aperture values for perturbations in aperture field properties. The small variations in $\overline{Y}$ for perturbations in aperture variance and correlation lengths are an artifact of the field generation algorithm and could not be avoided.

More than any other parameter, the mean aperture value caused the greatest change in total NAPL travel time. There are a number of reasons as to why this is the case. The geometric-mean aperture increases by approximately 2.5 times from the base case to case *increased-Y*, and decreases by approximately 0.5 times from the base case to case *decreased-Y*. From Equation 2.1, this corresponds to an increase

and decrease in permeability of roughly an order of magnitude in each direction. As flow rate is directly proportional to permeability, and travel time is inversely proportional to flow rate, a dramatic decrease in travel time for an increase in mean is observed; a dramatic increase in travel time for a decrease in mean is correspondingly observed. The other factor leading to the differences in travel time comes from the apparent relative change in geometric aperture variance, even though the ln-variance remains constant. It can be seen from Table 4.5 that in addition to the means changing, there are corresponding changes in the minimum and maximum aperture values. Therefore, changing the mean also tends to homogenize the smaller mean aperture field somewhat, while making the larger mean aperture field simulation more heterogeneous. The changes in total travel time for these simulations are consistent with observations made in the homogeneous fracture case, where travel time increased in the case where the fracture was more homogeneous. This analysis is also consistent with the increases and decreases seen in simulations $increased\text{-}\sigma_Y^2$ and $decreased\text{-}\sigma_Y^2$, where travel time increases when aperture variance is decreased. The aperture fields for these two simulations are shown in Figure 4.16. This analysis holds in cases where the correlation lengths, or the degree to which an aperture is statistically similar to other apertures around it, does not vary.

Correlation lengths also appear to affect the total travel time for the simulation. The aperture fields corresponding to perturbations in correlation lengths are shown in Figure 4.17. Large correlation lengths increase the statistical probability that one fracture aperture is similar to other fracture apertures around it. This acts to effectively increase the overall permeability of the fracture, in the sense that there are more and/or longer interconnected paths of higher permeability (larger apertures). For this reason, the travel time decreases in simulation $increased\text{-}\lambda_{sp}$. Similarly, when the correlation length is reduced, the fracture effectively has a lower permeability, where the incidence of interconnected higher permeability flow paths is decreased. Therefore, total travel time increases. Pruess and Tsang (1990) also found that relative permeabilities depend sensitively on the spatial correlation scale of the aperture

(a)   (b)   (c)
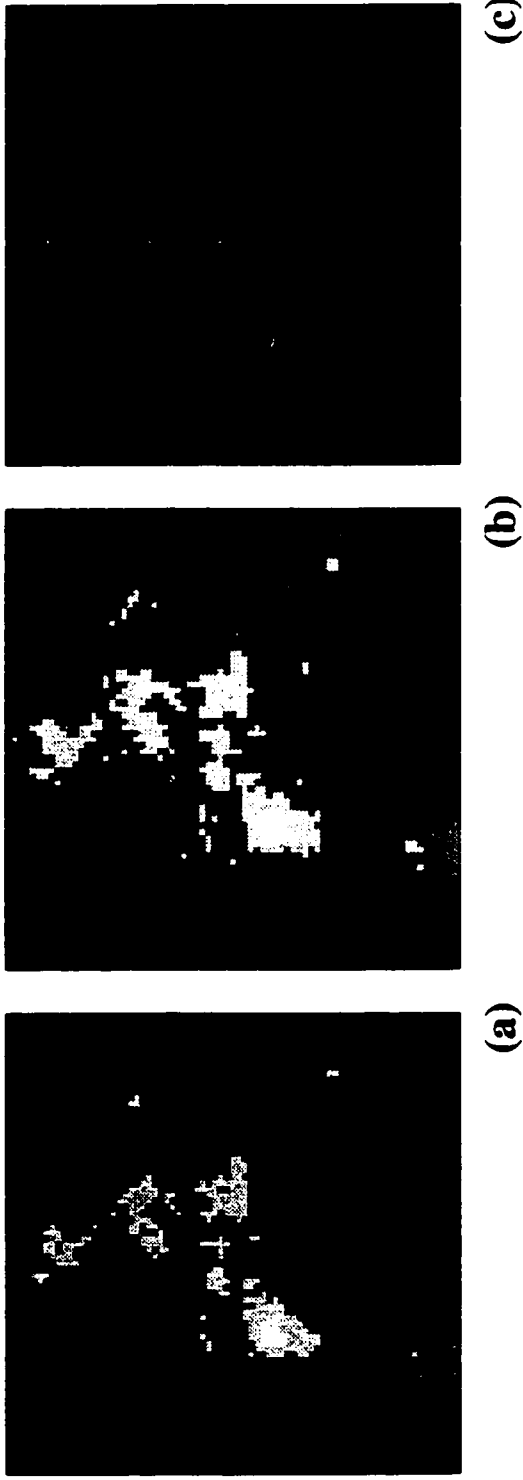
Figure 4.16: Aperture fields for (a) base case, (b) *increased-σ_Y^2*, and (c) *decreased-σ_Y^2*. All of the fields are shown for the same aperture range, with darker areas indicating smaller apertures. The horizontal and vertical scales are as shown in Figure 4.4. Note that the same random number (seed) was used to generate these fields; therefore, they share the same overall structure, with σ_Y^2 scaled.

Figure 4.17: Aperture fields for (a) base case; (b) *increased-λ_{sp}*, and (c) *decreased-λ_{sp}*. All of the fields are shown for the same aperture range, with darker areas indicating smaller apertures. The horizontal and vertical scales are as shown in Figure 4.4.

distribution.

Total NAPL travel time - Boundary condition definition

The last category that appears to significantly affect the NAPL travel time deals with how the boundary conditions are assigned. When the NAPL column height is reduced, the pressure exerted on the top of the fracture is also correspondingly lowered (Equation 2.5). Therefore, the constrained NAPL saturations at the top of the fracture are also reduced (just as they were for the case where NAPL density was made smaller). For this reason, an increase in NAPL travel time is observed. Conversely, when the NAPL column height is increased, the pressure is also increased, and the saturations at the top increase. This leads to a decrease in NAPL travel time.

The effect of the initial water flow field in the fracture on NAPL flow was also considered to be of importance. The rate of flow of NAPL increased when water flowed down the fracture with a gradient of 0.1 (simulation *increased-δ*); the total NAPL travel time decreased accordingly. Correspondingly, the upward flow of water attenuated the flow of NAPL somewhat, causing the NAPL to take longer to traverse the fracture. This is similar to observations made by Kueper and McWhorter (1991); in fact, they found that if they applied a high enough gradient, they could completely halt the downward migration of NAPL.

4.4.2 Intermediate and Final NAPL Distributions

Total travel times provide some indication of the sensitivity of results to input parameters; however, the distribution of NAPL in the fracture was also considered to be an important sensitivity measure. To this end, the sensitivity parameters were analyzed in terms of both intermediate (same time) and final (different time) distributions.

NAPL distributions - Contaminant properties

Figure 4.18 shows intermediate and final NAPL distributions in the fracture for the base case, the case where NAPL density was increased, and where NAPL density
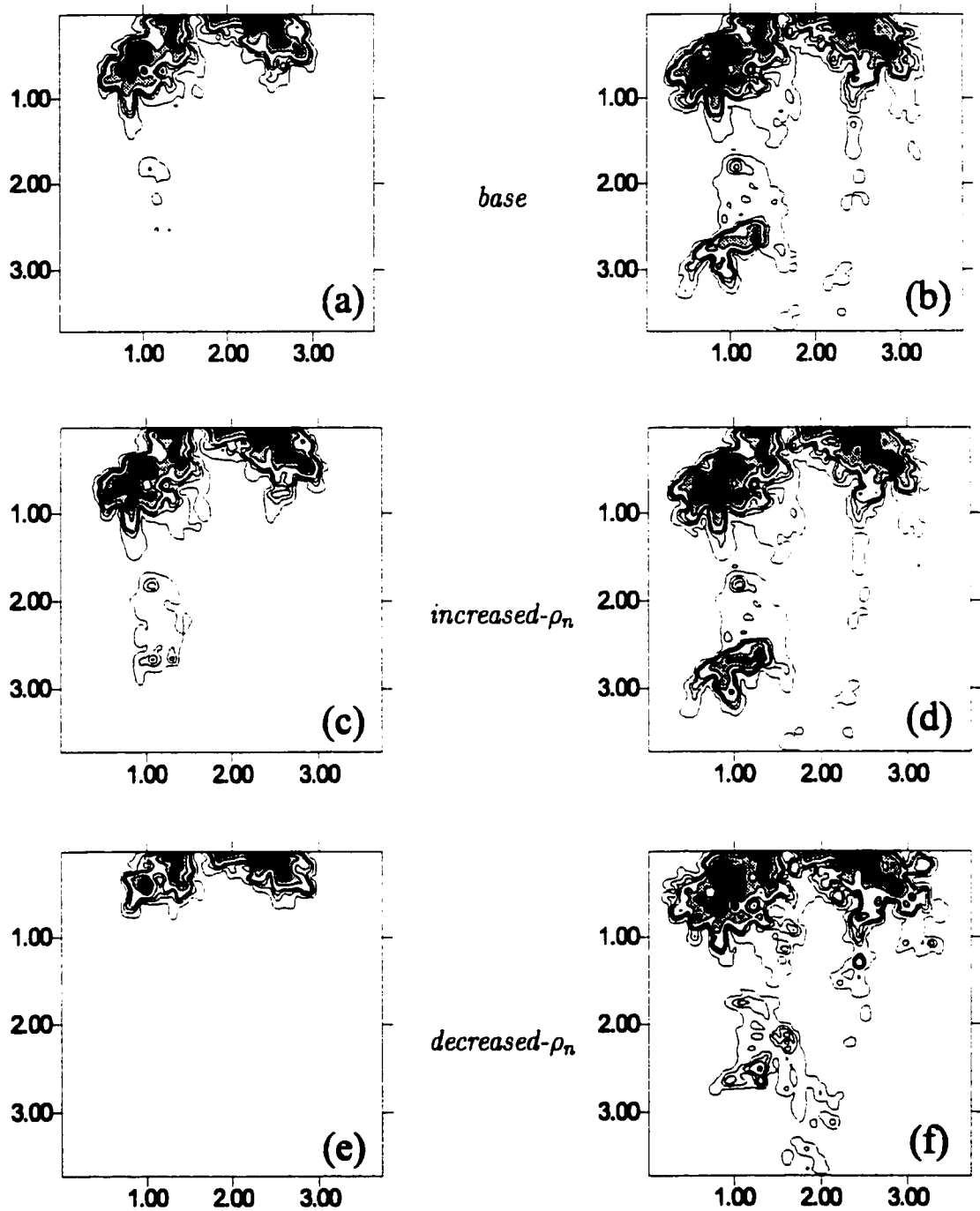
Figure 4.18: Intermediate (a,c,e) and final (b,d,f) NAPL distributions for variations in NAPL density. Intermediate saturations are at t=300 s, and final saturations are at the point where NAPL reaches the base of the fracture (i.e., variable time). Refer to Table 4.4 for an explanation of density perturbations. The contour interval is as given in Figure 4.3.

was decreased. It appears that at the intermediate time (t=300 s), the NAPL front is advanced (*increased-ρ_n*) or attenuated (*decreased-ρ_n*). This is consistent with the variation in total travel times. It is difficult to tell if there are significant changes in NAPL distributions that cannot only be attributed to variations in NAPL flow velocity. It is clear, however, from the final distributions, that the NAPL distributions are ultimately different. The final distribution for simulation *increased-ρ_n*, when compared with the base case, does not show much difference. This suggests that the density chosen for the base case was already reasonably high, and the effect of further upward perturbations would be minimal. The final distribution for simulation *decreased-ρ_n* is somewhat different than the base case. Figure 4.19 shows intermediate and final NAPL saturation profiles from B-B' (Figure 4.4). It can again be seen that there is little difference in NAPL distribution from the base case to simulation *increased-ρ_n*, while in simulation *decreased-ρ_n* the NAPL saturations are both lower and attenuated. When the NAPL density is reduced, the force which drives the NAPL to flow downwards is also reduced due to a decrease in capillary pressure. Lower capillary pressures result in lower saturations (cf., Figure 3.4). The area in the lower left near Intersection 3 shows this particularly well. The total travel time taken also influences the final NAPL distributions in the case where NAPL density is reduced. The additional simulation time allows NAPL to move further in areas with higher saturations (i.e., near the source).

Figure 4.20 shows the intermediate and final saturation distributions for perturbations in NAPL viscosity. Changing NAPL viscosity does not affect final NAPL distributions, but does affect quite dramatically the distributions at the intermediate time levels. The reasons behind why increasing or decreasing NAPL viscosity change NAPL travel time were given in Section 4.4.1. To summarize, changing the NAPL viscosity serves to increase or decrease the rate of flow; that is, distributions are constant but scaled in time.
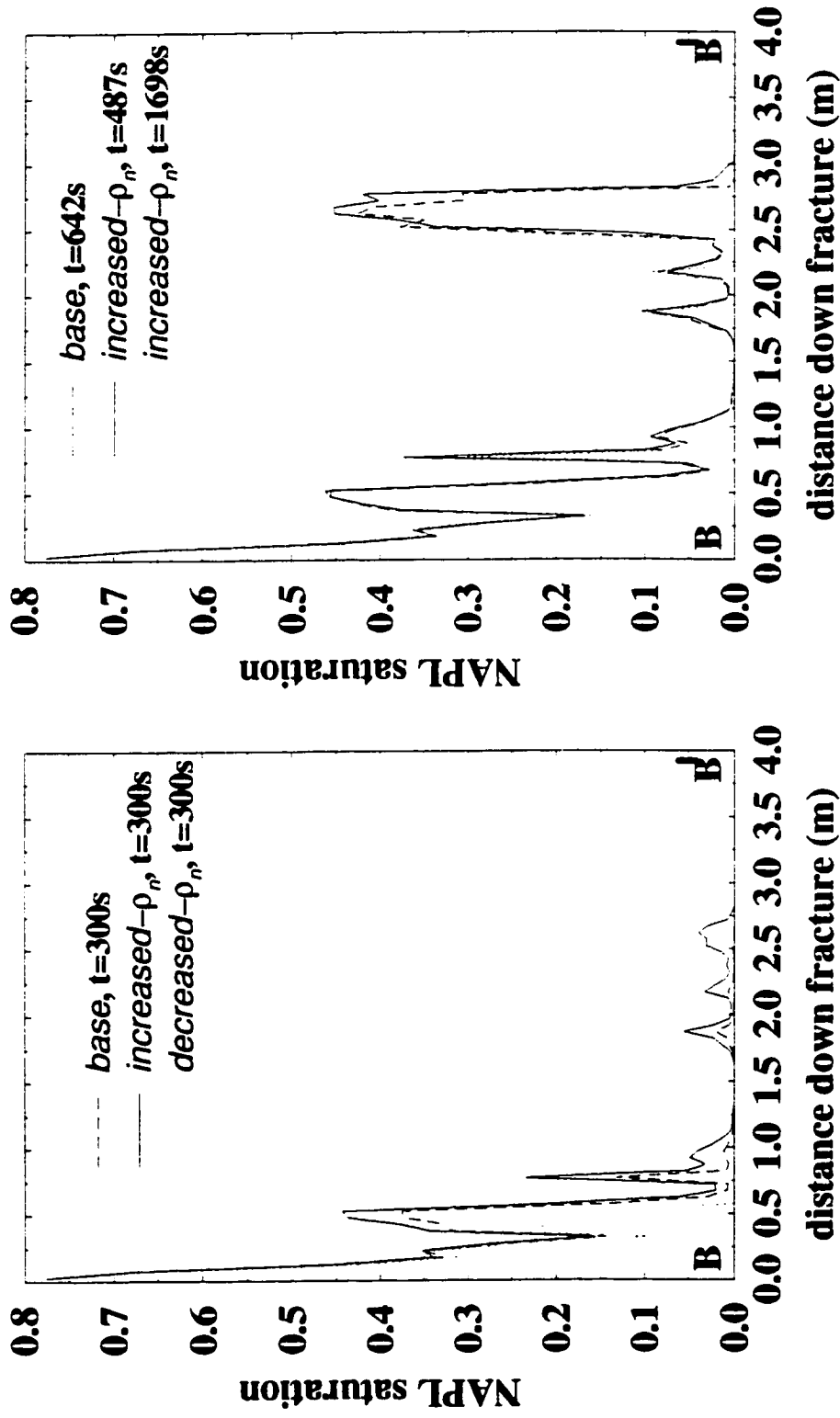
Figure 4.19: (a) Intermediate and (b) final NAPL saturation profiles for perturbations in NAPL density.
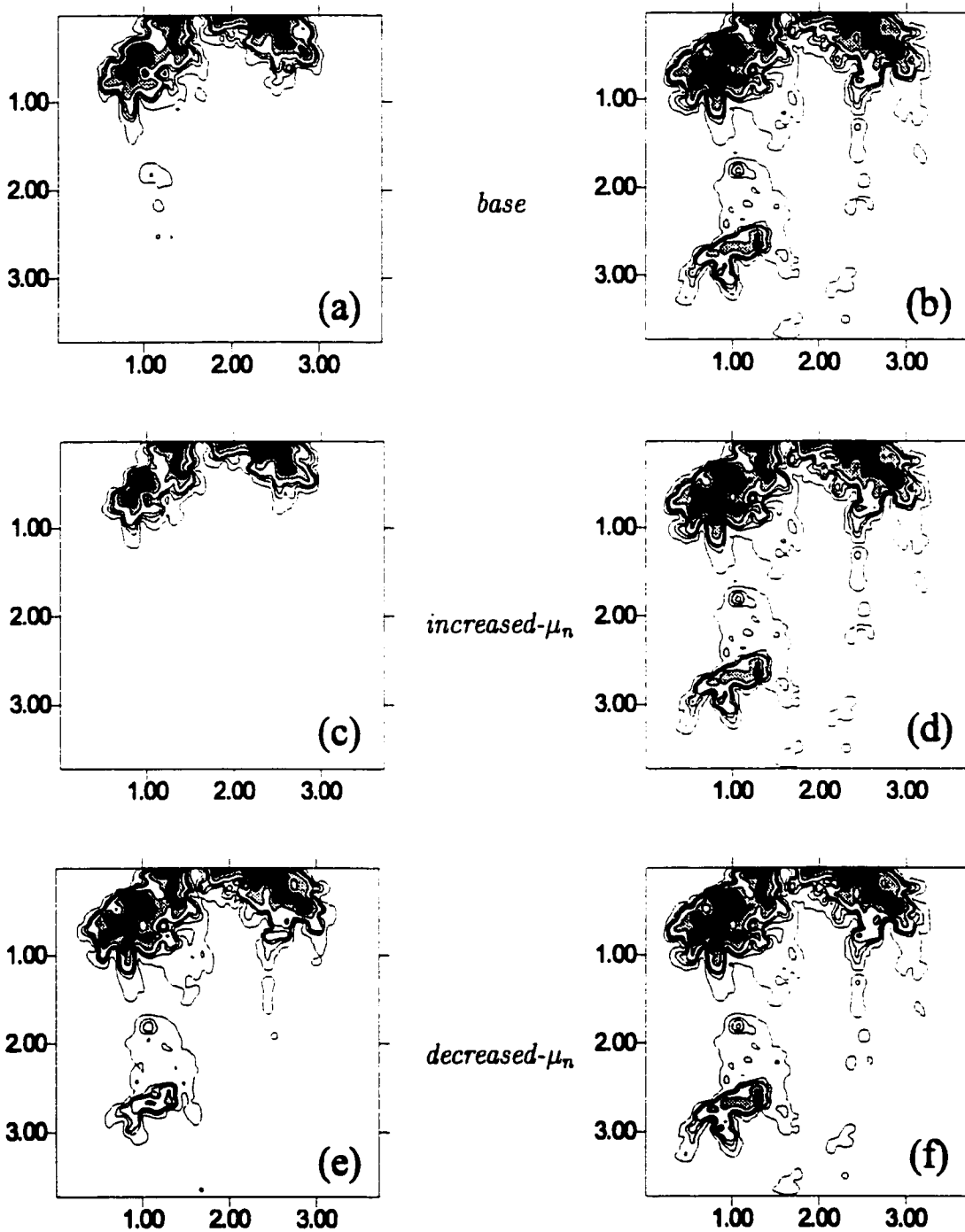
Figure 4.20: Intermediate (a,c,e) and final (b,d,f) NAPL distributions for variations in NAPL viscosity. Intermediate saturations are at t=300 s, and final saturations are at the point where NAPL reaches the base of the fracture (i.e., variable time). Refer to Table 4.4 for an explanation of viscosity perturbations. The contour interval is as given in Figure 4.3.

NAPL distributions - Aperture field properties

As noted above, the choice of mean aperture appears to significantly impact the total real simulation time. From Figure 4.21, it is also clear that in addition to the travel time changing, the final NAPL distributions are strongly affected, particularly in the case where the mean is decreased. It was also noted above that the apparent net aperture field variance decreases in the case where a smaller mean aperture is chosen. This is supported in Figure 4.21(c), as a much more evenly distributed NAPL front is observed. There is little change from the base case to simulation *increased-Y*. This suggests that the mean chosen for the base case is sufficiently large such that upward perturbations make little difference in terms of NAPL occupancy. The minimum and maximum aperture values are also more similar than in simulation *decreased-Y*.

Figures 4.22 and 4.23 show horizontal and vertical final NAPL profiles for simulations corresponding to Figure 4.21. These profiles demonstrate that the NAPL fronts are advanced or attenuated as the mean aperture is increased or decreased. The D-D' profile, however, shows a slightly different NAPL distribution. For the simulation *decreased-Y*, there is a visible "spike" at roughly $z = 1.25$ m, where the saturation is larger than that for the base case and simulation *increased-Y*. The reason for this spike and for the other differences is that in the case with a smaller aperture mean, the NAPL has had longer to accumulate because the overall rate of migration is slower. This manifests itself more strongly in larger aperture blocks above very small aperture blocks, where NAPL tends to pool, and at lower saturations, where the relative change in saturation between the base and *decreased-Y* cases is more pronounced.

Figure 4.24 shows that the final distributions for perturbations in field variance are strikingly similar to those of Figure 4.21. This supports the assertion made above, that reducing the mean for the same ln-variance results in a similar, albeit scaled, aperture field. Here, the total travel time is less affected than in cases *increased-Y* and *decreased-Y*; however, the final NAPL distributions are similarly affected.

In Figure 4.25(d), it can be seen that the NAPL distribution is much less spread
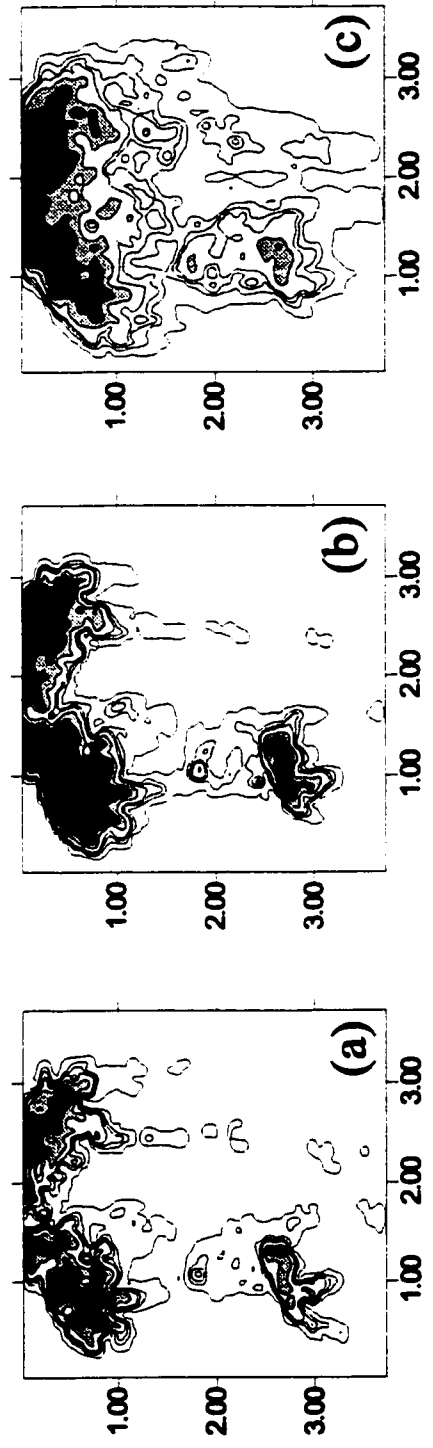
Figure 4.21: Final NAPL distributions for variations in Y. Refer to Table 4.4 for an explanation of Y perturbations.
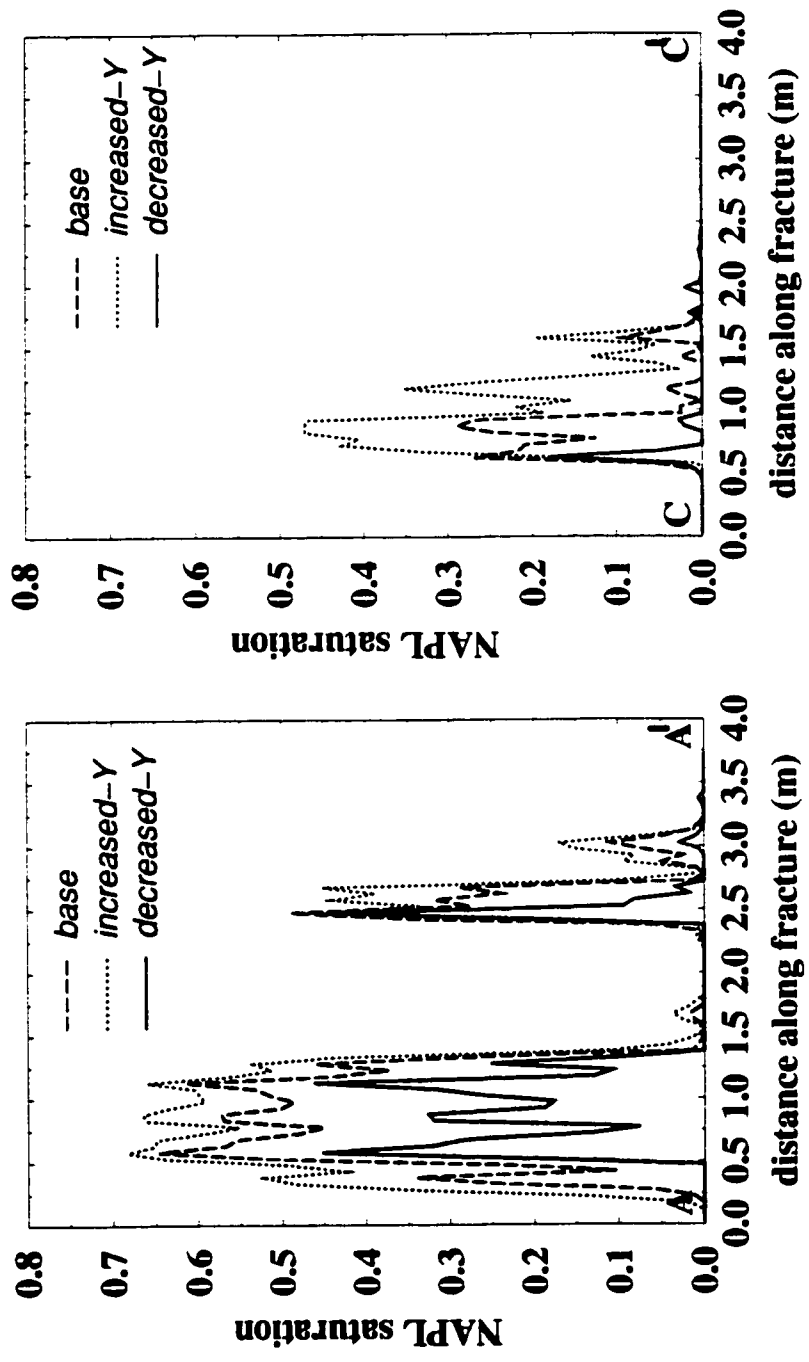
Figure 4.22: Horizontal profiles along A-A' and C-C' through time at the final NAPL distribution for perturbations in aperture mean.
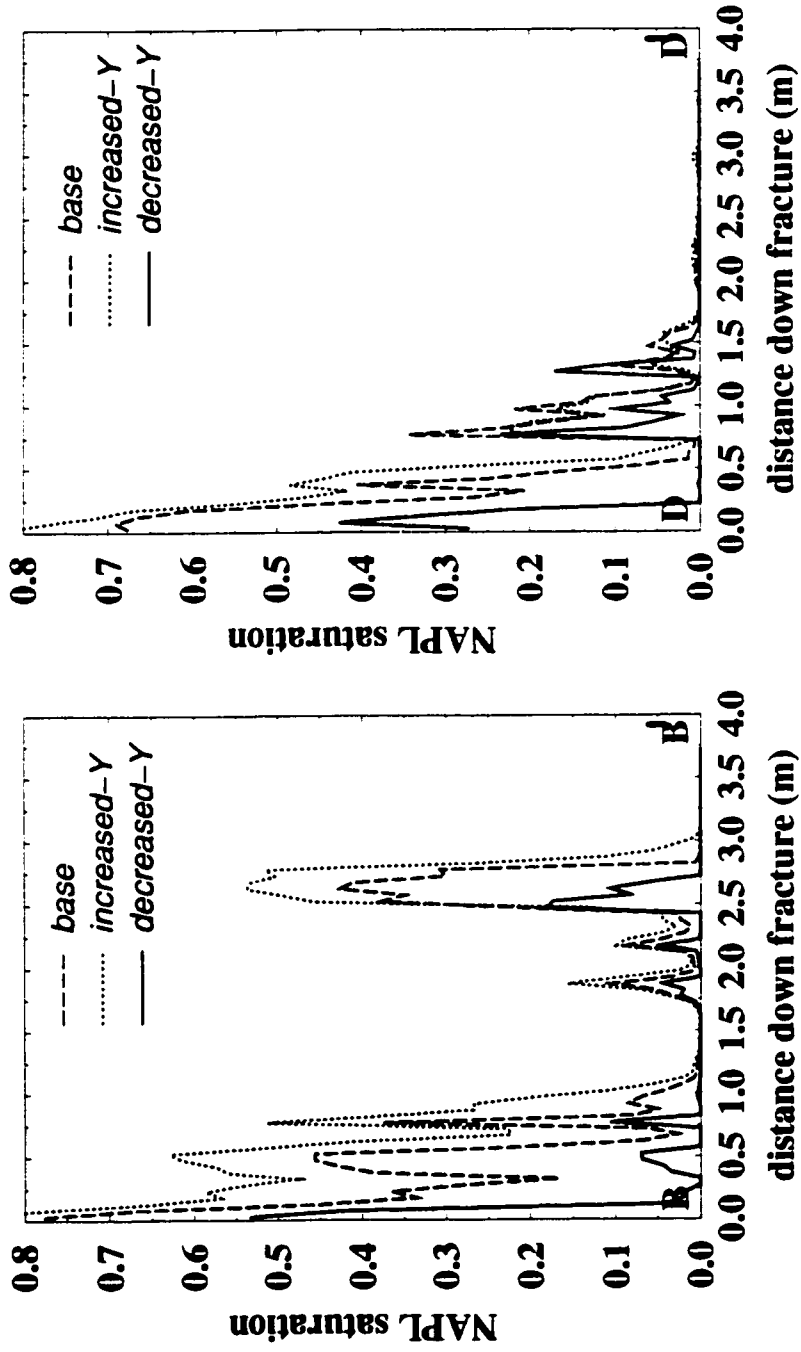
Figure 4.23: Vertical profiles along B-B′ and D-D′ through time at the final NAPL distribution for perturbations in aperture mean.

Figure 4.24: Intermediate (a,c,e) and final (b,d,f) NAPL distributions for variations in σ_Y^2. Intermediate saturations are at t=300 s, and final saturations are at the point where NAPL reaches the base of the fracture (i.e., variable time). Refer to Table 4.4 for an explanation of σ_Y^2 perturbations. The contour interval is as given in Figure 4.3.

Figure 4.25: Intermediate (a,c,e) and final (b,d,f) NAPL distributions for variations in correlation lengths. Intermediate saturations are at t=300 s, and final saturations are at the point where NAPL reaches the base of the fracture (i.e., variable time). Refer to Table 4.4 for an explanation of correlation length perturbations. The contour interval is as given in Figure 4.3.

out across the fracture. Increasing the correlation length serves to provide the NAPL with more interconnected apertures of similar (larger) size, leading to this distribution. Conversely, reducing the correlation length effectively makes the aperture field more spatially heterogeneous, thereby resulting in a more distributed NAPL front as NAPL encounters more small apertures in its preferential flow path.

NAPL distributions - Boundary condition definition

Changes in intermediate and final NAPL distributions result from changes in the height of the column of NAPL above the fracture. Figure 4.26 illustrates these distributions. In the case where the NAPL column height is decreased (*decreased-H*), the NAPL does not exert as much pressure at the top of the fracture and hence there are lower initial saturations at the top of the fracture; the converse is true for an increase in NAPL column height. At the final time step, there is little apparent difference between the base case and simulation *increased-H*. There is a more pronounced difference between the base case and simulation *decreased-H*, where a significant amount of time had passed such that NAPL had the opportunity to enter and accumulate in more areas in the interior of the fracture.

Changing the water flow field had a significant impact on the intermediate and final NAPL distributions in the fracture (Figure 4.27). Clearly, the water flow assisted and impeded NAPL flow through the fracture in simulations *increased-δ* and *decreased-δ*, respectively. In Figure 4.27(d), a vertically thinner distribution of NAPL is manifested, whereas in Figure 4.27(f), a much wider distribution of NAPL, especially near the source, can be seen.

Recall that capillary pressure is defined as the difference between NAPL pressure and water pressure. Thus, as water flows upwards in the fracture, the capillary pressure at the NAPL/water interface is lowered such that advancement of the front is impeded. This encourages NAPL to flow to the sides, where water pressures are lower. The NAPL can still flow downwards in areas with larger apertures, which correspond to lower required entry pressures (Equation 2.6). However, as less NAPL
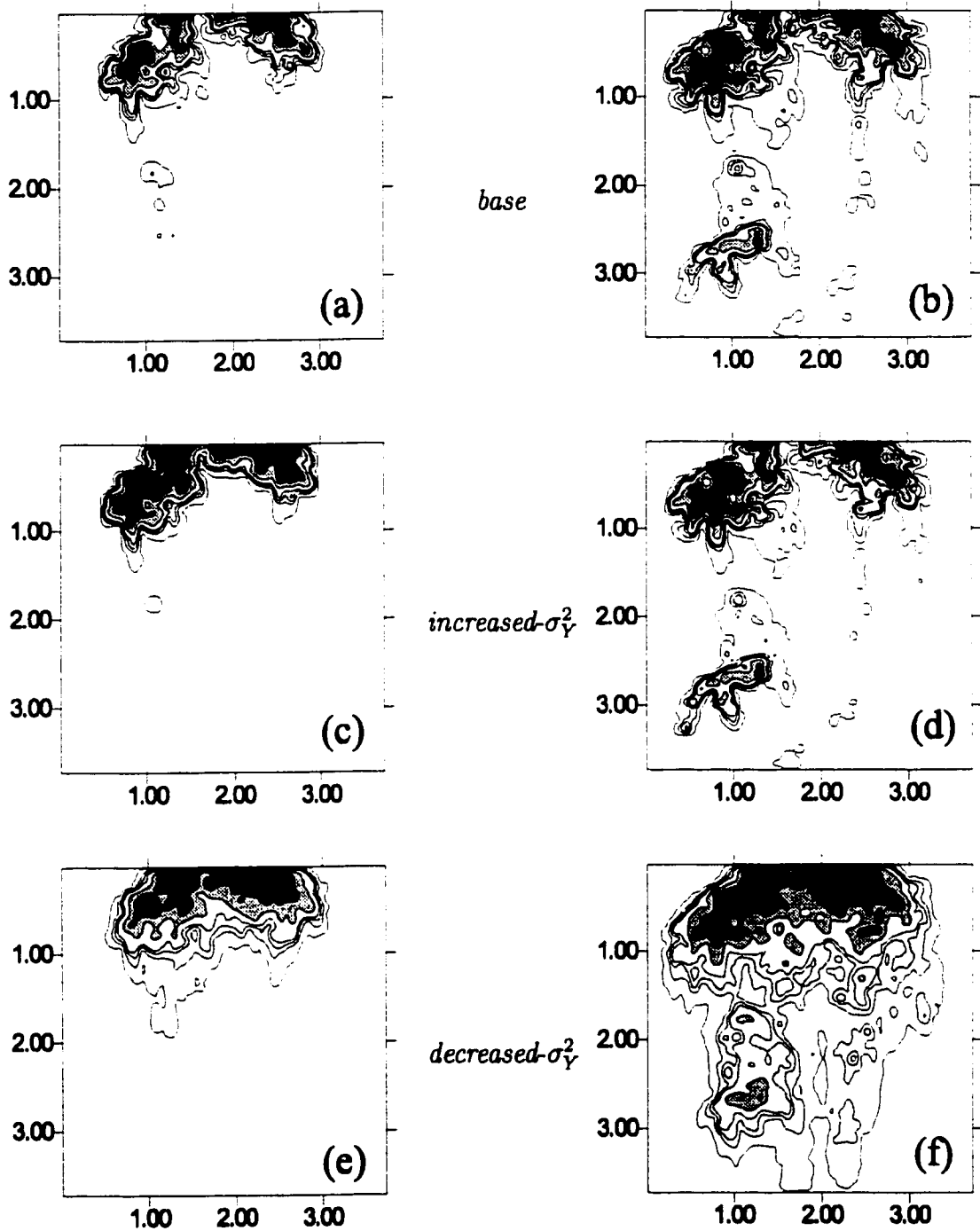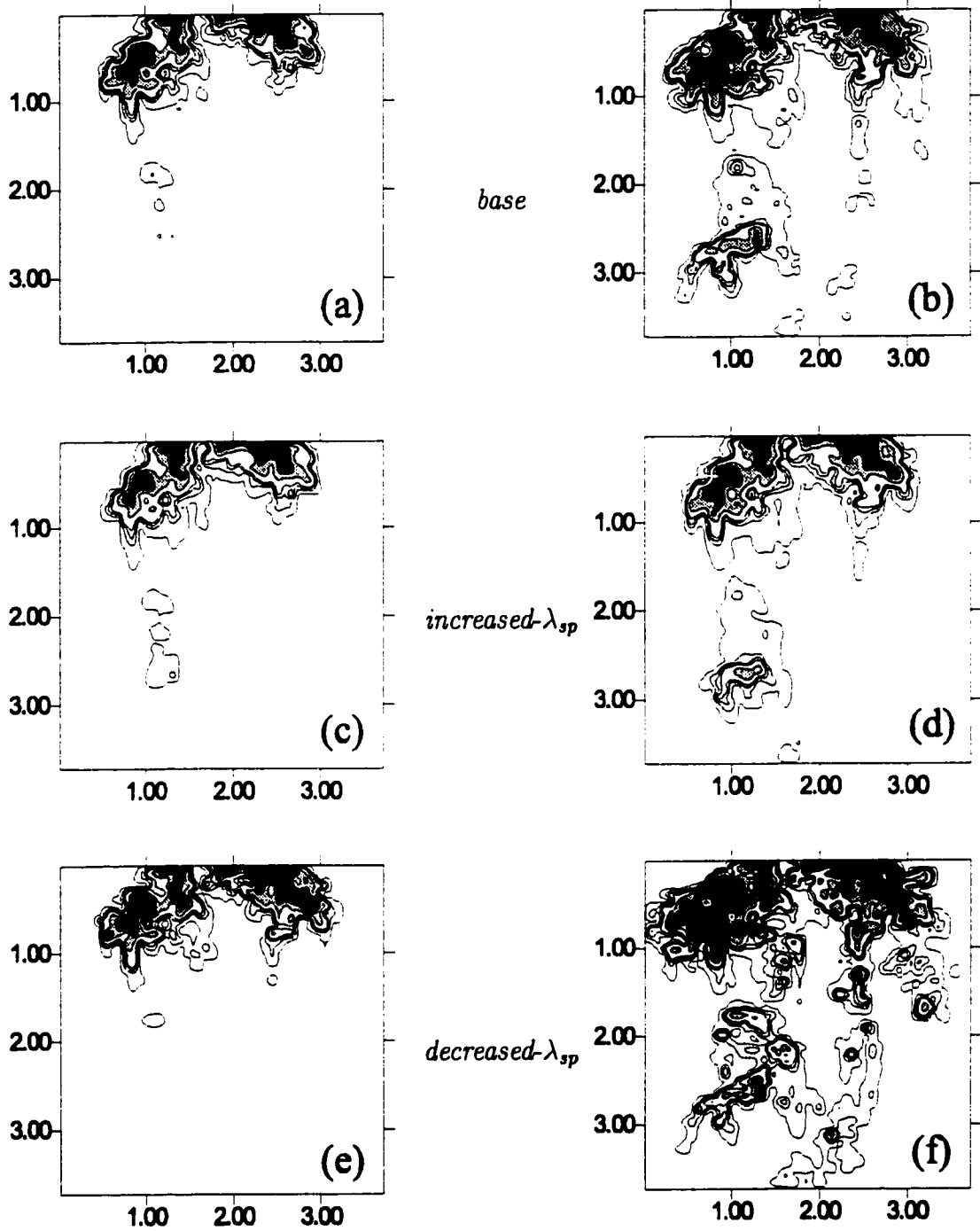
Figure 4.26: Intermediate (a,c,e) and final (b,d,f) NAPL distributions for variations in NAPL column height. Intermediate saturations are at t=300 s, and final saturations are at the point where NAPL reaches the base of the fracture (i.e., variable time). Refer to Table 4.4 for an explanation of NAPL column height perturbations. The contour interval is as given in Figure 4.3.
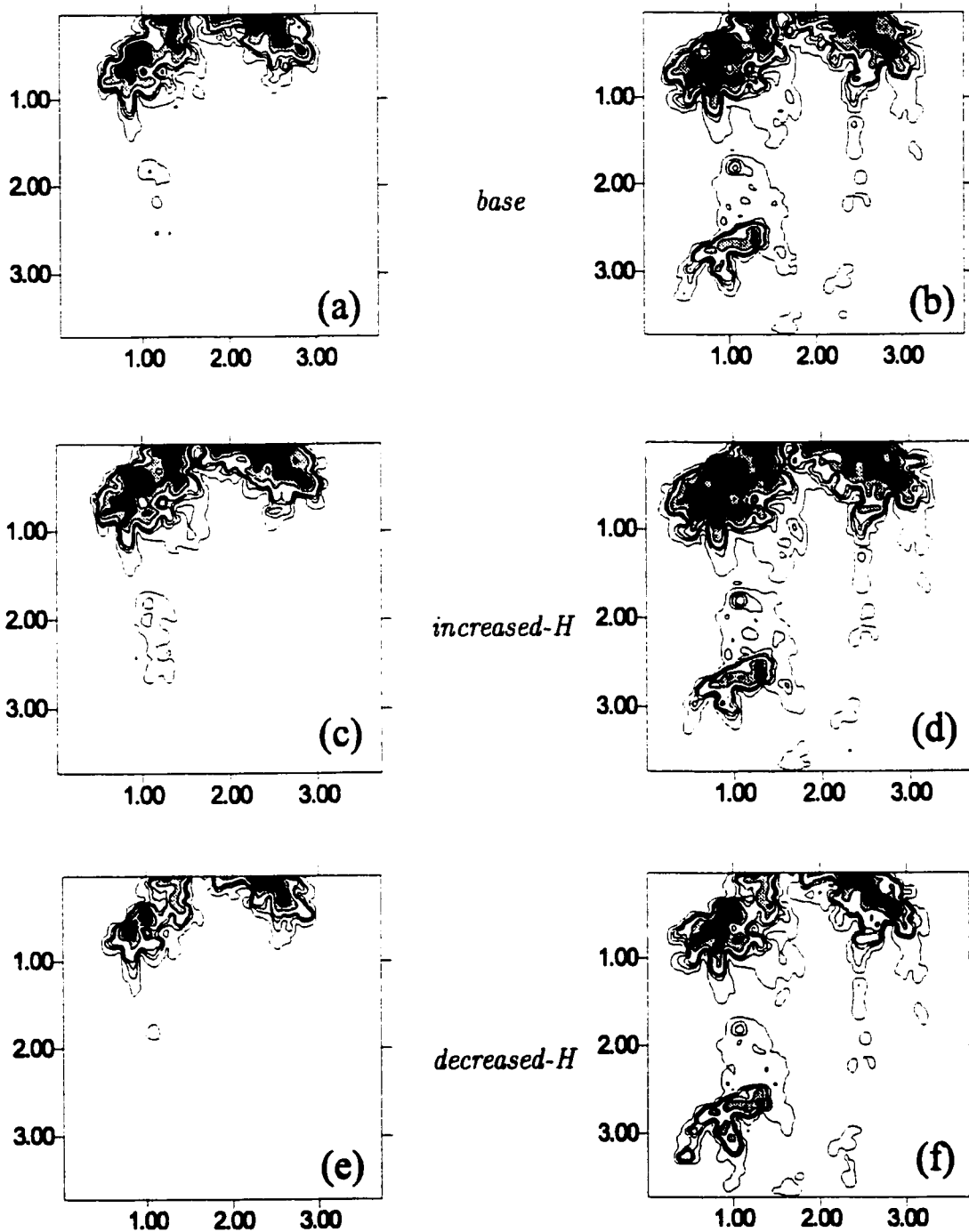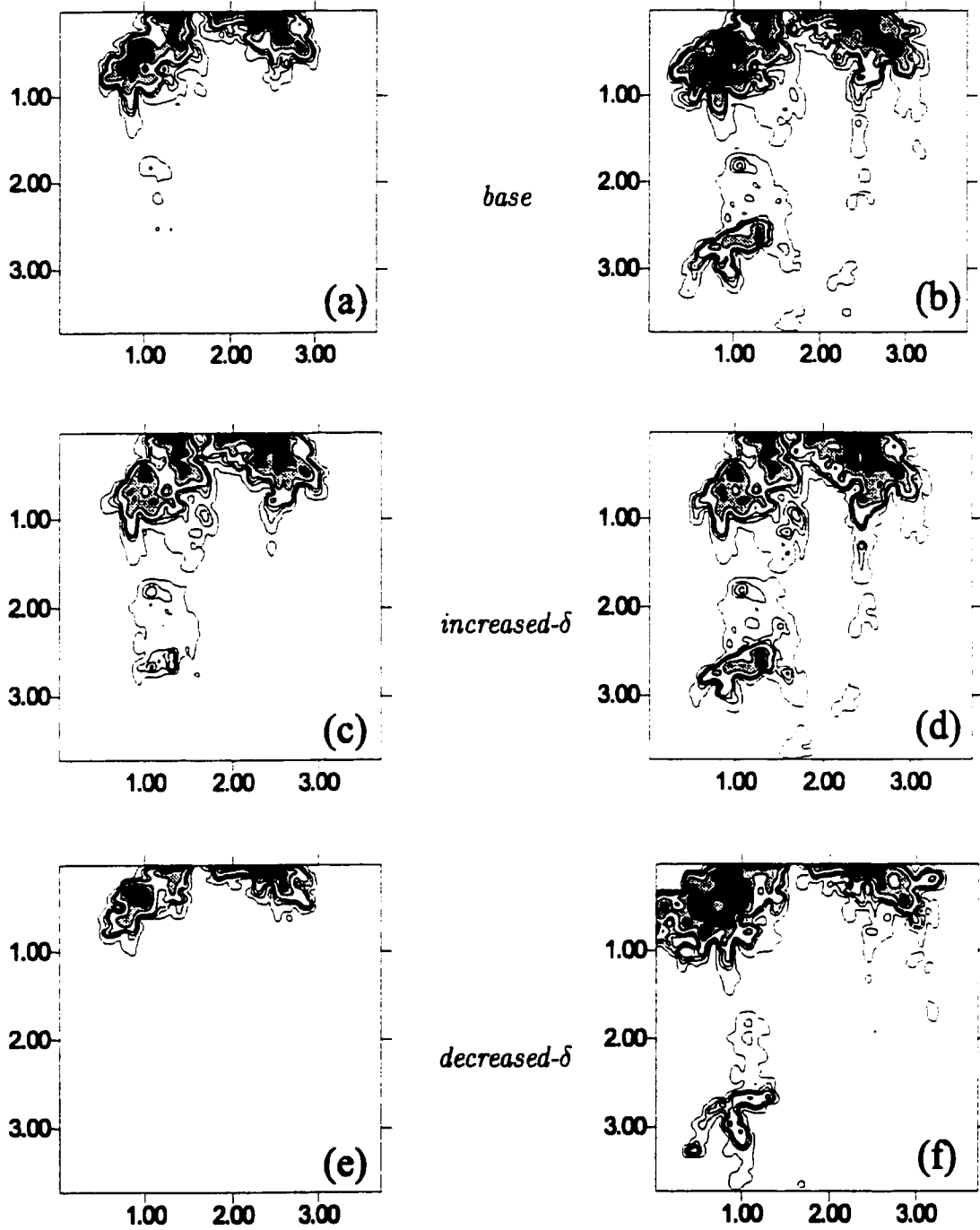
Figure 4.27: Intermediate (a,c,e) and final (b,d,f) NAPL distributions for variations in water flow field gradient. Intermediate saturations are at t=300 s, and final saturations are at the point where NAPL reaches the base of the fracture (i.e., variable time). Refer to Table 4.4 for an explanation of water flow field gradient perturbations. The contour interval is as given in Figure 4.3.

is permitted to flow downwards, a much smaller area of NAPL is observed in the lower left quadrant of the fracture.

4.5 Effect of Parameter Sensitivity on Transport

Recall that concentrations in the fracture blocks are constrained to the solubility limit whenever a threshold volume of NAPL occupies the block. Therefore, the distribution of dissolved contaminant in the fracture, and correspondingly in the matrix, is strongly dependent on the distribution of free-phase NAPL in the fracture. The total amount of mass that is available to diffuse into the matrix is similarly linked to the free-phase distribution of NAPL. In addition, the total travel time is also expected to influence the total amount and distribution of mass in the fracture and in the matrix, as mass will continue to diffuse according to the concentration gradient until such a time as the gradient becomes negligible. The importance of matrix diffusion as a mechanism for mass removal from a fracture is noted by Ross and Lu (1999) as increasing for longer NAPL migration times. For these reasons, only those parameters that do not have a major impact on NAPL migration times are chosen for further analysis with respect to transport.

4.5.1 Mass Flux Behaviour and Total Mass Diffused

The magnitude of the mass flux and the amount of mass that diffuses into the matrix are very closely related, and thus will be treated concurrently. Figure 4.28 shows summaries of the total mass diffused into the matrix for each of the four sensitivity categories. Clearly, contaminant properties and matrix properties are the two most sensitive classes of parameters. In particular, diffusion coefficient, matrix porosity, and NAPL solubility seem to influence the total amount of mass diffused into the matrix the most, because these parameters factor directly into the definition of mass flux across the fracture/matrix interface. This observation is consistent with observations by Parker et al. (1994), who found that the mass lost from the fracture,
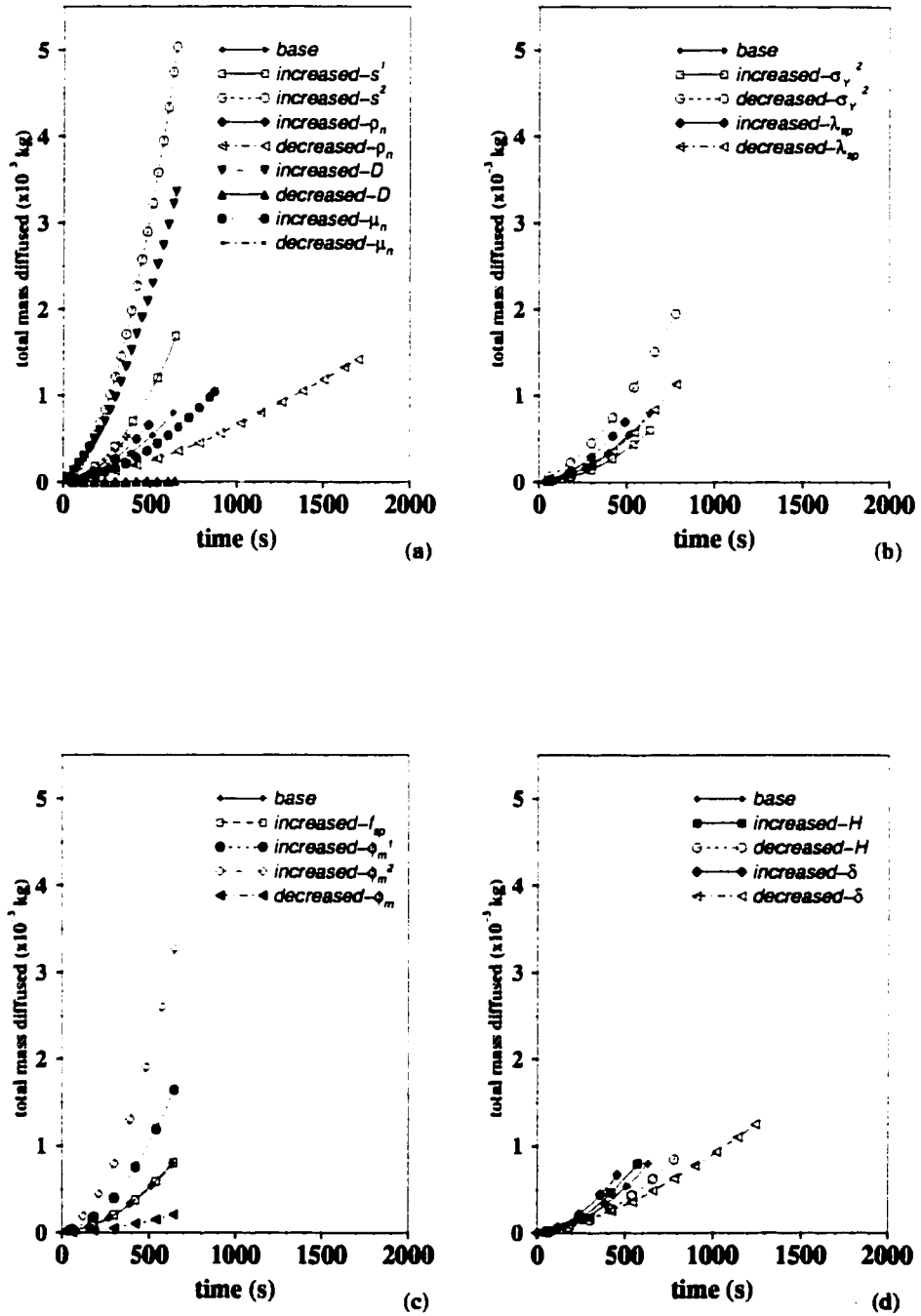
93

Figure 4.28: Total mass diffused into the matrix versus time for variations in (a) contaminant properties, (b) aperture field properties, (c) matrix properties, and (d) boundary condition properties. The graphs are plotted on the same scale. An explanation of the parameter changes is given in Table 4.4.

and hence the mass gained by the matrix, is proportional to the matrix porosity, solubility, effective diffusion coefficient, and time of diffusion.

As the solubility increases, the total amount of mass that can diffuse into the matrix increases correspondingly. This leads to an increase in the concentration gradient out of the fracture, and subsequently more mass diffuses out. An increased diffusion coefficient also increases the strength of the diffusive process, by defining a faster rate of diffusion for the same concentration gradient. It is conceded that the diffusion coefficient chosen for the base case and most of the sensitivity simulations is high for diffusion in water; however, this parameter was chosen to enhance the overall processes occurring and make the data analysis more straightforward. In addition to the initial sensitivity simulations, the most sensitive parameters, NAPL solubility and matrix porosity, were simulated with a more realistic diffusion coefficient of 1.0 $\times 10^{-10}$ m/s. The results of these simulations are given in Section 4.5.3.

Figure 4.29 shows the total mass diffused out of the fracture for simulations *base*, *increased-D*, *increased-ϕ_m^2*, and *increased-s^2*, plotted on log-log axes. It can be clearly seen that the case where the diffusion coefficient is increased shows a characteristically different slope from the other simulations. This implies that the rate of diffusion decreases more with time than for the other simulations. This is consistent with the gradient of the mass flux in time, which also decreases more rapidly. Figure 4.30 shows temporal relative concentration profiles at the first matrix block behind Intersection 1. The relative concentrations clearly are much higher earlier for simulation *increased-D*, and finish with higher concentrations in the matrix. That the relative concentration lines for the base case and simulation *increased-s^2*, where the solubility is increased, are concurrent supports the earlier supposition that the increase in the total mass diffused can be entirely attributed to the increase in the amount of mass in the fracture.

It still remains to be demonstrated why the total mass diffused increases so much for the case where matrix porosity is increased. From Fick's second law of diffusion (Equation 2.29), it can be seen that concentrations in the matrix are independent
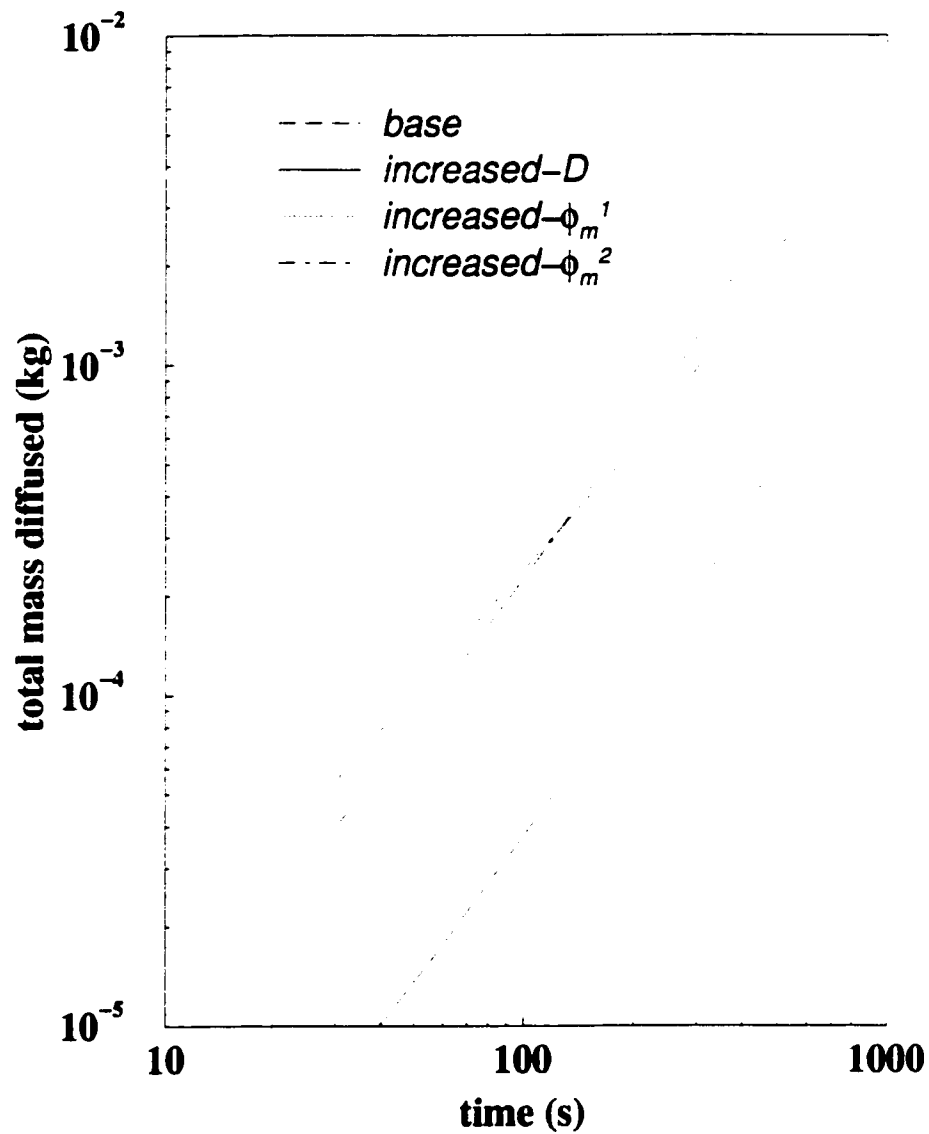
Figure 4.29: Total mass diffused into the matrix versus time for simulations base, increased-D, increased-ϕ_m^2, and increased-s^2.
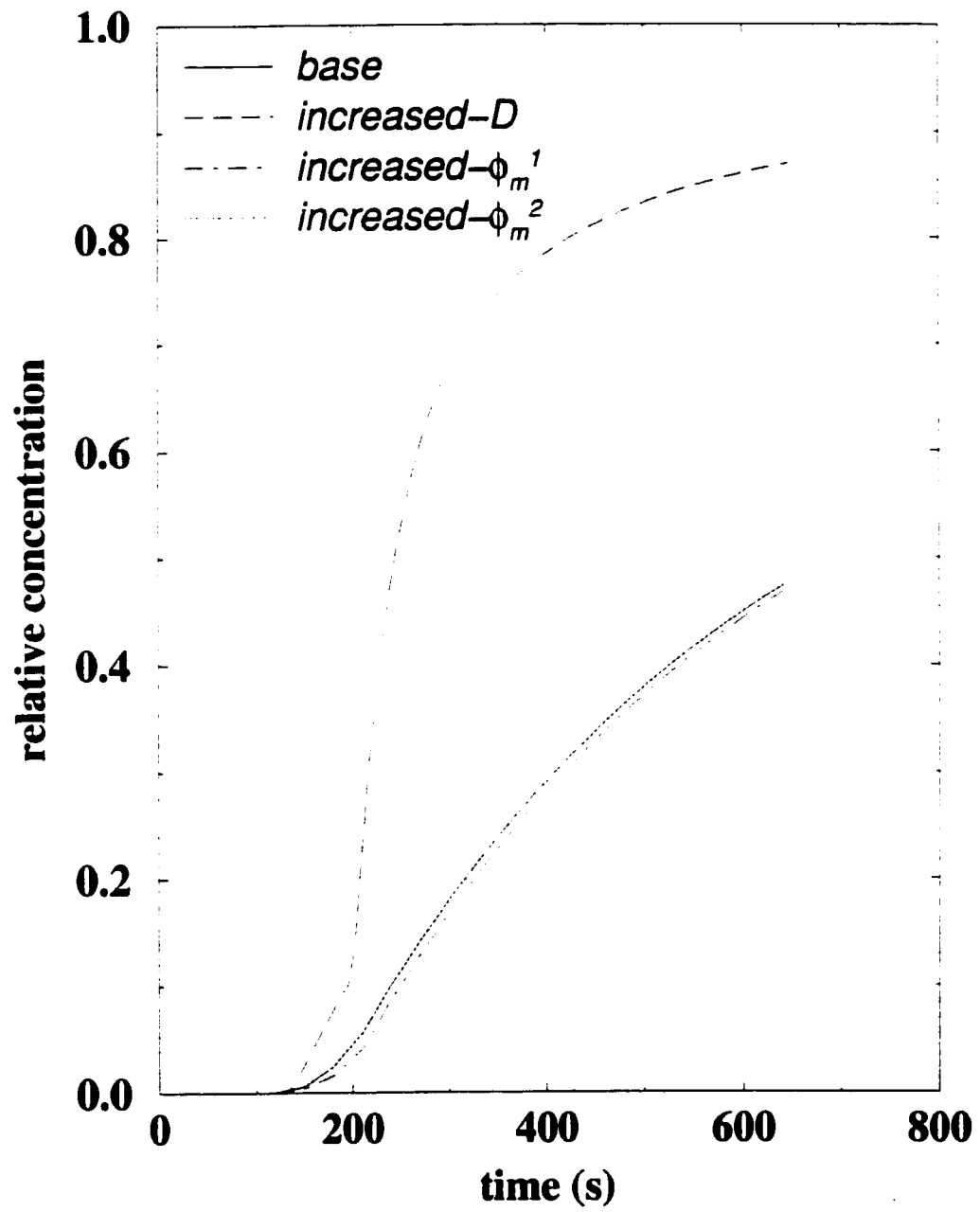
Figure 4.30: Temporal relative concentration profiles for the first matrix block behind Intersection 1.

of porosity, if porosity is uniform in space and time. However, from Fick's first law (Equation 2.28), the mass flux is directly proportional to the matrix porosity. Therefore, the total mass diffused into the matrix must increase with increased matrix porosity. Also, the amount of mass in any one block is defined as the concentration in the block multiplied by its porosity. It follows that the blocks in the matrix contain more mass in case $increased\text{-}\phi_m^1$ and $increased\text{-}\phi_m^2$ than in the base case.

4.5.2 Concentration Profiles

For reasons stated above, the analyses of concentration profiles spatially and temporally were not considered valuable in cases where NAPL distributions in the fracture vary considerably from the base case. As such, the only profiles considered were those for the simulations base, $increased\text{-}s^1$, $increased\text{-}s^2$, $increased\text{-}D$, $decreased\text{-}D$, $increased\text{-}\phi_m^1$, $increased\text{-}\phi_m^2$, and $decreased\text{-}\phi_m$.

Spatial Profiles

The spatial distribution of diffused NAPL in the matrix was plotted for all of the above cases. In all cases except for $increased\text{-}D$ and $decreased\text{-}D$, the relative concentration profiles did not change. The profile comparing the base case and simulation $increased\text{-}D$ is presented in Figure 4.31. The concentration in the matrix block is independent of the porosity; only the mass flux and total mass diffused are affected. For NAPL solubility perturbations, the relative concentrations remain unaffected, even though the absolute (non-normalized) concentrations increase. For the case where the fracture spacing was made smaller, only a very small difference in total mass diffused into the matrix was seen; that is, the total mass increased by roughly 4%. This increase can be attributed to the accumulation of mass at the end of the matrix blocks, where the zero diffusive flux boundary does not allow mass to continue to diffuse.
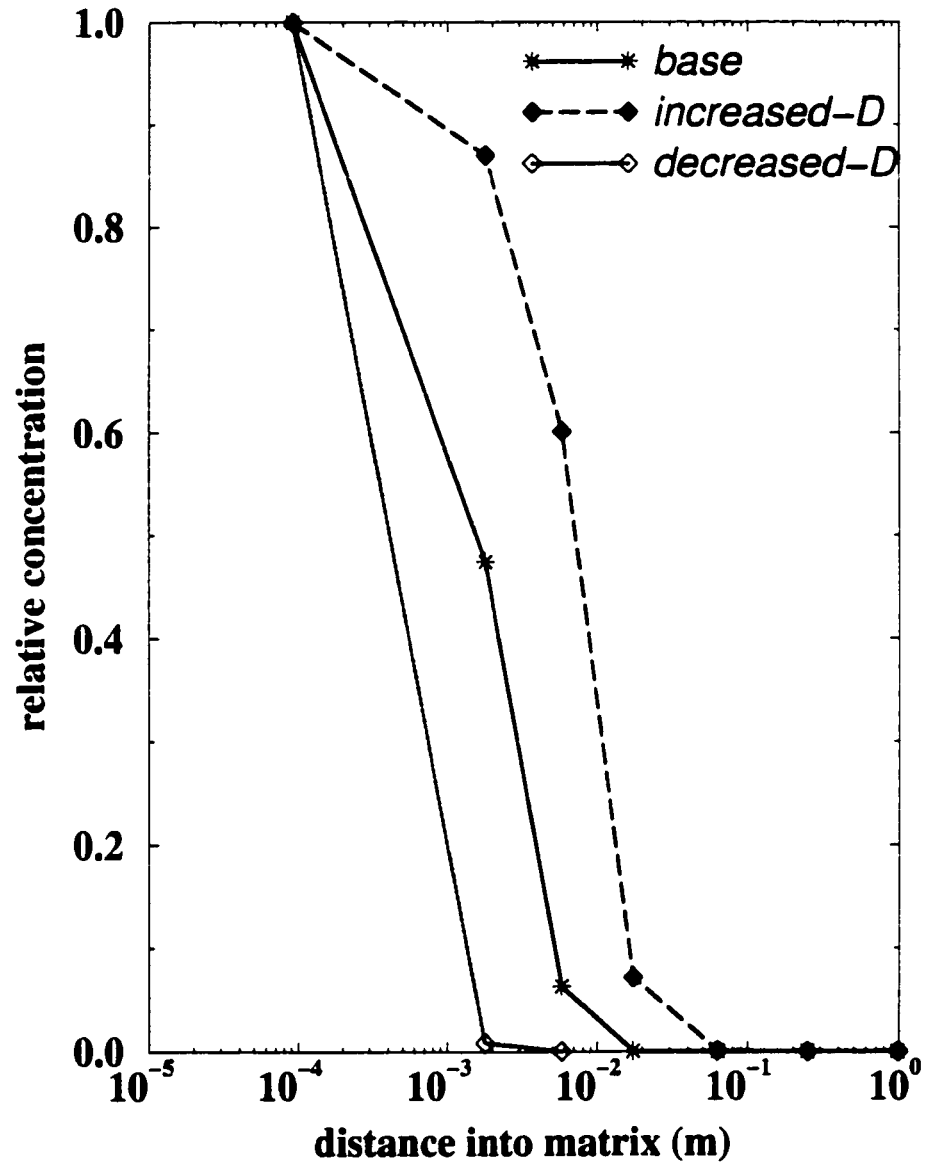
Figure 4.31: Concentration profile into the matrix at Intersection 1 for the base case, *increased-D*, and *decreased-D* for the final saturation distribution.

Simulation ID	Changed Parameter and Value	Units	D^*	Units
$incr\text{-}s/decr\text{-}D$	s=0.90	kg/m^3	1.0×10^{-10}	m^2/s
$incr\text{-}\phi_m/decr\text{-}D$	ϕ_m=0.8	-	1.0×10^{-10}	m^2/s

Table 4.6: Summary of parameter changes for additional simulations involving a lower value for D^*.

4.5.3 Additional Diffusion Simulations

In order to examine the relationship between the diffusion coefficient and other parameters of sensitivity, two additional simulations were performed. The first perturbed both the NAPL solubility ($s = 0.9$ kg/m^3) and the diffusion coefficient ($D^* = 1.0 \times 10^{-10}$ m^2/s). The second perturbed both the matrix porosity ($\phi_m = 0.8$) and the diffusion coefficient ($D^* = 1.0 \times 10^{-10}$ m^2/s). Table 4.6 summarizes these simulations. Figure 4.32 shows the total mass diffused results for these simulations.

From Figure 4.32, it can be seen that the general shape of each of the curves remains unaffected for perturbations in the diffusion coefficient. In addition, the spacing between the simulations where the porosity and solubility were perturbed remains virtually unaffected with changes in the diffusion coefficient. This plot again demonstrates the importance of the choice of diffusion coefficient in model inputs. From this analysis, it appears that the diffusion coefficient acts to scale the mass diffused in time in more or less the same manner from one sensitivity simulation to the next.

4.6 Coupling of Flow and Transport

Total travel time, NAPL distributions, total mass diffused, and concentration distributions are all considered to be important indicators of the strength of coupling between flow and transport. The parameter perturbations of NAPL solubility, diffusion coefficient, fracture spacing, and matrix porosity all provide direct insight into how the system is impacted by dissolution and subsequent aqueous phase transport.
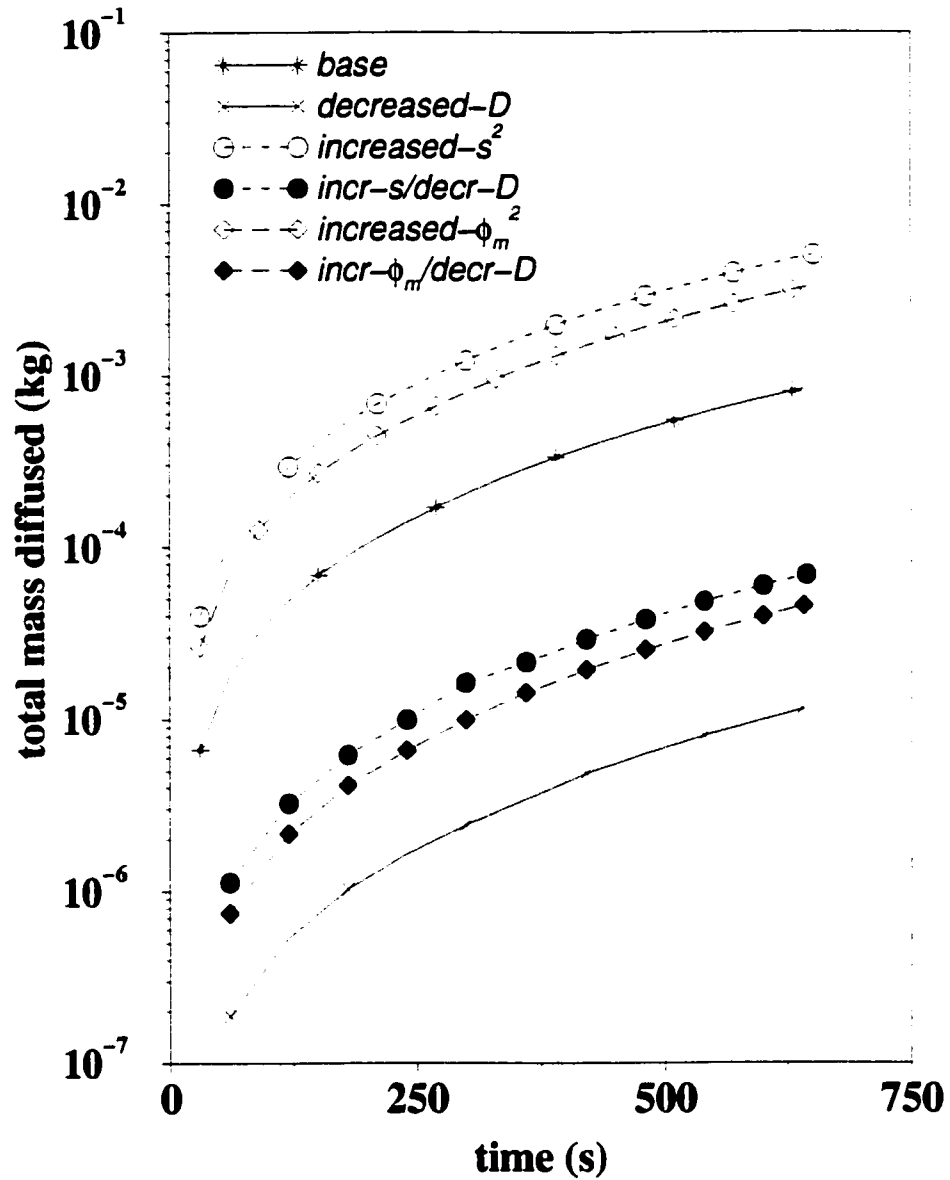
Figure 4.32: Total mass diffused for the base case, simulation *decreased-D*, and the additional simulations involving solubility and porosity. Refer to Tables 4.4 and 4.6 for explanations of parameter changes.

Of these parameters, NAPL solubility appeared to provide the greatest sensitivity to simulation results. When the NAPL solubility was increased, the time taken for the NAPL to traverse the fracture was the most significantly impacted, increasing by about 1.5%. In addition, increasing the NAPL solubility led to larger increases in the amount of mass diffused into the matrix than for the other parameters. Increasing the solubility acts to increase the absolute concentrations in the fracture and in the matrix, but does not affect the relative concentration values. These values are scaled by the absolute solubility. It follows from this analysis that for a NAPL with a much higher solubility, such as bromochloromethane with a solubility of 16700 mg/L (Cohen and Mercer, 1993), this coupling could become far more significant. These simulations were not undertaken due to the numerical instability of the model in solving simulations with very strong coupling. Modifications would have to be made to the model before attempting to solve such a difficult problem.

The diffusion coefficient also had an impact on the apparent coupling between flow and transport. When the diffusion coefficient was increased, the travel time for NAPL to reach the base of the fracture was increased, although by a smaller amount than for solubility. This factor is most directly related to the strength of the mass transfer from the fracture to the porous matrix. In addition to altering the total NAPL travel time, the simulation results demonstrate that the diffusion coefficient also affects the distribution of diffused NAPL in the porous matrix. This can have implications for remediation of NAPL contaminated sites, as the further into the matrix dissolved mass diffuses, the longer it will take to diffuse back out (Parker *et al.*, 1994).

4.7   Summary

Flow of NAPL with simultaneous dissolution and aqueous phase transport in a discrete, rough-walled fracture has been simulated with the aid of the computer program **FaTMatD**. This model also simulates matrix diffusion out of the fracture into the surrounding porous matrix. It was found that the NAPL density, NAPL viscosity,

mean aperture, aperture variance, correlation length, NAPL column height, and initial water column flow field definition affect the NAPL flow velocity to the greatest degree. Final NAPL distributions were the most sensitive to perturbations in NAPL density, mean aperture, aperture variance, correlation length, and initial water column flow field. Solubility, matrix porosity, and diffusion coefficient had the greatest direct affect on matrix diffusion.

Chapter 5

Conclusions and Suggestions for Further Study

The primary objective of this study was to investigate the relationship between non-aqueous phase liquid flow and subsequent aqueous phase transport in a discrete, rough-walled fracture and the surrounding porous matrix. The strength of the coupling between two-phase flow and transport, including matrix diffusion, is an area of study that has been largely ignored in the literature, particularly in the context of a discretely fractured system.

A finite-difference numerical model was developed and used to simulate simultaneous flow of water and NAPL in a discrete, rough-walled fracture. Equilibrium dissolution, full advective-dispersive transport in the fracture, and diffusion from the fracture into the matrix blocks were also simulated as water and NAPL flowed. In order to define system behaviour, several types of outputs were examined:

- total travel time for the NAPL to reach the base of the fracture,

- influence on NAPL distributions in the fracture,

- distribution of the dissolved phase in the fracture and the diffused phase in the matrix,

- mass flux from the fracture to the matrix, and

- total mass diffused into the matrix.

The analyses show that the total NAPL travel time and NAPL distribution were the most sensitive to changes in NAPL density, ln-aperture mean, ln-aperture variance, and the initial water flow field gradient. These parameters all directly affect the pressure field definition in slightly different ways. Increasing (or decreasing) NAPL density increases (or decreases) the capillary pressure at the aperture entry point. Larger densities therefore allow smaller apertures to be invaded, facilitating the movement of NAPL in the fracture.

Changes in the ln-aperture mean affect the pressure requirements for entry into an aperture segment. For a given capillary pressure, an aperture field with a higher average ln-mean aperture allows NAPL to flow more easily and uniformly, as the entry pressure will be exceeded in more aperture segments than in the case with smaller apertures. This parameter shows a particularly high degree of sensitivity to simulation results as the local fracture permeability is proportional to the square of the aperture. A smaller ln-aperture variance tends to homogenize the aperture field somewhat such that there are fewer very small or very large apertures. The result is a more uniform entry pressure field, where more apertures can be invaded but overall with lower saturations.

The initial water flow gradient also affects the pressure distribution at the capillary interface. Large water pressures (for given NAPL pressures) decrease the capillary pressure and hence lower the driving force behind NAPL flow; the converse is also true. The result is an attenuated NAPL flow field that flows much slower and is more spread out.

The distribution of the dissolved phase in the fracture and matrix and the total mass diffused in the matrix are strongly influenced by the NAPL solubility, matrix porosity, and effective diffusion coefficient chosen. Perturbations in choices of diffusion coefficient show characteristically different behaviour from the solubility or matrix porosity. All three parameters influence the strength of the mass flux from the fracture to the matrix, but in different ways. Solubility and matrix porosity re-

late to the amount of dissolved mass present, while the diffusion coefficient directly defines the rate at which mass can move via diffusion.

This research project showed that, for any appreciable volume flow of NAPL, the coupling between free-phase NAPL flow and transport is quite weak at lower solubilities. It remains for further study how the coupling strength increases with larger solubilities.

Matrix diffusion can be an important storage mechanism for dissolved phase NAPL in a rough-walled fracture. Even for the relatively short time scales considered here, appreciable amounts of mass were still able to diffuse into the matrix, particularly when compared to the amount of mass in the fracture. Because the drinking water standards of most NAPLs are orders of magnitude smaller than their aqueous solubilities, this mass, spread out into the matrix, can conceivably act as a source for groundwater contamination for long periods of time.

Many studies have examined dissolution and/or matrix diffusion for a static NAPL case. The model written for this thesis research was intended to provide insight into the interaction between simultaneous flow of NAPL and water and aqueous phase transport with matrix diffusion. Only two other studies were found to simulate all of the processes discussed. The study by Ross and Lu (1999) only simulated a one-dimensional fracture with a single aperture value in two-dimensional porous media, and the porous matrix was not impervious to advective water flow. Esposito and Thomson (1999) did not couple the flow and transport solution at every time step. Clearly, this is a relatively new area of research that requires further study.

Suggestions for continued research in this area would be to directly test the hypotheses put forth by Parker *et al.* (1994; 1997) and Ross and Lu (1999). That is, further knowledge could be gained by adapting the numerical model to test conditions of diffusive disappearance for slowly moving or immobile NAPL in a fracture or fracture network at longer time scales. More work could also be done in examining the micro-scale NAPL behaviour above extremely small apertures in at least

two dimensions, in order to test Ross and Lu's hypothesis that immobile NAPL can remobilize after large periods of time due to a decrease in diffusion gradient into the matrix.

References

Abdel-Salam, A., and C. V. Chrysikopoulos. 1996. Unsaturated flow in a quasi-three-dimensional fractured medium with spatially variable aperture. *Water Resources Research*, **32**(6), pp. 1531–1540.

Abdul, A. S. 1988. Migration of petroleum products through sandy hydrogeologic systems. *Ground Water Monitoring Review*, Fall, pp. 73–81.

Anderson, M. P., and W. W. Woessner. 1992. *Applied Groundwater Modeling: Simulation of Flow and Advective Transport*. San Diego: Academic Press, Inc.

Banack, L. 1996. Numerical Simulation of Non-Aqueous Phase Liquid Dissolution in Discrete Rough-Walled Fractures. M.Sc. Thesis, Department of Geology, University of Alberta.

Baveye, P., and G. Sposito. 1984. The operational significance of the continuum hypothesis in the theory of water movement through soils and aquifers. *Water Resources Research*, **20**(5), pp.521–530.

Bear, J. B. 1972. *Dynamics of Fluids in Porous Media*. New York: Dover Publications, Inc.

Behie, A., and P. K. W. Winsome. 1982. Block iterative methods for fully implicit reservoir simulation. *Society of Petroleum Engineers Journal*, **22**(October), pp. 658–668.

Brooks, R. H., and A. T. Corey. 1964. *Hydraulic Properties of Porous Media*. Fort Collins, Colorado: Colorado State University. Hydrology Paper No. 3.

Brown, S. R. 1987. Fluid flow through rock joints: The effect of surface roughness. *Journal of Geophysical Research*, **92**(B2), pp. 1337–1347.

Brown, S. R. 1995. Simple mathematical model of a rough fracture. *Journal of Geophysical Research*, **100**(B4), pp. 5941–5952.

Buckley, S. E., and M. C. Leverett. 1942. Mechanism of fluid displacement in sands. *AIME*, **146**, pp. 107–116.

Celia, M. A., E. T. Bouloutas, and R. L. Zarba. 1990. A general mass-conservative numerical solution for the unsaturated flow equation. *Water Resources Research*, **26**(7), pp.1483–1496.

Celia, M. A., and P. Binning. 1992. A mass conservative numerical solution for two-phase flow in porous media with application to unsaturated flow. *Water Resources Research*, **28**(10), pp. 2819–2828.

Cohen, R. M., and J. W. Mercer. 1993. *DNAPL Site Evaluation*. Boca Raton: C. K. Smoley.

Crank, J. 1956. *The Mathematics of Diffusion*. New York: Oxford University Press.

Esposito, S. J., and N. R. Thomson. 1999. Two-phase flow and transport in a single fracture-porous medium system. *Journal of Contaminant Hydrology*, **37**, pp.319–341.

Faust, C. R., and J. O. Rumbaugh. 1990. *SWANFLOW: Simultaneous Water, Air, and Nonaqueous Flow – Documentation*.

Faust, C. R. 1985. Transport of immiscible fluids within and below the unsaturated zone: A numerical model. *Water Resources Research*, **21**(4), pp.587–596.

Fetter, C. W. 1993. *Contaminant Hydrogeology*. New York: Macmillan Publishing Company.

Freeze, R. A., and J. A. Cherry. 1979. *Groundwater*. Toronto: Prentice-Hall.

Frind, E. O., J. W. Molson, and M. Schirmer. 1999. Dissolution and mass transfer of multiple organics under field conditions: The Borden emplaced source. *Water Resources Research*, **35**(3), pp.683–694.

Fung, L. S. K. 1991. Simulation of block-block processes in naturally fractured reservoirs. *Society of Petroleum Engineers, Reservoir Engineering Journal*, **31**(November), pp. 477–484.

Ge, S. 1997. A governing equation for fluid flow in rough fractures. *Water Resources Research*, **33**(1), pp. 53–61.

Guiguer, N., J. Molson, T. Franz, and E. Frind. 1994. *FLOTRANS: Two-Dimensional Steady-State Flownet and Advective-Dispersive Contaminant Transport Model - User Guide Version 2.2*. Waterloo Hydrogeologic.

Huyakorn, P. S., and G. F. Pinder. 1983. *Computational Methods in Subsurface Flow*. New York: Academic Press, Inc.

Huyakorn, P. S., S. Panaday, and Y. S. Wu. 1996. A three-dimensional multiphase flow model for assessing NAPL contamination in porous and fractured media, 1. Formulation. *Journal of Contaminant Hydrology*, **16**, pp. 109–130.

Imhoff, P. T., and C. T. Miller. 1996. Dissolution fingering during the solubilization of nonaqueous phase liquids in saturated porous media: 1. Model predictions. *Water Resources Research*, **32**(7), pp. 1919–1928.

Kueper, B. H. 1989. *The Behaviour of Dense, Non-Aqueous Phase Liquid Contaminants in Heterogeneous Porous Media*. Ph.D. Thesis, Department of Earth Sciences, University of Waterloo.

Kueper, B. H., and D. B. McWhorter. 1991. The behavior of dense, nonaqueous phase liquids in fractured clay and rock. *Ground Water*, **29**(5), pp. 716–728.

Kueper, B. H., and D. B. McWhorter. 1996. Physics Governing the Migration of Dense Non-Aqueous Phase Liquids (DNAPLs) in Fractured Media. *Pages 337–353 of:* Pankow, J. F., and Cherry, J. A. (eds), *Dense Chlorinated Solvents and other DNAPLs in Groundwater.* Portland, Oregon: Waterloo Press.

Leverett, M. C. 1941. Capillary behaviour in porous solids. *Trans. Soc. Pet. Eng. AIME,* **142**, pp. 152–169.

Mackay, D. M., and J. A. Cherry. 1989. Groundwater contamination: Pump-and-treat remediation. *Environmental Science and Technology,* **23**, pp. 630–636.

Mayer, A. S., and C. T. Miller. 1996. The influence of mass transfer characteristics and porous media heterogeneity on nonaqueous phase dissolution. *Water Resources Research,* **32**(6), pp. 1551–1567.

McWhorter, D. B., and B. H. Kueper. 1996. Mechanics and Mathematics of the Movement of Dense Non-Aqueous Phase Liquids (DNAPLs) in Porous Media. *Pages 89–128 of:* Pankow, J. F., and Cherry, J. A. (eds), *Dense Chlorinated Solvents and other DNAPLs in Groundwater.* Portland, Oregon: Waterloo Press.

Medina, A., and J. Carrera. 1996. Coupled estimation of flow and solute transport parameters. *Water Resources Research,* **32**(10), pp. 3063–3076.

Mendoza, C. A. 1992. Capillary Pressure and Relative Transmissivity Relationships Describing Two-Phase Flow Through Rough-Walled Fractures in Geologic Materials. Ph.D. Thesis, University of Waterloo, Waterloo, Ontario, Canada.

Mendoza, C. A., and E. A. Sudicky. 1992. Hierarchical scaling of constituitive relationships controlling multi-phase flow in fractured geologic media. *Reservoir Characterization III,* L. Linville, editor, PennWell Publishing, Tulsa, pp. 505–514.

Mercer, J. W. and C. R. Faust. 1976. The application of finite-element techniques to immiscible flow in porous media. Gray, W. G., G. F. Pinder, and C. A. Brebbia (eds). *Finite Elements in Water Resources.* Pentech Press, England.

Mercer, J. W. and R. M. Cohen. 1990. A review of immiscible fluids in the subsurface: Properties, models, characterization and remediation. *Journal of Contaminant Hydrology,* **6**, pp.107–163.

Moreno, L., Y. W. Tsang, C. F. Tsang, F. V. Hale, and I. Neretnicks. 1988. Flow and tracer transport in a single fracture: A stochastic model and its relation to some field observations. *Water Resources Research,* 24(12), pp. 2033–2048.

Mualem, Y. 1976. A new model for predicting the hydraulic conductivity of unsaturated porous media. *Water Resources Research,* 12(3), pp. 513–522.

Ogata, A. and R. B. Banks. 1961. *A Solution of the Differential Equation of Longitudinal Dispersion in Porous Media. U.S. Geological Survey Professional Paper,* **411-A.**

Parker, J. C. 1989. Multiphase flow and transport in porous media. *Reviews of Geophysics,* 27(3), pp. 311–328.

Parker, B. L., D. B. McWhorter, and J. A. Cherry. 1997. Diffusive loss of non-aqueous phase organic solvents from idealized fracture networks in geologic media. *Ground Water,* 35(6), pp. 1077–1088.

Parker, B. L., J. A. Cherry, and R. W. Gillham. 1996. The Effects of Molecular Diffusion on DNAPL Behavior in Fractured Porous Media. *Pages 355–393 of:* Pankow, J. F., and Cherry, J. A. (eds), *Dense Chlorinated Solvents and other DNAPLs in Groundwater.* Portland, Oregon: Waterloo Press.

Parker, B. L., R. W. Gillham, and J. A. Cherry. 1994. Diffusive disappearance of immiscible-phase organic liquids in fractured geologic media. *Ground Water,* **32**(5), pp. 805–820.

Peaceman, D. W. 1977. *Fundamentals of Numerical Reservoir Simulation.* The Netherlands: Elsevier Scientific Publishing Company.

Peng, G. P., J. L. Yanosik, and R. E. Stephenson. 1990. A generalized compositional model for naturally fractured reservoirs. *Society of Petroleum Engineers, Reservoir Engineering Journal,* **30**(May), pp. 221–226.

Powers, S. E., C. O. Loureiro, L. M. Abriola, and W. J. Weber, Jr. 1991. Theoretical study of the significance of nonequilibrium dissolution of nonaqueous phase liquids in subsurface systems. *Water Resources Research,* **27**(4), pp. 463–477.

Powers, S. E., L. M. Abriola, and W. J. Weber, Jr. 1992. An experimental investigation of nonaqueous phase liquid dissolution in saturated subsurface systems: Steady state mass transfer rates. *Water Resources Research,* **28**(10), pp. 2691–2705.

Protter, M. H., and C. B. Morrey. 1991. *A First Course In Real Analysis.* New York: Springer-Verlag New York, Inc.

Pruess, K. and Y. W. Tsang. 1990. On two-phase relative permeability and capillary pressure of rough-walled rock fractures. *Water Resources Research,* **26**(9), pp. 1915–1926.

Reeves, P. C., and M. A. Celia. 1996. A functional relationship between capillary pressure, saturation, and interfacial area as revealed by a pore-scale network model. *Water Resources Research,* **32**(8), pp. 2345–2358.

Reitsma, S. and B. H. Kueper. 1994. Laboratory measurement of capillary pressure-saturation relationships in a rock fracture. *Water Resources Research,* **30**(4), pp. 865–878.

Robin, M. J. L., A. L. Gutjahr, E. A. Sudicky, and J. L. Wilson. 1993. Cross-correlated random field generation with the direct Fourier transform method. *Water Resources Research,* **29**(7), pp. 2385–2397.

Rose, W. 1993. Coupling coefficients for two-phase flow in pore spaces of simple geometry. *Transport in Porous Media*, **10**, pp. 293–296.

Ross, B, and N. Lu. 1999. Dynamics of DNAPL Penetration into Fractured Porous Media. *Ground Water*, **37**(1), pp. 140–147.

Rossen, R. H., and E. I. C. Shen. 1989. Simulation of gas/oil drainage and water/oil imbibition in naturally fractured reservoirs. *Society of Petroleum Engineers, Reservoir Engineering Journal*, **29**(November), pp. 464–470.

Rostron, B. J. 1990. Numerical Simulation of Oil Migration Through a Lenticular Reservoir. M.Sc. Thesis, Department of Geology, University of Alberta.

Slough, K. J., E. A. Sudicky, and P. A. Forsyth. 1999. Importance of rock matrix entry pressure on DNAPL migration in fractured geologic materials. *Ground Water*, **37**(2), pp. 237–244.

Sudicky, E. A. 1988. *Craflush - Parallel Crack Model.*

Sudicky, E. A., and E. O. Frind. 1982. Contaminant transport in fractured porous media. *Water Resources Research*, **18**(6), pp. 1634–1642.

Sudicky, E. A., and R. G. McLaren. 1992. The Laplace transform Galerkin technique for large-scale simulation of mass transport in discretely fractured porous formations. *Water Resources Research*, **28**(2), pp. 499–514.

Schwille, F. 1988. *Dense Chlorinated Solvents in Porous and Fractured Media - Translated by James F. Pankow.* Chelsea, Michigan: Lewis Publishers.

Tsang, Y. W., and C. F. Tsang. 1989. Flow channeling in a single fracture as a two-dimensional strongly heterogeneous permeable medium. *Water Resources Research*, **25**(9), pp. 2076–2080.

van Genuchten, M. T. 1980. A closed-form equation for predicting the hydraulic conductivity of unsaturated soils. *Soil Science of America Journal*, 44(5), pp. 892–898.

Wang, H. F., and M. P. Anderson. 1982. *Introduction to Groundwater Modeling: Finite Difference and Finite Element Methods*. New York: W.H. Freeman and Company.

Wang, J. S. Y. 1991. Flow and transport in fractured rocks. *Reviews of Geophysics, Supplement*. pp. 254–262.

Weber, W. J., Jr., P. M. McGinley, and L. M. Katz. 1991. Sorption phenomena in subsurface systems: Concepts, models, and effects on contaminant fate and transport. *Water Research*, 25(5), pp. 499–528.

Witherspoon, P. A., J. S. Y. Wang, K. Iwai, and J. E. Gale. 1980. Validity of the cubic law for fluid flow in a deformable rock fracture. *Water Resources Research*, 16, pp. 1016–1024.

Zheng, C. 1990. *MT3D: A Modular Three-Dimensional Transport Model for Simulation of Advection, Dispersion, and Chemical Reaction of Contaminants in Groundwater Systems - User Guide Version 1.5*. S.S. Papadopulos and Associates, Inc.